

Cite this: *J. Mater. Chem. A*, 2023, 11, 10015

# CdS based 3D nano/micro-architectures: formation mechanism, tailoring of visible light activities and emerging applications in photocatalytic H<sub>2</sub> production, CO<sub>2</sub> reduction and organic pollutant degradation

Jai Prakash,<sup>a</sup> Pragati Kumar,<sup>b</sup> Nupur Saxena,<sup>c</sup> Zonghua Pu,<sup>d</sup> Zhangsen Chen,<sup>d</sup> Ankit Tyagi,<sup>e</sup> Gaixia Zhang<sup>f</sup> and Shuhui Sun<sup>g</sup>

Semiconductor photocatalyst nanomaterials have been extensively studied for the last few decades due to their great potential in solving energy and environmental problems on the earth by harnessing solar light. Cadmium sulfide (CdS) based nanomaterials have emerged as promising photocatalyst materials due to their visible light absorption and physio-chemical properties suitable for high-performance photocatalytic activities in terms of solar-fuel generation and environmental/water remediation. CdS photocatalysts have been reported in several morphologies from 0-dimensional to 3-dimensional (0-3D) nano/micro-architectures. However, regarding CdS photocatalysts with specific nanostructures, 3D nanostructures (nanoflowers, self-assembled -hierarchical, hollow, tetrapod, etc.) have shown special structural features with high surface/volume ratio and significant improvement in their photocatalytic properties for various energy and environment applications. This review deals with CdS-based 3D nano/micro-architectures (sole CdS and nanocomposites with various functional nanomaterials), their formation mechanism and tailoring of properties for visible light induced photocatalytic activities in energy and environmental applications. Particularly, it includes the emerging applications of 3D CdS-based photocatalysts in photocatalytic H<sub>2</sub> production, photocatalytic CO<sub>2</sub> reduction and photodegradation of organic pollutants with an emphasis on the mechanism as well as the role of functional nanomaterials in boosting photocatalytic activities of CdS. Moreover, various challenges and future prospects in the research of CdS-based photocatalysts have also been discussed.

Received 21st January 2023  
Accepted 18th April 2023

DOI: 10.1039/d3ta00396e

rsc.li/materials-a

## 1. Introduction

In recent years, due to their fascinating properties and remarkable applications in various fields, semiconductors have gained more attention and are in the limelight due to their potential as futuristic nanomaterials for technological applications. Cadmium sulfide (CdS), being an n-type semiconductor, having a band gap (bulk) of ~2.4 eV at room temperature, is

applicable in visible light induced activities in the field of energy and environment.<sup>1-6</sup> It possesses high stability and also shows a quantum size effect.<sup>3,7-9</sup> It normally exists in wurtzite lattice possessing hcp geometry which is the most stable state, whereas, its cubic lattice possesses ccp geometry which is known to be the least stable. Its rock salt lattice possesses ccp geometry at high pressure.<sup>10-13</sup> CdS-based nanomaterials exhibit various novel optical, electronic, magnetic, chemical and structural properties.<sup>11,14-16</sup> As the band gap of CdS lies in the visible region of the electromagnetic spectrum, it shows efficient sunlight photo-activities. However, it possesses a few drawbacks like a high recombination rate of photogenerated charge carriers (electrons and holes) and less photochemical stability as photocorrosion of CdS is a major problem.<sup>17-22</sup> These issues seriously lower its photocatalytic efficiencies and are bottlenecks in its potential applications in the field of energy and environment.<sup>18,21</sup> It is well-known that the properties and the corresponding applications of the CdS nanomaterials significantly depend on the size and architecture.<sup>23-25</sup>

<sup>a</sup>Department of Chemistry, National Institute of Technology Hamirpur, Hamirpur-177005, India. E-mail: jaip@nith.ac.in

<sup>b</sup>Nano-Materials and Device Lab, Department of Nano Sciences & Materials, Central University of Jammu, Rahya-Suchani, Samba, Jammu, 181143, India

<sup>c</sup>Department of Physics, Indian Institute of Technology Jammu, 181221, India

<sup>d</sup>Institut National de la Recherche Scientifique (INRS), Centre Énergie Matériaux Télécommunications, Varennes, Québec, J3X 1P7, Canada. E-mail: shuhui.sun@inrs.ca

<sup>e</sup>Department of Chemical Engineering, Indian Institute of Technology Jammu, 181221, India

<sup>f</sup>Department of Electrical Engineering, École de Technologie Supérieure (ÉTS), Montreal, QC H3C 1K3, Canada

It has been reported that its properties can be improved in order to enhance its photocatalytic properties by engineering its shape/size and forming hybrid nanocomposite structures with other functional nanomaterials.<sup>26–31</sup> Various functional nanomaterials such as noble metals/plasmonics,<sup>32–36</sup> semiconductors,<sup>37–41</sup> carbon-based materials (graphene, graphene oxides, carbon nanotubes, *etc.*)<sup>20,42–45</sup> have great potential to improve the photocatalytic activity of CdS and other semiconductors. For example, Li *et al.*<sup>31</sup> proposed a CdS/graphene nanocomposite to overcome these problems by first increasing the number of adsorption sites for sacrificial reagents, resulting in more consumption of holes instead of oxidizing CdS itself. Secondly, reduces the bulk recombination of photogenerated  $e^-$  and  $h^+$  pairs resulting in a greater improvement in the photoactivity of CdS/graphene nanocomposite. Various synthesis techniques such as chemical, physical and green synthesis methods have been found to be useful for tailoring the properties of nanostructured materials<sup>46–54</sup> and have been used to modify CdS-based nanomaterials in order to enhance their photocatalytic activities.<sup>55–60</sup>

In the case of nanomaterials, it has been found that the size and shape of nanostructures show great influence on their physical/chemical properties and further on their functionality.<sup>62</sup> CdS nanomaterials have been reported in different structures, *i.e.* 0 to 3 dimensions (0-3D) with some different properties/functionality originating from their geometries<sup>8,9,63–68</sup> as shown in Fig. 1a. These different forms of CdS nanostructures have extensively been studied and applied in various fields of energy and environment particularly because of their excellent solar-driven photo activities. All the forms of CdS have unique properties because of their morphologies that contribute to their functionality.<sup>7,40,50,69</sup> Especially, 3D nanostructures provide a high surface-to-volume ratio, which promotes better surface activities for functional applications.<sup>40,69</sup> For example, 3D CdS nanostructures have been shown to have great potential in photocatalytic applications in the field of energy and environment. Hence, morphology is an important parameter that influences photocatalytic activity. However, the fabrication of such nanostructures or hybrid nanostructures with complex morphology is very difficult as they require high preparation skills.<sup>64,70</sup> There have been several studies reporting on the reduced band gap up to 2.25 eV and improved photocatalytic activities by tailoring the shapes/morphologies of the 3D CdS nanostructures using the hydrothermal method.<sup>63,65,71</sup> Recently, Shenoy *et al.*<sup>69</sup> studied the comparative photocatalytic functionalities of different morphologies *i.e.* 1D, 2D and 3D of CdS nanostructures in view of their energy and environmental applications. They studied the photodegradation of erioglaucline and photocatalytic hydrogen evolution using those 1-3D CdS nanostructures under visible light. It was found that out of all these nanostructures, 3D CdS morphology showed better photocatalytic activities as compared to other morphologies along with good photo corrosion stability. Even enhanced photo functional applications have been reported by hybrid CdS 3D nanostructures.<sup>72</sup> For example, Wang *et al.*<sup>70</sup> fabricated hierarchical flower-like Au@CdS-CdS nanoparticles composed of a core of Au, a shell of CdS, and CdS nanorod structures. These

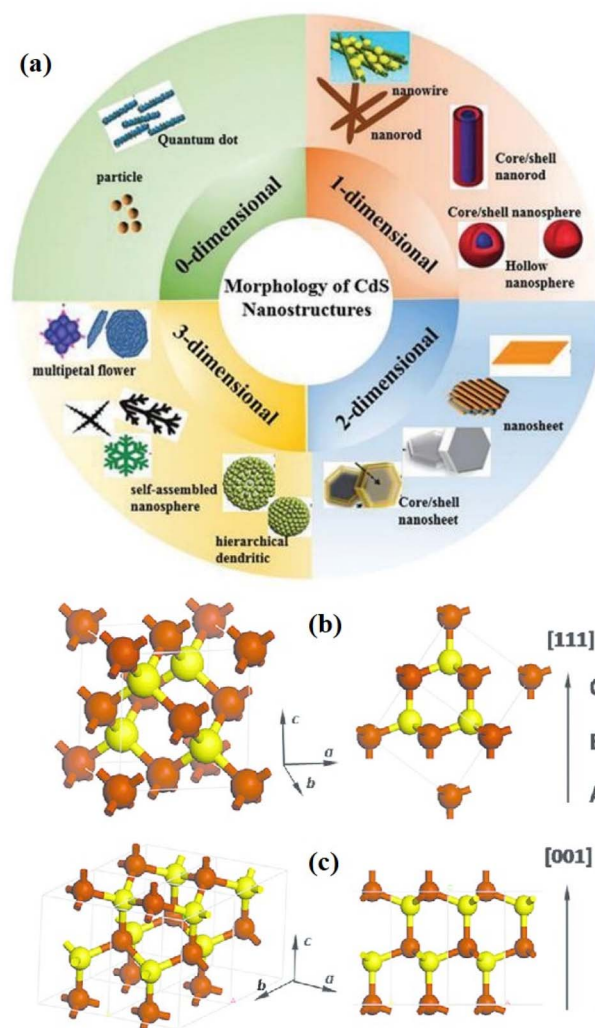


Fig. 1 Schematic diagram of (a) various dimensions of CdS nanostructures and the unit cell of the CdS crystal structure with (b and c) wurtzite (hcp), and zinc blend (ccp) phases. Reprinted with permission from ref. 61.

multi-structured CdS-based nanoflowers exhibited absorption within the whole range of UV-visible region up to 850 nm and the highest photocatalytic degradation as well as photocatalytic hydrogen production under visible light as compared to the sole CdS or Au@CdS 3D nanostructures.

In this way, extensive research has been conducted in the past decades for the degradation of harmful/toxic organic pollutants and the generation of hydrogen *via* photocatalytic water splitting. This could be possible through the rational design, development and tailoring of efficient semiconductor nanomaterials for the next generation of high-performance photocatalysts. These provide a promising way to produce clean energy and to solve the various environmental issues related to air/water pollution as well as global warming.<sup>69,73</sup> This review deals with the rational design and development of CdS-based 3D nano-architectures through tailoring and nanocomposites formation with various functional nanomaterials for visible light-induced photocatalytic activities in degradation

of emerging organic pollutants with an emphasis on the mechanism and role of functional nanomaterials in boosting its photocatalytic activities. Moreover, emerging applications of 3D CdS-based photocatalysts in photocatalytic H<sub>2</sub> production and photocatalytic CO<sub>2</sub> reduction have also been reported followed by challenges and future prospects in research of CdS-based photocatalysts in brief.

## 2. Basics of CdS and morphologies

### 2.1. Basic properties of CdS

CdS is a compound semiconductor of the II–VI group that exhibits three crystalline structures namely cubic (zinc blende), hexagonal (wurtzite), and rock salt. The hexagonal phase possesses a *P6<sub>3</sub>mc* space group with *a* = 4.160 Å and *c* = 6.756 Å nm and is the most stable crystalline phase (in both bulk and nano-crystalline form). While the cubic phase is a metastable crystalline phase that exhibits in nanomaterials only and holds an *F43m* space group with an average lattice parameter of 5.832 Å. In both the crystalline structures, Cd and S atoms are tetrahedrally coordinated. However, the stacking sequence of the atoms is ABABAB *etc.* in the wurtzite form that consists of hexagonal close packing (hcp), while the zinc blende structure has the stacking sequence of the atoms as ABCABC..., *i.e.*, called cubic close packing (ccp)<sup>74</sup> (Fig. 1b and c). Instead, the rock salt is a high-pressure crystalline phase in a nano regime having a *Pmnn* space group with lattice parameters *a* = *b* = 3.898 Å and *c* = 5.511 Å. The rock salt crystalline structure is built up by the alternative coordination of each atom (say Cd) to six other atoms (say S) in an octahedral fashion such that every atom has six neighboring atoms of the opposite kind. Identical to the zinc blende phase, the rock salt phase possesses ccp with stacking sequence ABCABC *etc.* indeed, many properties of the material particularly optical and electronic depend on the different crystal structures due to differences in their lattice parameters. The formation of a particular phase and thereby its property depends on many factors including synthesis methods and conditions, choice of precursors, post-synthesis treatments, *etc.*<sup>75–79</sup> Besides, the structural and other properties may also be tuned by the incorporation of suitable impurity elements.<sup>74,80</sup>

The bulk bandgap (~2.4 eV at room temperature) of CdS is well lying in the visible region of the electromagnetic spectrum and allows marvelous applications in vast areas including solar cells, LEDs, lasers, photodetectors, photocatalysis, temperature sensors, biosensors, gas sensor, environmental monitoring, and chemical sensors, *etc.*<sup>61,81–88</sup> In the band structure of CdS, S 3p orbitals contribute to the top of the valence band (VB), while Cd 5s and 5p orbitals contribute to the bottom of the conduction band (CB). The lower position of CB is dominated by Cd 3d orbitals. In particular, photocatalytic technology required the excitation of the photogenerated charge carriers by absorbing light photons, bulk diffusion and surface reaction of photo-generated electrons.<sup>61</sup> Thus, the position of CB and VB with respect to redox potential is very important to utilize the extended part of solar radiation for the splitting of a large amount of H<sub>2</sub>, *i.e.*, efficient photocatalysis. Among various semiconductors, VB and CB levels of CdS are closest to the O<sub>2</sub>/

H<sub>2</sub>O redox couple (1.23 V vs. normal hydrogen electrode (NHE), pH = 0) and H<sup>+</sup>/H<sub>2</sub> redox couple (0 V vs. NHE, pH = 0).<sup>89</sup> In addition, CdS can mobile photogenerated electrons and holes efficiently and timely due to its good carrier transportation ability that increases the carriers' life and leads to high photocatalytic activity.<sup>61</sup> Moreover, heat treatment can assist the formation of functional interfaces between CdS and other co-catalysts easily. These functional interfaces are the major decisive asset for photocatalytic property and its application in water splitting.<sup>89</sup>

### 2.2. 3D CdS nano/micro-architectures: morphology and formation mechanism

Surface morphology *i.e.* shape of nanostructures, grain size, surface roughness, and surface energy, *etc.* alters multiple properties of the materials, and thereby the functioning of materials in a particular application changes.<sup>90</sup> It has been found that mostly, 3D CdS nanostructures are formulated *via* a self-assembly process.<sup>61,91</sup> Therefore, it is essential to understand the morphology-dependent mechanism for desired application/property and hence the control over surface processes and composition is decisive for repeatability and reliability.

**2.2.1. Nano/micro flower structures.** Nano/micro flower structures are 3D structures that look like natural plant flowers with sizes ranging from nanoscale to micron size.<sup>40</sup> CdS-based 3D nano/micro structures have been extensively studied in the past years because of their simple preparation strategies, control over the morphology, surface area, and improved optoelectronic properties relevant to photocatalytic applications.<sup>23,69,92</sup> For example, Liu *et al.*<sup>92</sup> demonstrated a simple mixed solvothermal method to control the morphology of CdS 3D nanoflowers and studied the morphology-dependent photocatalytic hydrogen evolution. It was observed that the variation in solvent and their concentration resulted in different morphologies such as NFs, porous NFs, nanobelts (NBs), and net-like structures as illustrated in Fig. 2(a<sub>1</sub>–a<sub>4</sub>) and (b<sub>1</sub>–b<sub>4</sub>) respectively along with the schematic of their formation mechanism in between. They predicted that N atoms in an organic solvent like diethylenetriamine (DETA) played a vital role in controlling the morphology as they can be bonded to the exposed Cd atoms in the (1 0 0) and (0 1 0) surfaces, inhibiting the crystal growth along these directions and promoted along [0 0 2] direction only. They observed that alone DETA as a solvent allowed it to grow into bulk-like structures attributed to the high viscosity of DETA resulting in strong bonding between Cd and N atoms. On the other hand, the addition of an assist solvent of good fluidity like H<sub>2</sub>O weakened the N–Cd attraction due to the balance of N–Cd and N–H<sup>+</sup> and resulting in a wire-like structure whereas the gradual replacement of H<sub>2</sub>O by ethanol (EtOH) strengthened N–Cd and weakened N–H<sup>+</sup>, consequently belt and porous flower-like structures were grown.<sup>92</sup> While Yao *et al.*<sup>93</sup> controlled the morphology of CdS nanostructures by varying the volume ratio of DETA and deionized water in a facile solvothermal approach. The reaction was carried out at 180 °C for 12 h and obtained morphologies

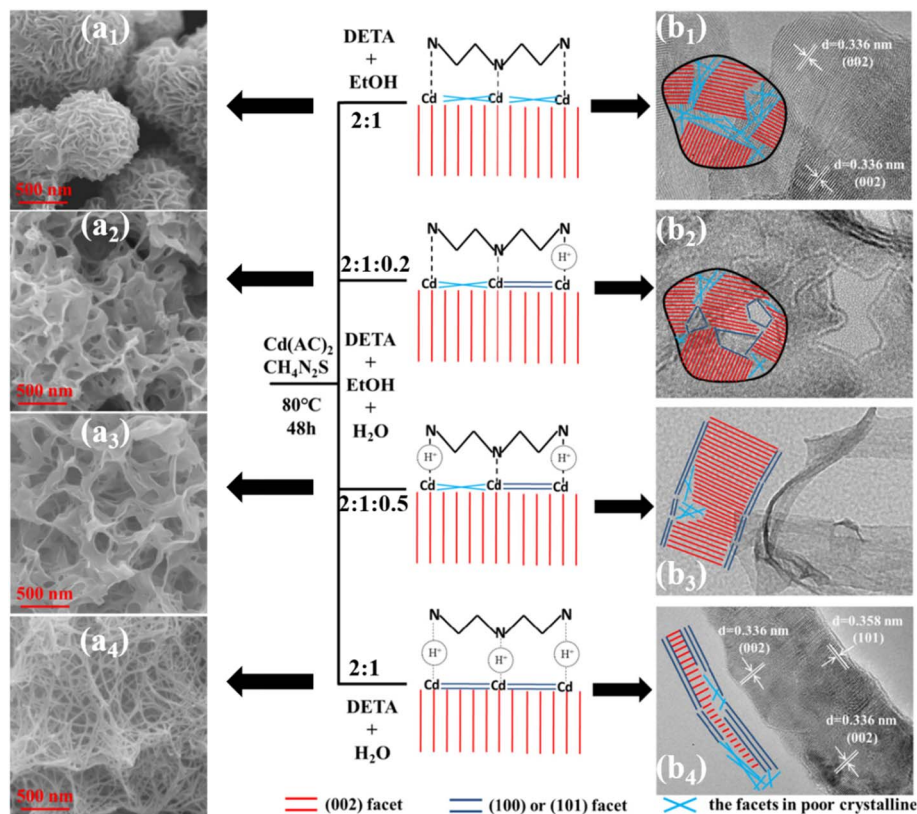


Fig. 2 Schematic diagram of formation mechanisms for flower-like, porous flower-like, belt-like and net-like CdS. Reprinted with permission from ref. 92.

are demonstrated in Fig. 3a. Further, they investigated the photocatalytic activity of these nanoflowers structures by choosing photocatalytic degradation of acid fuchsine ( $C_{20}H_{17}N_3O_9S_3-Na_2$ ) as a test reaction and observed the highest photocatalytic activity due to the branched nanowires with higher surface area among all morphologies.<sup>93</sup>

A detailed systematic investigation of the processing parameters like growth temperature and time, Cd/S molar ratio, the concentration of capping molecules like thiourea and hexamethylenetetramine (HMT) that influence the shape of 3D nanostructures (NSs) during hydrothermal synthesis was carried out by Chen *et al.*<sup>63</sup> The influence of said processing parameters on the shape of 3D NSs is illustrated in Fig. 3b which describes the mechanism for the formation of 3D CdS NSs.<sup>63</sup> The influence of the concentration of complexing agents like ethylenediamine (EDA) along with time and concentration of surfactant (sodium dodecyl benzene sulfonate: SDBS) on 3D CdS NSs was investigated by Yang *et al.*<sup>71</sup> They optimized the concentrations of EDA, SDBS, and time as 0.009 mol, 0.01 g  $ml^{-1}$  and 5 h respectively for the growth of quality CdS NFs cubic phase and found that the photocatalytic degradation of MB was shown better in the case of NFs morphology as compared to CdS NPs.

Doping of CdS nanostructures, reaction temperature and time are other important parameters that affect the morphology of the various nanostructures forming 3D CdS NFs.<sup>94,95</sup> For example, the morphology of hydrothermally synthesized CdS

NSs at 150 °C for 2 h was found to be changed from nano-flakes to fine NFs by varying the concentration of dopant (Mn).<sup>94</sup> It was found that the doping induced a decrease in crystalline size resulting in a high surface area, lower band gap and recombination rate of photogenerated charge carriers. All these contributed to the unprecedented photocatalytic activity for the decomposition of MB and methyl violet (MV) dyes. The effect of reaction time on the morphology and other properties including photocatalysis of hydrothermally grown PVP-capped CdS was investigated. It was observed that the morphology of PVP-capped CdS NSs changes from the spherical-like nano-grains to NFs (3 h) to sword-like branched NFs with varying reaction temperatures from 1 h to 5 h at 200 °C. The sword-like branched NFs growth starts beyond the reaction time of 3 h due to the initiation of secondary nucleation.<sup>95</sup> Thin films of CdS NFs were also deposited using chemical bath deposition (CBD) at the reaction temperature of 80 °C for 1 h<sup>96</sup> and at 60 °C for 3–12 h followed by annealing at 300 °C for 2 h.<sup>96</sup> Further, these CdS NFs thin films were applied as photoanode for water splitting and high as well as stable current density with enhanced efficiencies were achieved.<sup>96</sup> Besides, the physical vapor deposition (PVD) method was also used to grow CdS microstructures (rose-flower) at an elevated temperature of 800 °C for 1 h.<sup>97</sup>

A facile colloidal chemical method with the aid of cetyltrimethyl ammonium bromide (CTAB) has also been used to fabricate uniform 3D porous CdS NFs. In this study, the effect of

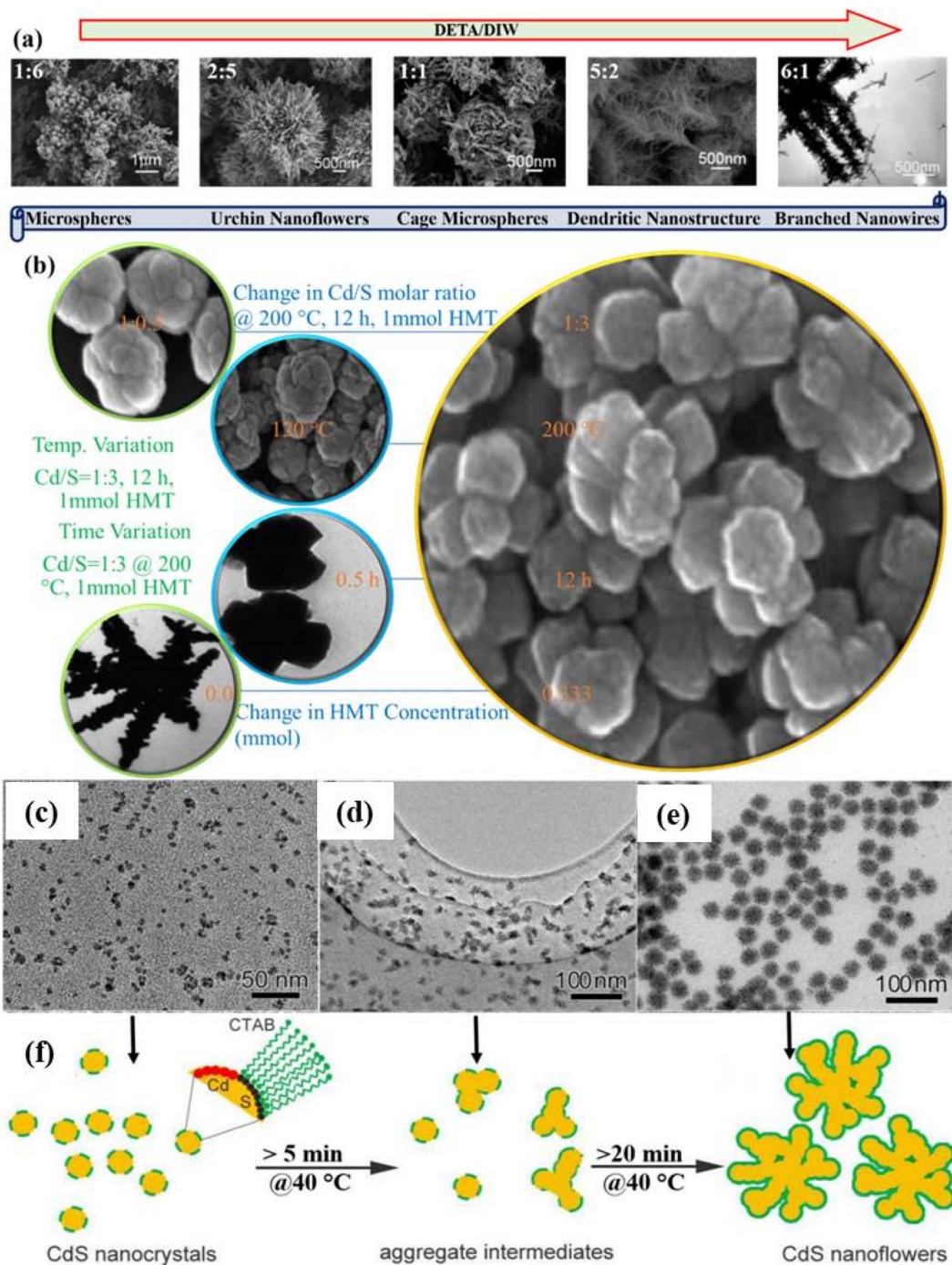


Fig. 3 Change in the morphology of CdS as a function of (a) DETA/DIW ratio. Reprinted with permission from ref. 93 and (b) various reaction parameters. Reprinted with permission from ref. 63. TEM images of CdS NFs with different reaction times: (c) 5 min, (d) 10 min, (e) 30 min at a reaction temperature of 40 °C and (f) growth process. Reprinted with permission from ref. 23.

reaction time keeping other parameters fixed was examined to insight into the understanding of the mechanism for the evolution process of the CdS NFs. The overall reaction was carried out at a low reaction temperature of 40 °C and the morphology evolution process was analyzed *via* TEM images as shown in Fig. 3c–e. It was concluded that nanocrystals were assembled leading to the formation of NFs in intermediate states as schematically shown in Fig. 3f. However, at elevated

reaction temperature (90 °C), the reaction rate was so fast and NFs were formed within 10 s.<sup>23</sup>

**2.2.2. Nano/micro hollow and spherical structures.** Nano/micro hollow and spherical structures are unique 3D structures with uniform and a large fraction of empty space as well as, intact shells inside providing a large surface area that could be beneficial for the adsorption of foreign molecules, especially in case of photocatalytic processes in energy and environmental

applications.<sup>98–100</sup> Additionally, hollow 3D structures possess low specific weight, and high mechanical strength and could be utilized as a nano/micro container for different purposes. These structures have shown great applications in the field of photocatalysis, lithium-ion batteries, hydrogen storage, *etc.* as well as in biomedicines and pharmaceuticals.<sup>100</sup>

In most of the studies, the 3D CdS hollow spherical structures are limited to mesoscale hollow/nano/micro spheres with diameters typically exceeding 100 nm.<sup>100</sup> For example, Wang *et al.*<sup>101</sup> synthesized 3D nanostructured CdS nanocrystals with mesospheres (MSPs) morphology on large scale. These hydrothermally synthesized 3D structures were composed of radially arranged nanorods from the center of CdS mesospheres and various reaction conditions were studied for morphological formulation and its mechanism. CdS MSPs were obtained at 200 °C for varying times, *i.e.* 12, 24, and 40 h, without using any surfactants and it was found that prolonging of reaction time induces larger crystal size. A surfactant and template free synthesis of CdS microspheres was reported using solvothermal process where 4,4'-dipyridyldisulfide (DPDS = (C<sub>5</sub>H<sub>4</sub>N)<sub>2</sub>S<sub>2</sub>) was used as a temperature controlled *in situ* source to provide S<sup>2-</sup> ions at 120–140 °C for 12 h.<sup>102</sup> It was observed that the increase in the size of microspheres was temperature dependent. CdS microspheres with spherical morphology sizes ranging from 0.5 to 2 μm were obtained. The morphological analysis exhibited that the microspheres were composed of assembled CdS NCs of ultrasmall (2–5 nm) size (Fig. 4a–c). The formation mechanism was explained on the basis of the breaking of the S–S bond of DPDS at ≥120 °C with the generation of S<sup>2-</sup> ions followed by a reaction with Cd<sup>2+</sup> ions to form CdS NCs. Subsequently, the self-aggregation of these NCs forms CdS microspheres (Fig. 4d).<sup>102</sup> These microspheres were found to be excellent visible light active photocatalysts against the degradation of MB molecules. Further, they studied the Zn-doped CdS microspheres with tunable band structures for efficient water splitting and reduction of the aromatic compound for water applications.<sup>103</sup> Similarly, mesoporous CdS microspheres of sizes more than 1 μm were fabricated by Patel *et al.*<sup>104</sup> with pronounced photocatalytic activity against the photodegradation of rhodamine B (RhB).

Han *et al.*<sup>106</sup> synthesized CdS nanospheres (NSPs) using the hydrothermal method by varying the molar concentration ratio of precursors at 200 °C for 5 h. They proposed that the C=S bond broken by the attack of the strong nucleophilic O atoms of H<sub>2</sub>O molecules releases S<sup>2-</sup> anions slowly that reacted with Cd<sup>2+</sup> ions and formed CdS NCs due to constrained growth of nuclei in the presence of an excess of thiourea. Further, the self-assembly of individual NCs occurred to form NSPs. Whereas, the shape of CdS NCs was tuned from NRs to NSPs by manipulating the addition rate of the sulfide precursor and was stabilized *via* tetraethyl ammonium bromide (TOAB) ligand in a non-aqueous medium. The observations revealed the growth mechanism follows the effective monomer concentration model, where the shape evolution was explained by manipulating the free energy of the crystallographic faces of the nuclei formed. CdS NSPs were also grown at room temperature using a simple and fast sonochemical method with different molar

ratios of Cd and S in starting solutions of surfactant EG and CTAB. They believed that the radical species obtained from the solvent EG and the acidity of the solution formed CdS. Further, the observed reduction in NSPs size with an increase in S content in the starting solution was explained by considering the fact that the increased concentration of S, speeded up the releasing of sulfite ions from the CTAB micelles and limited the particle growth and *vice versa*.<sup>107</sup> The surfactant-free CdS NSPs were synthesized by a single-step chemical method where the uniformity in shape was controlled *via* variation in thioacetamide concentration (C<sub>2</sub>H<sub>5</sub>NS-TAA). They observed that smooth NSPs formed if the mole concentration of TAA is equal to the mole concentration of Cd(NO<sub>3</sub>)<sub>2</sub> while transforming into uniform mesoporous NSPs occurred at slightly higher concentration of TAA due to liberation of the H<sub>2</sub>S gas bubbles during the decomposition of TAA that evolved the reactions as the soft template driven by the minimization of interfacial energy tends to aggregation of NPs. Further, an increase in the mole concentration of TAA tends to agglomerate the spheres with each other and regrowth the NSPs on the surfaces of pre-growth NSPs.<sup>108</sup>

On the other hand, biomolecule (soulcarboxymthyl chitosan) assisted CdS hollow spheres (HSPs) were synthesized solvothermal at 140 °C for 24 h as shown in Fig. 4e and f.<sup>105</sup> Here, the supersaturated solution under alkaline conditions formed CdS NPs nucleate that aggregated into round spheres owing the minimization of the interfacial energy with the assistance of soulcarboxymthyl chitosan. The formed [Cd(NH<sub>3</sub>)<sub>4</sub>]<sup>2+</sup> complex due to the presence of ammonia in the reaction reacted with S<sup>2-</sup> under the hydrothermal conditions to form CdS. Subsequently, the dissolution of CdS by NH<sub>3</sub> to form [Cd(NH<sub>3</sub>)<sub>4</sub>]<sup>2+</sup> and the reprecipitation of CdS from the solution simultaneously occur as illustrated by the reactions (Fig. 4g). As the reaction progresses the CdS NPs grew bigger at the surface with the continuous evacuation of the smaller core particles during the dissolution–reprecipitation process which resulted in inner cavities eventually and thus HSPs were formed.<sup>105</sup> Similarly, Wang *et al.*<sup>109</sup> demonstrated the formation of CdS hollow microspheres (HMSPs) of size about 5 μm with a diameter of the center hole of about 500 nm using oxalic acid as an auxiliary agent by solvothermal method. They investigated the effect of various parameters such as reaction time (12 h to 24 h), temperature (100–120 °C), and concentration of synthetic auxiliary agent and sodium precursor on growth of high quality CdS HMSPs. It was found that reaction time played an important role in growth of 3D CdS HMSPs (Fig. 5a–d) which exhibited a band gap of 2.31 eV and better absorption in visible light. It was also considered that the S source was the key parameter for the internal structure and mass transport control during the growth mechanism as shown in Fig. 5e. Under high reaction temperature, Cd<sup>2+</sup> and H<sub>2</sub>S formed CdS nanosheets quickly that nucleated rapidly into primary NCs, which grew and self-assembled through random aggregation into small unstable spheres due to a high degree of energy. Thus the excess energy released through the hole formation along the *c*-axis in each hexagonal CdS sphere and resulted in HMSPs.<sup>109</sup>

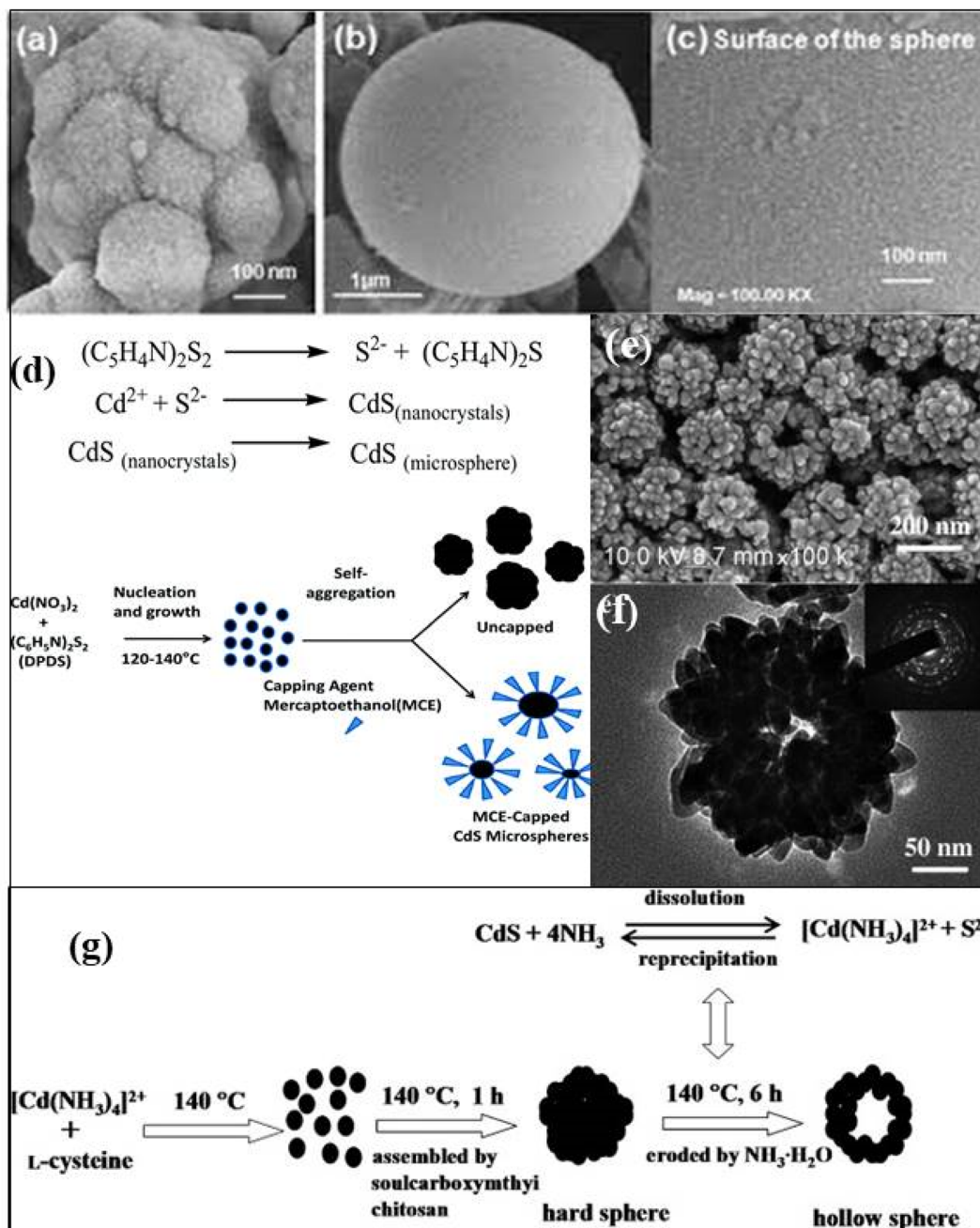


Fig. 4 FESEM images of a CdS microsphere, with (a) and without (b, c) capping agent, (c) shows the presence of nanocrystals (d) the formation mechanism of CdS microspheres. Reprinted with permission from ref. 102 (e) SEM and (f) TEM micrographs of hollow CdS microspheres structures with (g) the formation mechanism of CdS hollow microspheres. Reprinted with permission from ref. 105.

**2.2.3. Hierarchical nanostructures.** The 3D nano/micro hierarchical structures are usually referred to nanostructured morphologies with multidimensional domains at different levels or multimodal pore structures.<sup>110</sup> There are many typical hierarchical nanostructures *i.e.* urchin-like, brush-like, flower-like, tree-like, dendritic and branched structures. Generally, these 3D nano/micro hierarchical structures are composed of different nanosized building blocks and are created by mimicking the marvelous hierarchical and fractal structures such as trees and the surface structures of plant leaves existing

in nature.<sup>110,111</sup> For instance, Xiong *et al.*<sup>11,112</sup> demonstrated the preparation of such novel hierarchical nanostructures with tunable optical, morphological and photocatalytic properties. The preparation of CdS hierarchical nanostructures of various shapes such as water lily, nanorices, nanofans was carried out by nanorod bunch self-assembly (Fig. 6a–d) *via* control of reaction conditions *i.e.* volume ratio of the mixed solvents, reaction temperature, and reaction time following a facile L-cysteine and ethanolamine (EA)-synergistically assisted hydrothermal route. The growth mechanism was proposed based on

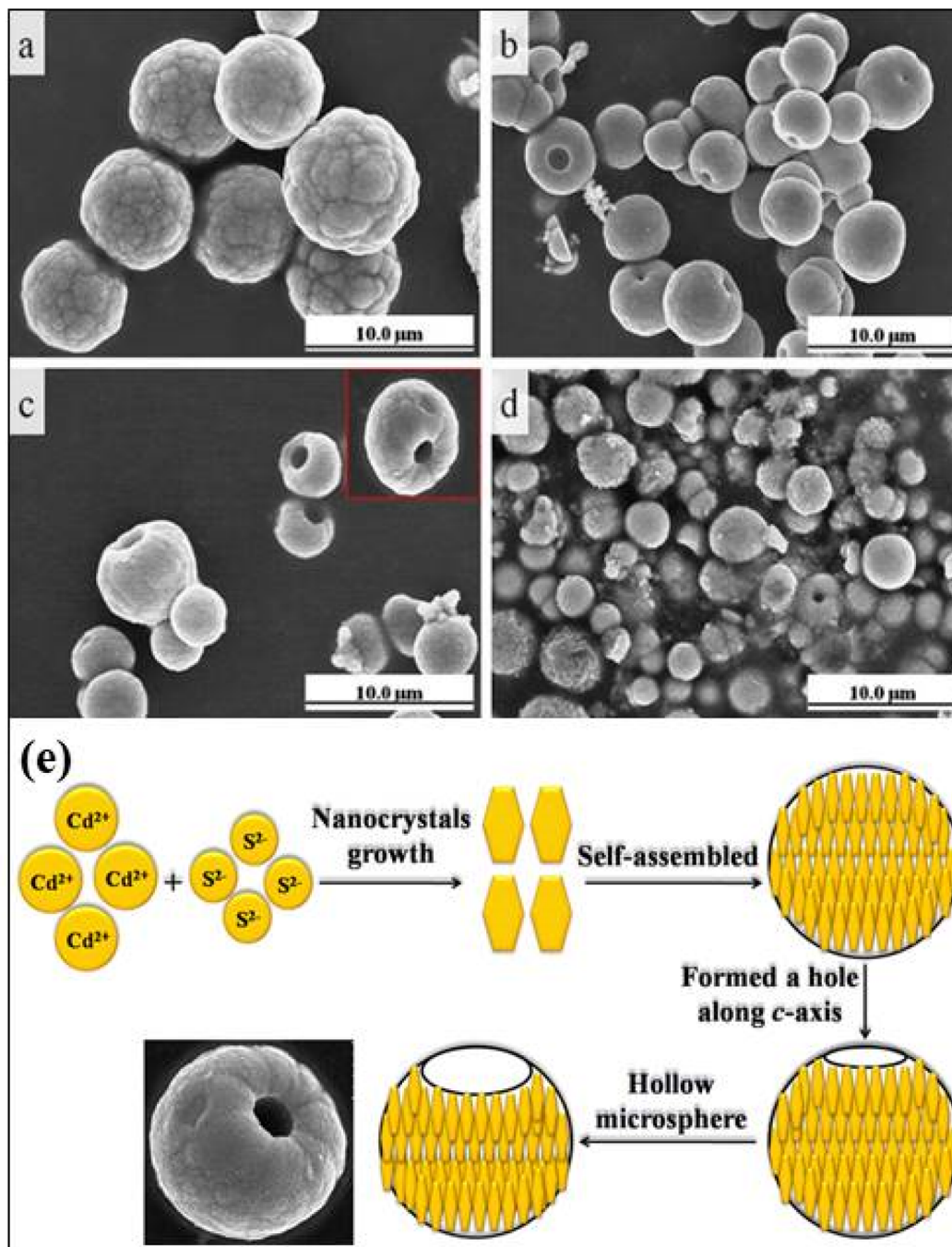


Fig. 5 The FESEM images of CdS at different reaction times. (a) 8 h, (b) 12 h, (c) 24 h, (d) 36 h. (e) Growth mechanism of hollow microsphere CdS structures. Reprinted with permission from ref. 109.

consecutive processes of *L*-cysteine and EA ratio synergistically assisted nucleation growth, oriented assembly, and sphere-cracking.<sup>112</sup>

Similarly, Pandit *et al.*<sup>113</sup> proposed another hydrothermally assisted method for synthesizing hierarchical 3D CdS nano-flowers using Lawesson's reagent (LR) as illustrated in Fig. 6e. First, the decomposition of LR in chloroform occurs due to a reaction with cadmium nitrate (aqueous) and forms a monomer that forms a complex with cadmium. Further, this complex

decomposed hydrothermally and results in tiny nuclei of CdS (Fig. 6e(A)) that grows with time. Under, prolonged hydrothermal reaction time, nuclei constructs CdS NPs followed by the growth of anisotropic CdS NSs (thin nanopetals) (Fig. 6e(B and C)) due to aggregation of NPs and finally 3D hierarchical flower-like nanostructures (Fig. 6e(D)) were constructed owing the self-assembly of nanopetals were formed. A 3D CdS hierarchical microtremella morphology was fabricated by Dai *et al.*<sup>117</sup> The solvothermal method with the assistance of EDA was used



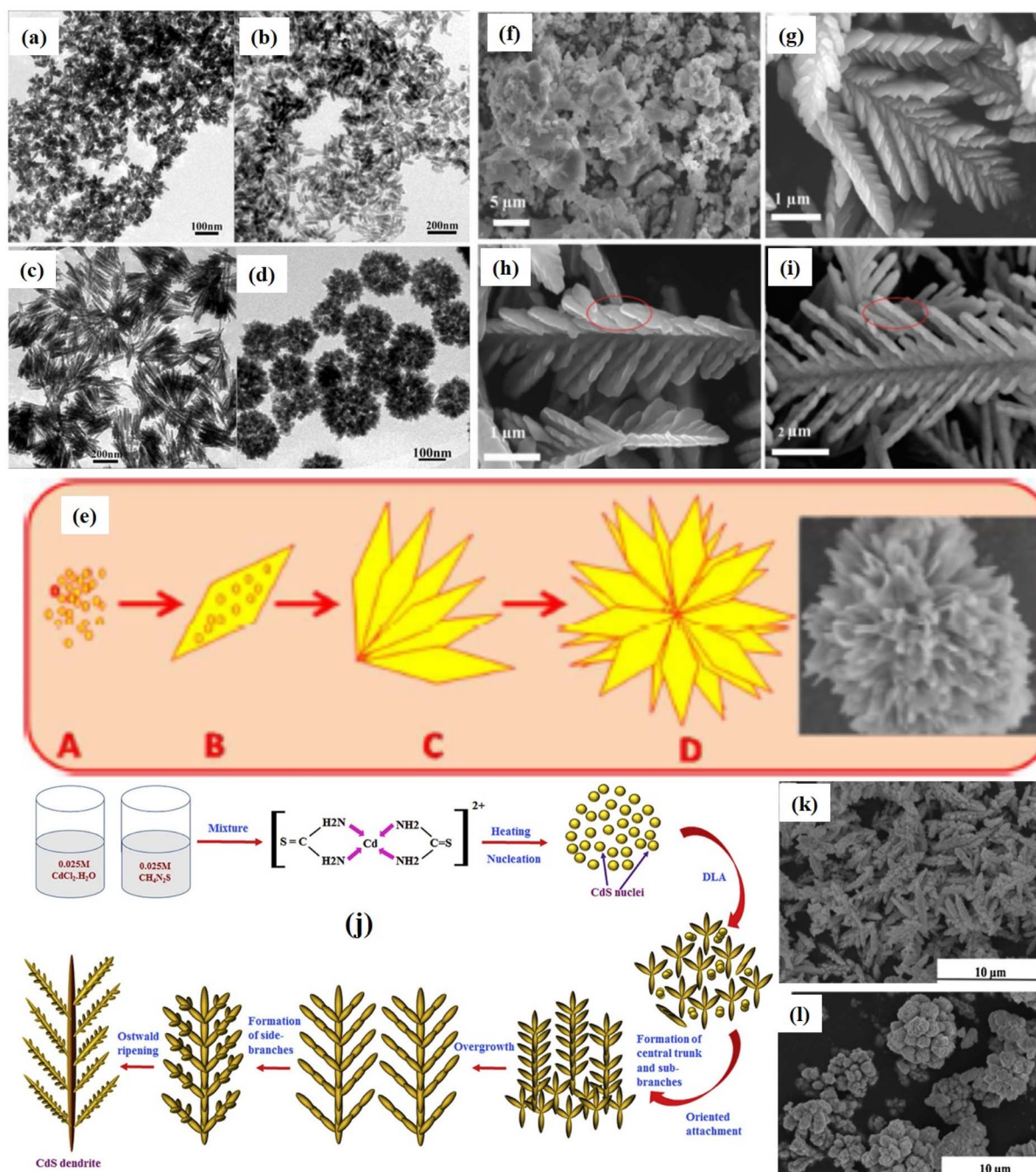


**Fig. 6** (a–d) 3D CdS hierarchical nanostructures *i.e.* water lily, nanorices, nanofans and porous microparticles under different experimental conditions. Schematic representation of the formation of CdS dendrites. Reprinted with permission from ref. 112. (e) Schematic of mechanism of growth of 3D CdS hierarchical nanoflower. Reprinted with permission from ref. 113. Formation of CdS dendrites nanostructures: SEM images of samples prepared at different temperatures: (f) 120, (g) 150, (h) 180, and (i) 220 °C. Reprinted with permission from ref. 114. (j) Schematic of mechanism for the growth of hierarchical CdS dendrites<sup>115</sup> (k and l) Zn-doped dendritic-like CdS structures (k) Zn-doped lower concentration and (l) higher concentration. Reprinted with permission from ref. 116.

to fabricate MT at 60 °C for 12 h. The growth mechanism of the MT structure was described as the dissolution of thiourea in the water releasing  $S^{2-}$  ions slowly due to broken C=S chemical bonds. However due to the excess concentration of  $Cd^{2+}$  ions compared to the concentration of  $S^{2-}$  ions, a fraction of  $Cd^{2+}$  ions form coordination complexes to react with EDA and

restricted the growth of generated CdS NCs largely. Subsequently, NCs gradually aggregated to acquire the shape of minimum surface energy and resulting in the formation of MT. While 3D branched (hierarchical) CdS NS arrays were synthesized through the combination of electro-deposition and subsequent solvothermal methods reaction using EDA as the

solvent, thiourea sulfur source, and hexamethylenetetramine (HMTA) as capping agent. The examination of various factors influencing the morphology indicated that the addition of HMTA ( $\geq 160$  °C) only results in the formation of a branched structure each branch consists of ten thousand of NWs growing preferentially along [0001] direction *via* EDA and HMTA co-assisted gradual crystallization and subsequent self-assembling process and degree on ordering aspect ratio of NWs depends on the concentration of HMTA. In addition, the concentration of sulfur source, temperature, and time are also critical parameters that controlled the aspect ratio of branched NWs.<sup>118</sup>

Interestingly, hierarchical CdS dendrites were demonstrated by Yu *et al.*<sup>114</sup> following the same synthesis strategies but varying the reaction temperature and time. It was observed that dendrites were formed at a certain reaction temperature ( $\geq 150$  °C) for time ( $\sim 24$  h) and a raise in temperature (180 °C) transformed hyperbranched dendrites into shorter branched dendrites. Further, an increase in temperature (220 °C) resulted in the formation of nanorod-branched dendrites (Fig. 6f–i). These CdS hierarchical nanostructures exhibited excellent photocatalytic activities by degrading eosin red nearly completely (over 95%) after visible light irradiation of 100 min. A slightly different influence on the morphology of CdS dendrites nanostructure was reported by Jamble *et al.*<sup>115</sup> as a result by varying the temperature where dendrites were grown at 160 °C and increasing temperature led to the overall growth, density uniformity, yield, and crystallinity of dendrites at 180 °C and then the fragmentation of dendrites into small parts occurred at 200 °C. However, in both cases, as discussed above, a similar mechanism was proposed for the growth of hierarchical CdS dendrites as demonstrated in Fig. 6j. It was proposed that due to the dual role of thiourea as a sulfur source and bidentate ligand, Cd-thiourea stable system was formed first that weakened with raise in temperature and gradually released Cd<sup>2+</sup> ions. Meanwhile, nucleophilic O atoms from H<sub>2</sub>O molecules attack thiourea, leading to the weakening of the C=S bonds and subsequently releasing S<sup>2-</sup> anions. These S<sup>2-</sup> then reacted with Cd<sup>2+</sup> to produce CdS nuclei, which were further grown preferentially to form rod-like CdS nanostructures. Afterward, the secondary branches turned off aligning mutually parallel along the central trunk and growing further along the secondary branches. Finally, anisotropic growth led to the formation of dendritic structures (Fig. 6j). It was demonstrated that the photocatalytic activities of CdS dendrites as synthesized were found to be enhanced with changes in the morphologies with respect to the increase in temperature. An excellent photocatalytic performance was observed by the dendrites obtained at 200 °C attributed to the greater surface area led to the enhanced adsorption property. Similar 3D CdS crystals with dendrites nanostructures were fabricated by Qui *et al.*<sup>119</sup> *via* an amino acid mediated hydrothermal process where various amino acids were used as capping agents. It was suggested that the growth mechanism of structures required a kinetic growth regime (elevated temperature), whereas thermodynamic control (slow growth at low temperature) was essential for growth of isotropic (aspect ratio) structures. The resulting morphologies

exhibited tunability in their optical properties which could be used as ideal building blocks for optoelectronic devices and most importantly as a photocatalyzer attributed to the mixed features of micro and nano-sized crystals. The influence of Zn ions incorporation in growth of dendrite like 3D CdS structure *via* hydrothermal was investigated by Yang *et al.*<sup>116</sup> It was found that low Zn<sup>2+</sup> doping concentration resulted in dendritic-like CdS structures while higher concentrated provided flower-like structures (Fig. 6k and l). These tunability in the morphology improved the photo absorption capability of the overall optical properties with excellent photocatalytic activity.

**2.2.4. Tetrapods nanostructures.** 3D Tetrapod nanostructure is referred to a shape with four arms connected to one center<sup>120–122</sup> as shown in Fig. 7a. Tetrapod nanostructures show very promising technological potential in view of their applications in variety of fields.<sup>122–125</sup> 3D CdS tetrapod nanostructures possess unique morphology with excellent optical and electronic properties for various applications and particularly photocatalytic applications due to their superior light-harvesting ability.<sup>126,127</sup> These nanostructures have gained great attention in the recent past due to their unique structure extended in the surrounding which facilitates their assembly and networking for obtaining/tailoring desired mechanical strength and physicochemical properties.<sup>91,120,127</sup>

Several groups have been working on the synthesis of such tetrapod nanostructures and the tailoring of their properties. For example, Chu *et al.*<sup>128</sup> studied the growth of such 3D CdS tetrapod nanostructures as shown in Fig. 7a and b. It was proposed that the lattice space match and the location match of ions at the interface of the zinc blende (ZB) core and the wurtzite (WZ) arms in the tetrapod structure were responsible and main structural factors for such anisotropic 3D growth. It was also proposed that by mixing the different proportions of the solvents such as ethylenediamine (EDA) and ethylene glycol (EG), wurtzite or zinc blende CdS rich nanostructures could be formed under the solvothermal conditions. Similarly, the influence of reaction temperature and time on the growth of Cd<sub>0.9</sub>Zn<sub>0.1</sub>S nanotetrapods *via* solvothermal using EDA as both solvent and capping agent was studied.<sup>129</sup> The growth mechanism was explained on the basis of the formation of ZB-structured seeds attributed to the temperature-induced nucleation followed by preferential growth of the WZ phase arms (Fig. 7c). It was proposed that the nucleation temperature was the main factor determining the formation of ZB or WZ through nucleation whereas, the monomer deposition and surface diffusion determined the final shape of nanostructures. Furthermore, it was concluded that a relatively low reaction temperature favored the ZB tetrahedral nucleation and subsequent growth initiated *via* growth monomers depositing ( $V_{\text{deposition}}$ ) at one of the ZB-(111) facets of the tetrahedron seed with restricting their diffusion. The growth thus assisted along one direction only led to the formation of nanorods (Fig. 7c, situation 1). At moderate temperature, surface diffusion ( $V_{\text{diffusion}}$ ) is initiated, leading to access to other ZB-(111) facets by adsorbed monomers and formed multipods along with nanorods (Fig. 7c, situation 2). The diffusion effect dominated at the elevated reaction temperature, and eventually promoted

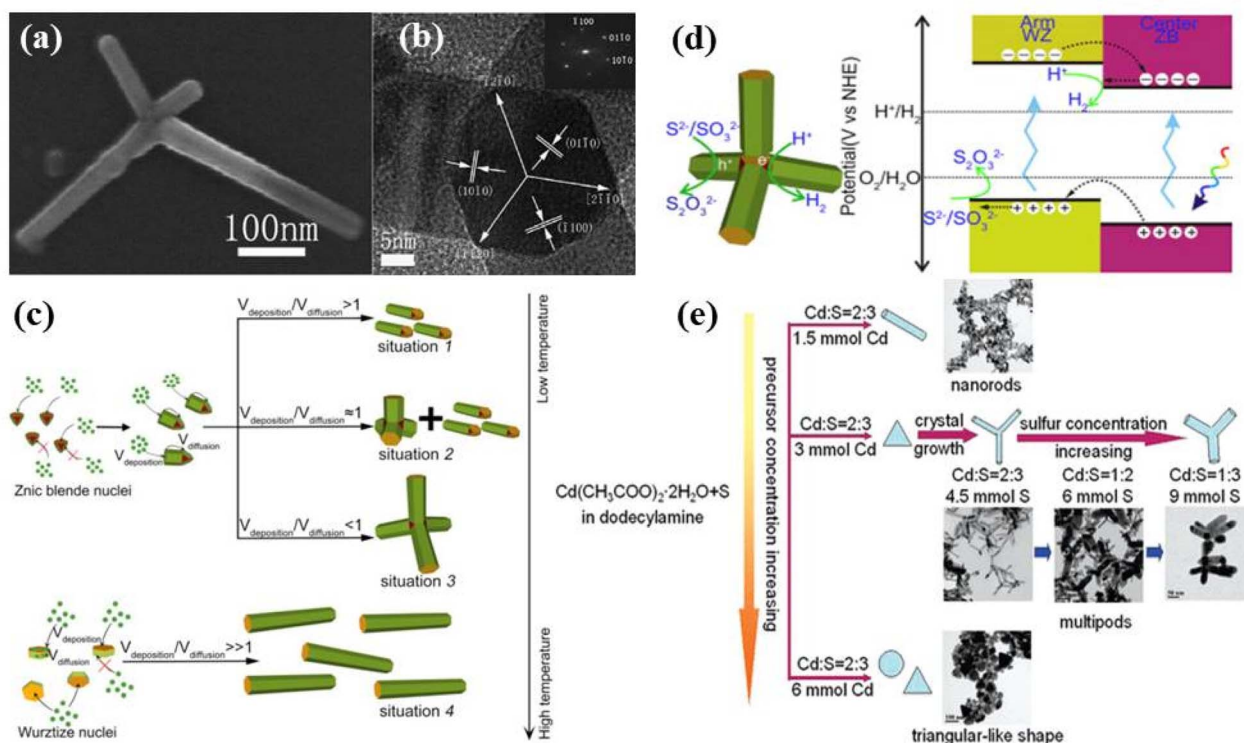


Fig. 7 (a) TEM and (b) HRTEM images of 3D CdS nanotetrapod. Reprinted with permission from ref. 128. (c) Schematic illustrations showing the formation mechanism of different morphologies of  $\text{Cd}_{0.9}\text{Zn}_{0.1}\text{S}$  nanostructures at different temperatures. (d) Mechanism for photogenerated charge separation as well as the redox reaction around the WZ-ZB homojunction. Reprinted with permission from ref. 129. (e) Schematic illustration of the formation process of CdS nanostructures. Reprinted with permission from ref. 130.

the formation of tetrapod nanostructures (Fig. 7c, situation 3). In contrast, at a temperature high enough, the nucleation mode switched from ZB tetrahedron to WZ hexagonal plate and growth started at one of the WZ-(0001) facets leading to the formation of WZ nanorods (Fig. 7c, situation 4). A similar argument could be applied to the intermediate case, where only a portion of the nuclei take the WZ hexagonal shape and the resultant product lay between situations 3 and 4. The photocatalytic studies showed that such nanotetrapods exhibited superior photocatalytic hydrogen production due to their high crystallinity and an atomically well-matched phase junction conveniently generated the ZB core and WZ arms (Fig. 7d).<sup>129</sup> Here, it is important to mention that temperature plays an important role in determining the stages of formation of tetrapod structures along with the crystal structure. It also provides the formation mechanism of the tetrapod providing the stepwise information during the synthesis of such tetrapod nanostructures.

Interestingly, 3D hierarchical CdS nanotetrapods with tunable optical properties by controlling the length and diameter of the arms of the tetrapod were proposed by Wang *et al.*<sup>130</sup> It was observed that the arm diameter of CdS multipods could be tuned (from 10 to 60 nm) by increasing the S concentration and length could be controlled by varying the reaction time as shown in Fig. 7e. Similarly, Yu *et al.*<sup>131</sup> also synthesized multi-armed CdS tetrapods and observed excellent photocatalytic  $\text{H}_2$ -production activity under visible light with Pt as a co-catalyst

attributed to the synergistic effects of several factors including hexagonal phase structure, high surface area, great pore volume and good crystallization. The tetrapods were found to be photostable and no photocorrosion was observed after photocatalytic recycling. It has been found that the shape and composition controlled synthesis of such nanostructures provides better control over the physiochemical properties. Similarly, Vaneski *et al.*<sup>132</sup> demonstrated room temperature aqueous synthesis of CdS tetrapod nanostructures in  $\text{H}_2\text{O}/\text{EDA}$  mixtures and tested the effect of the addition of common ligands like mercaptopropionic acid (MPA), thioglycolic acid (TGA), and cysteine for their ability to stabilize the colloidal CdS tetrapod nanostructures. It was noticed that the reaction was completed within 3 days without any significant difference in arm length of the tetrapod nanostructures on the addition of ligands. This simple method offered advantages for the subsequent direct use of aqueous-based colloidal CdS nanostructures for photocatalytic hydrogen generation from water avoiding any additional phase transfer.

In summary, growth of CdS tetrapod structures by hydrothermal/solvothermal process is preferably initiated when seed nuclei are in cubic phase and anisotropic growth of hexagonal branches occurs at elevated temperature (usually  $\geq 160$  °C). The Cd/S molar ratio plays a critical role for different morphologies and tetrapod structures result when this ratio becomes smaller (nearly  $0.6 \leq$ ). The length of the arms of tetrapod can be controlled by precursors' molarities, for

a constant molar ratio, higher the molarities longer the arms. Additionally, the arm length also depends on the reaction time, larger the processing time longer the arm length and lesser the arm diameter, however reaction time do not affect morphology significantly. Besides, the length of tetrapod arms also depends on type of sulphurous precursor.

**2.2.5. Other micro/nano structures.** As discussed above, several 3D CdS nanostructures have been synthesized and various parameters have been optimized in order to produce 3D nanostructures with better morphological as well as photoelectronic/photocatalytic properties. Furthermore, there are some other 3D CdS nano-architectures that have shown better morphological properties and have the potential to be good candidates for several applications. For example, Wang *et al.*<sup>133</sup> demonstrated one pot synthesis of CdS NCs of various shapes, from nanocone to nanofrustum, to nanoplate and proposed that the designed growth pattern involved diffusion of

growth monomers driven by chemical potential as shown in Fig. 8a and b. It was also proposed that by engineering the facet growth *via* quantitatively controlling the addition of the metal precursor and adjustment of the reaction kinetics, CdS NCs of various shapes could be prepared along with shape-dependent photocatalytic activities. The growth mechanism involved the formation of CdS monomers due to the injection of metal ions ( $\text{Cd}^{2+}$ ) and their diffusion from the bulk solution to the surface of crystal nucleus/seeds. Successively, the deposition of monomers at certain surface planes (either  $\{0001\}$  facets or  $\{10\bar{1}1\}$  facets depending on the surface energies of facets and the chemical potential generated by the concentration) of grown monomers of the nucleus/seeds occurred followed by surface diffusion and reconstruction. Finally, the shape of the crystal can be adjusted by simply regulating the growth rates of the monomers on  $\{0001\}$  facets ( $r_1$ ) and  $\{10\bar{1}1\}$  facets ( $r_1'$ ), as illustrated in Fig. 8b. In addition, the deposited clusters may also

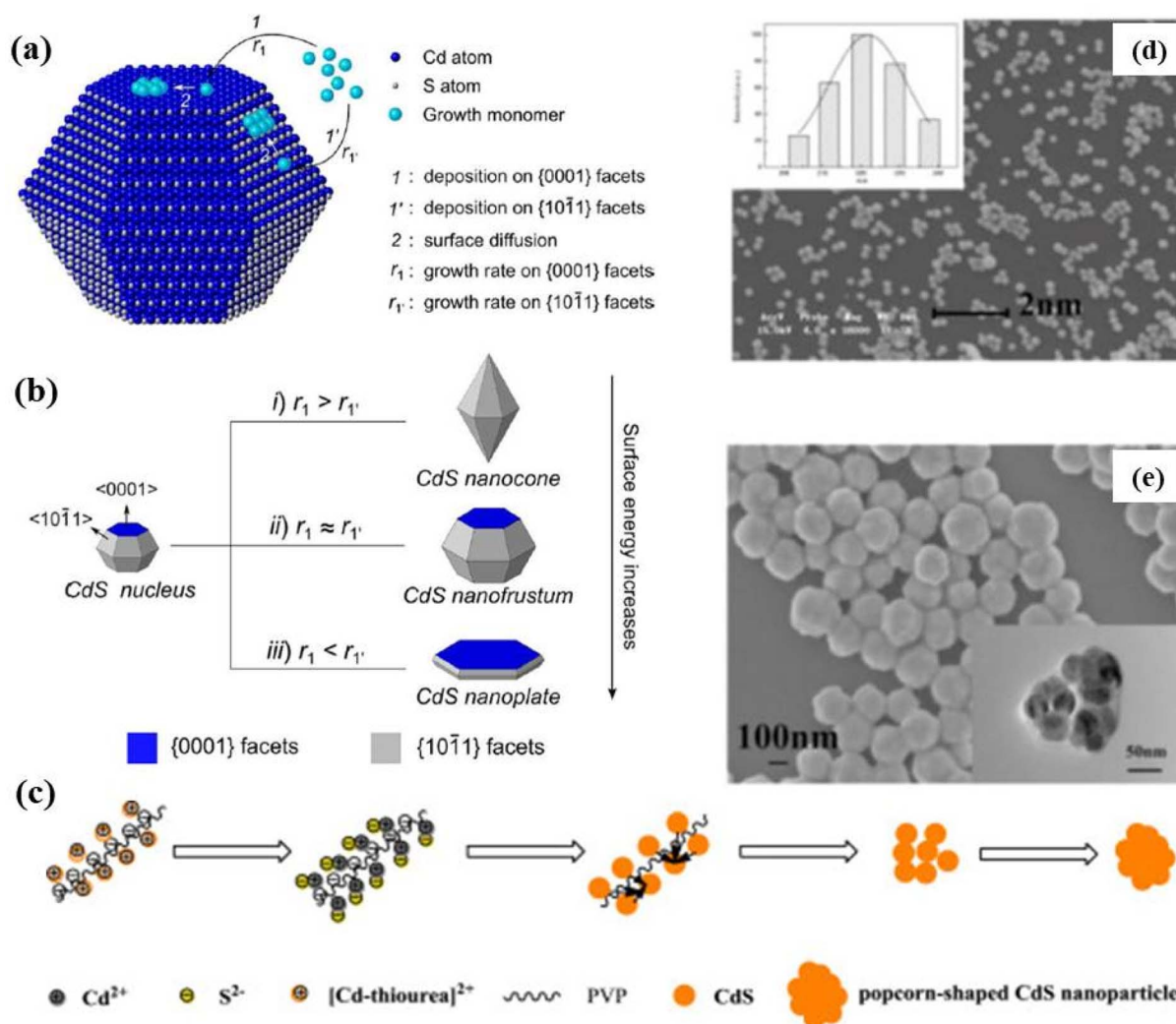


Fig. 8 Schematic illustration of (a) the major steps involved in the growth process and (b) the formation of a CdS nanocone, a CdS nanofrustum, and a CdS nanoplate, simply controlled by adjusting  $\text{Cd}^{2+}$  injection rate. Reprinted with permission from ref. 133. (c) Mechanism of the reaction in the formation of popcorn-shaped CdS nanostructures (d) SEM image with particle size distribution (inset), (e) FESEM and TEM (inset) images of CdS popcorn NPs obtained with  $20 \text{ mmol L}^{-1}$  thiourea and  $4 \text{ g L}^{-1}$  PVP for 24 h. Reprinted with permission from ref. 134.

undergo a surface diffusion process to make the crystal grow into more mature ones.<sup>133</sup> It was found that CdS nanoplates with the largest (0001) facets showed the best results in terms of photocatalytic activity.

On the other hand, Zhang *et al.*<sup>134</sup> demonstrated the synthesis of popcorn-shaped CdS NPs with potent photocatalytic activity by hydrothermal reaction for 24 h at a certain temperature with and without using PVP-K30 as a surfactant. It was considered that CdS nuclei generated from the reaction of Cd<sup>2+</sup> and S<sup>2-</sup> ions that produced due to the decomposition of [Cd-thiourea]<sup>2+</sup> with increasing temperature. Further, the continuous growth of crystal was prevented due to selective adsorption/desorption of organic ligands on the defined crystal plane of CdS and resulted in popcorn-shaped CdS NPs (Fig. 8c). The SEM image in Fig. 8d shows that CdS NPs with regular and uniform spheres of diameter 220 nm were obtained (the inset shows the size distribution). Further investigations were carried out by high-resolution SEM and TEM. Fig. 8e shows the HRSEM image of CdS NPs which were found to be with rough surfaces resulting from the aggregation of small spheres (sizes about 30–50 nm), forming popcorn-shaped NPs as clearly shown by TEM image (inset of Fig. 8e). On the other hand, it was found that CdS NPs synthesized without surfactants *i.e.* PVP showed different morphology that looked like nanoflowers. It was concluded that CdS NPs prepared using PVP formed like popcorn-shaped CdS NPs whereas, without PVP, the structure followed nanoflowers formation with a rough surface. This indicated that the surfactant *i.e.* PVP played an important role in tailoring the shape of the CdS NPs. Interestingly, it was observed that as compared to CdS nanoflowers, popcorn-shaped CdS NPs showed a much higher visible-light photocatalytic degradation activity with a rate of 93.3% in 4 h. The popcorn-shaped structure possesses the unsmooth surface with larger surface area and more active sites due to pores structures.

Recently, Kong *et al.*<sup>135</sup> reported the synthesis of hexagonal CdS cones *via* urothermal reactions at 80–120 °C for 4–12 h as shown in Fig. 9 and its growth was attributed to the dissolution and recrystallization process. It was proposed that during the grinding process of precursors small amount of S<sup>2-</sup> escaped and promoted the cubic phase of CdS at beginning of the reaction. However, with the passage of time and an increase in temperature, more and more S<sup>2-</sup> released from thiourea and formed hexagonal CdS nuclei that grew anisotropically along the polar direction (0001) during the prolonged reaction and formed hexagonal CdS cones (Fig. 9). Interestingly, photocatalytic investigations on water splitting under visible light ( $\lambda \geq 420$  nm) revealed that hexagonal CdS cones showed a better photocatalytic property ( $10.5 \text{ mmol h}^{-1} \text{ g}^{-1}$ ) as compared to that of other nanostructures attributed to the exposure of (0001) active crystal plane. Whereas, a 3D sponge-like microporous CdS film was prepared by Feng *et al.*<sup>136</sup> using solvothermal treatment of Ti pale with a seed layer for 24 h at various temperatures. The Ti pale with a seed layer was prepared by spin coating of seed layer solution over the Ti plate followed by thermal annealing at 500 °C for 2 h. It was observed that the raise in temperature increases grain size from a hundred nm to a few  $\mu\text{m}$ . The 3D CdS thin-film photoelectrode exhibited excellent photoelectrochemical performance and stability along with high photoelectric conversion efficiency.

In brief, the above discussion on synthesis of various 3D CdS based nanostructures using different approached resulting in different 3D morphologies with tunable dimensions and optical properties provide a complete overview of the formation mechanism of such nanostructures. It provides a pathway to tune the photocatalytic properties of the materials based on the morphologies and structural changes for enhanced photocatalytic efficiencies in different fields. Various parameters during the synthesis of such nanostructures play important role in designing their morphologies and dimensions. Additionally,

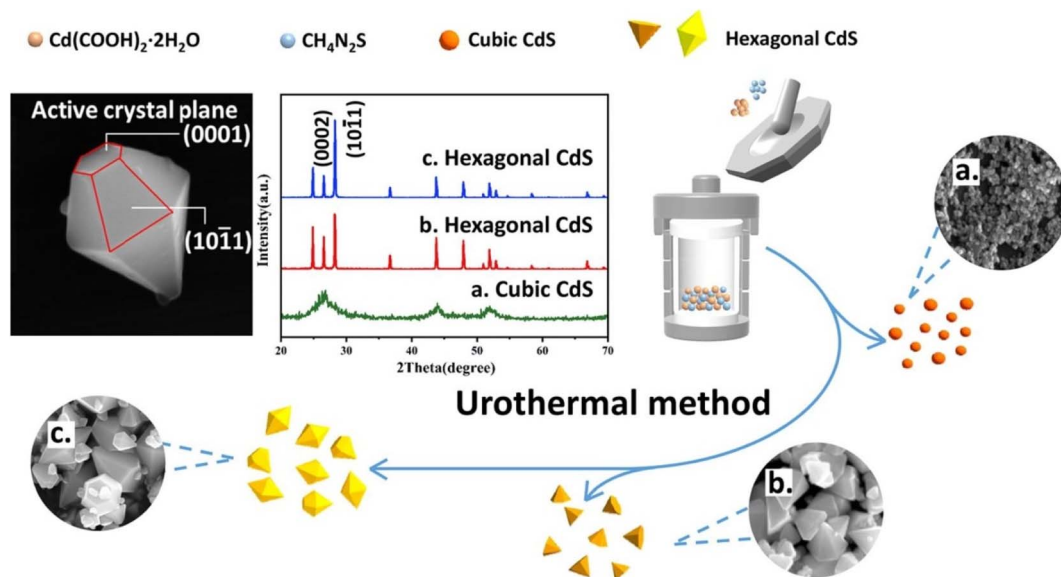


Fig. 9 Synthesis of hexagonal CdS cones *via* urothermal reactions. Reprinted with permission from ref. 135.

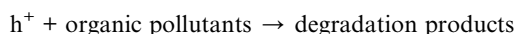
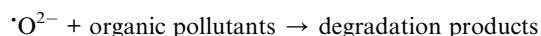
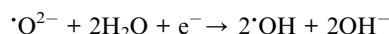
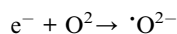
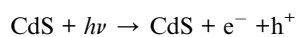
the starting materials, their concentrations followed by key reaction experimental parameters also play important role in finalizing the materials architectures. Therefore, various approaches used for the synthesis of 3D CdS based photocatalysts, starting materials, synthesis parameters, resulting morphologies with dimensions are summarized in Table 1. This not only provide the comparative strategies of synthesizing 3D CdS nanostructures but also to find the suitable parameters to design and engineering such nanostructures with enhanced photocatalytic properties.

### 3. Mechanism and visible light photocatalytic applications of CdS-based 3D nano/micro-architectures

Removal of organic pollutants from wastewater using CdS-based photocatalysts has been extensively studied in the past few years. The use of such photocatalysts is an ecological and efficient way for wastewater treatment due to its visible light photocatalytic activity which is promising for various energy and environmental applications. These 3D nanostructures have extensively been studied for improved photocatalytic action in the field of degradation of organic pollutants. Additionally, these CdS 3D nanoarchitectures are being used as promising and emerging nanomaterials in photocatalytic H<sub>2</sub> production as well as CO<sub>2</sub> reduction. This section includes recent advancements in mechanism and visible light photocatalytic applications of CdS-based 3D nanostructures in photocatalytic degradation of various emerging organic pollutants, photocatalytic H<sub>2</sub> production and photocatalytic CO<sub>2</sub> reduction.

#### 3.1. Photocatalytic degradation of emerging organic pollutants

**3.1.1. CdS-based sole 3D nano-architectures.** The semiconductor nanomaterials under irradiation with photon energy larger than band gap energy generally generate electron-hole pairs. In the case of CdS nanostructures, under visible or sun light irradiation, the photogenerated charge carriers undergo the following reaction mechanism resulting in the photodegradation of organic pollutants:



Firstly, there are the generation of electron-hole pairs in CdS semiconductors under visible light irradiation. After absorption of photon energy, equal to or larger than the band gap energy of CdS nanostructures, the holes (h<sup>+</sup>) are generated in the valence band (VB) and electrons (e<sup>-</sup>) are generated in the conduction

band (CB). The photogenerated charge carriers react with absorbed oxygen (O<sub>2</sub>) or water (H<sub>2</sub>O) molecules on the surface of the photocatalysts from the environment resulting in the formation of reactive oxygen species. Generally, photogenerated electrons reduce (O<sub>2</sub>) to superoxide anion radicals ( $\cdot\text{O}_2^-$ ), which were then partially transformed into hydroxyl radicals ( $\cdot\text{OH}$ ). These hydroxyl radicals ( $\cdot\text{OH}$ ), can decompose organic pollutants effectively into carbon dioxide (CO<sub>2</sub>), water (H<sub>2</sub>O), and simple inorganic by-products.<sup>21,139</sup> The mechanism behind the photocatalytic action of the CdS semiconductor has been shown schematically in Fig. 10.

It has been reported that the optical and photocatalytic properties of CdS nanostructures and their corresponding applications significantly depend on the morphology including shape and size, *i.e.* nano-architecturing of the nanostructures.<sup>23,25</sup> 3D CdS nanoarchitectures as compared to other morphologies have shown promising applications in the field of photocatalytic degradation of emerging organic pollutants. Iqbal *et al.*<sup>65</sup> fabricated CdS nanoflowers and CdS nanopetals *via* the hydrothermal process which were confirmed by SEM micrographs as shown in Fig. 11a–d. The compositional and structural analyses were confirmed by EDS and XRD (Fig. 11e and f respectively). The EDS showed the presence of Cd and S elements whereas the XRD patterns exhibited the formation hexagonal phase in both structures. Furthermore, their optical and electrical properties were studied along with photocatalytic activities against Rhodamine B (RhB) dye molecules. The optical properties exhibited that the CdS nanoflower had a lower band gap (2.3 eV) as compared to the nanopetal (2.39 eV) as shown in Fig. 11g and h attributed to the quantum confinement effects. The photocatalytic degradation of RhB was found to be more effective in the case of CdS nanoflowers (78%) as compared to that of nanopetals (Fig. 11i and j). The higher photodegradation efficiency of CdS nanoflowers was explained by greater charge separation as studied by electrochemical impedance spectroscopy which confirmed that the 3D nano-architecture of CdS nanoflowers facilitated the separation of the photogenerated.

Yang *et al.*<sup>71</sup> demonstrated that 3D flower-like CdS nanostructures with cubic phase and CdS NPs with hexagonal phase as determined by field emission SEM (FESEM) micrographs and XRD patterns showed excellent photocatalytic degradation ability. However, it was shown that 3D flower-like CdS nanostructures with a band gap of 2.25 eV exhibited greater photocatalytic activity as compared to CdS NPs. The highest degradation rate of flower-like CdS was found to be 90.4% for MB, whereas in the case of CdS NPs degradation rate was found to be around 88% showing the promising optical and photocatalytic behavior of CdS nanoflowers structures. These CdS 3D nanostructures are also very effective in thin film coating on various surfaces for photocatalytic degradation. Recently, it was shown by Aboud *et al.*<sup>140</sup> that CdS nanoflower-based thin films exhibited unprecedented photocatalytic activities for the decomposition of MB and methyl violet (MV) dyes which were attributed to the high surface area, low energy band gap, and efficient charge separation properties for prepared CdS films.

Table 1 Various synthesis approaches, experimental parameters, structures/phases, morphologies/shape and sizes of 3D CdS nanostructures<sup>a</sup>

Synthesis method	Precursors and concentrations		Reaction key parameters				Morphology and dimensions (nm)	Phase	Ref.
	Cd	S	pH	T (°C)	t (h)	Concentration of solvent			
Hydrothermal	Cd(NO <sub>3</sub> ) <sub>2</sub> 3 mmol	TU 1 mmol	CA = HMT	DI	200	12	NFs ( <i>d</i> = 250)	Wz	63
	Cd : S 1 : 0.5				200	12	Spheres approx. NFs branched (5 to 8 pods) ( <i>l</i> = 150, <i>d</i> = 100) NFs		
	1 : 1								
	1 : 2								
	1 : 3								
	Cd : S = 3 : 1				120	12	Ball-like (400) imperfect NFs perfect NFs		
					160				
					200				
	CdCl <sub>2</sub> 1 g	TAA 0.75 g	CA = NMA	ET (50 ml)	120	1	Nanopetal	Wz	65
	Cd(NO <sub>3</sub> ) <sub>2</sub>	TU	DI (50 ml)	CA = PVP	150	4			
					150	1	NFs		
					180	6			
	[Cd (TSC)Cl <sub>2</sub> 0.8 g		DI (50 ml)		150	12	NFs	Wz	137
	CdCl <sub>2</sub> 3 mmol	TU 6 mmol + EN	DI		100	5	Nanospheres	Zb	71
		3 mmol					Flower		
		6 mmol							
		9 mmol					Flower		
		12 mmol					Flower surface collapses		
		TU + EN + SDBS					Flower		
		3.3 mg ml <sup>-1</sup>					Flower ( <i>d</i> = 10 μm)		
		6.7 mg ml <sup>-1</sup>					Flower ( <i>d</i> = 13 μm)		
		10 mg ml <sup>-1</sup>					NPs	Wz	119
		1.3 mg ml <sup>-1</sup>			160	12			
	Cd(NO <sub>3</sub> ) <sub>2</sub> 0.01 mol	Na <sub>2</sub> S 0.03 mol	DI		200	4	Dendritic (4–6 μm)	Wz	
	Cd(NO <sub>3</sub> ) <sub>2</sub> 1 mmol	TU 3 mmol	CA (0.3 mmol)				Dendritic		
			<i>l</i> -Valin				Spindle		
			Proline				NPs (40–50)		
			Serine				Flower-like		
			Cysteine				Hierarchical		
			Methionine				Branched		
			Histidine				Cauliflower		
			Tryptoplan		200	2	Dendritic with short and irregular trunk and braches		
			DI				Dendritic with very long and regular trunk and braches		
			CA (0.3 mmol)			4	Dendritic with reduced regularity		
			<i>l</i> -Valin			8	Dendritic with reduced regularity further		
					160	4	Urchin-sphere		
					180		Urchin-sphere		
					200		Dendrites		

Table 1 (Contd.)

Synthesis method	Precursors and concentrations		Concentration of solvent	Reaction key parameters		Morphology and dimensions (nm)	Phase	Ref.				
	Cd	S		pH	T (°C)				t (h)			
Solvothermal	Cd(NO <sub>3</sub> ) <sub>2</sub> 2 g	Lawesson's reagent 0.7 g	DI 100 ml	DI	220	Dendrites						
				CA = <i>l</i> -Valin	200	200	4					
				0.0 mmol								
				0.3 mmol								
				0.9 mmol								
				1.8 mmol								
				90	10	10	10	10	10	10	10	
				15	15	15	15	15	15	15	15	
				5	5	5	5	5	5	5	5	
				0.5	0.5	0.5	0.5	0.5	0.5	0.5	0.5	
Solvothermal	Cd(Ac) <sub>2</sub> 1.4 mmol	TAA 2 mmol	EN (%) : EG (%)	0 : 100	150	NPs (8)	Zb	128				
				50 : 1	180	NPs (13)	Wz					
				5 : 95		Multi rods ( <i>l</i> = 20, <i>d</i> = 10)						
				15 : 85		Multi rods ( <i>l</i> = 40, <i>d</i> = 15)						
				50 : 50		Tetrahedrons and spheres (64)						
				65 : 35		pencil-shaped rods ( <i>l</i> = 49, <i>d</i> = 20)						
				160	5	Tetrapod ( <i>l</i> = 206, <i>d</i> = 22.5) prickly spheres						
				180		Hexagonal nanoprisms ( <i>l</i> = 748, <i>w</i> = 35)						
				210		Tetrapod ( <i>l</i> = 100–600, <i>d</i> = 20) prickly spheres nanorods						
				Solvothermal	Cd(Ac) <sub>2</sub> 18 mmol	TAA 25 mmol	EN 30 ml	140	24	Nanorods ( <i>d</i> = 10)	Zb-centre (80 nm) with wz-arms (200 nm) W	129
160		Nanorods with multipods										
180		Tetrapods										
200		Tetrapods (large dimensions)										
220		Nanorods										
220	4	Irregular shape nanorods ( <i>l</i> = 13, <i>d</i> = 6)	Wz + Zb					130				
		Multipods ( <i>d</i> = 10)	Wz									
		Multipods ( <i>d</i> = 40)	Wz									
		Multipods ( <i>d</i> = 60)	Wz									
		Multipods ( <i>d</i> = 60)	Wz									
		Nanorods ( <i>l</i> = 45, <i>d</i> = 15)	Wz + Zb									
		Irregular shape (90)	Wz									
		Triangular	Wz + Zb									
Solvothermal	Cd(Ac) <sub>2</sub> 3 mmol	S powder	DAA (15 ml)	100	4	Nanorods ( <i>l</i> = 25, <i>d</i> = 5)	Wz					
				140		Multipods	Wz					
				180		Nanorods	Wz					
				100		Nanorods ( <i>l</i> = 35, <i>d</i> = 5)	Wz					
				140		Multipods	Wz					
				180		Multipods	Wz					
				220	24	Multipods ( <i>l</i> = 70, <i>d</i> = 10)	Wz					
				60	60	Multipods ( <i>l</i> = 100, <i>d</i> = 10)	Wz					
				Solvothermal	Cd(Ac) <sub>2</sub> 3 mmol	TAA 25 mmol	DAA (15 ml)	100	4	Nanorods ( <i>l</i> = 25, <i>d</i> = 5)	Wz	
								140		Multipods	Wz	
180		Nanorods	Wz									
100		Nanorods ( <i>l</i> = 35, <i>d</i> = 5)	Wz									
140		Multipods	Wz									
180		Multipods	Wz									
220	24	Multipods ( <i>l</i> = 70, <i>d</i> = 10)	Wz									
60	60	Multipods ( <i>l</i> = 100, <i>d</i> = 10)	Wz									



Table 1 (Contd.)

Synthesis method	Precursors and concentrations		Reaction key parameters			Morphology and dimensions (nm)	Phase	Ref.	
	Cd	S	Concentration of solvent	pH	T (°C)				t (h)
Cd(Ac) <sub>2</sub>	10 mmol	TAA 15 mmol	DAA (50 ml) DI (50 ml)		100 140	12	Nanorods Nanorods Multi-armed rods Multi-armed rods	Wz Wz Wz Wz	131
					180		NPs (20) NPs NPs (50)	Wz + Zb Wz + Zb Wz + Zb	
CdCl <sub>2</sub>	1.14 g	TU 0.38 g S powder	DI (10 ml) + EN (20 ml)		60	12	Hierarchical	Wz	117
	1.5 mmol	TAA Na (DDTC) 4.5 mmol TU 10 mmol	OM : OTA 1 : 1		90	16	Tetrapod (l = 21.9, d = 10) Tetrapod (l = 84, d = 11.8) Tetrapod (l = 20.9, d = 6.8)	Wz Wz Wz	138
Cd(Ac) <sub>2</sub>	2 mmol		DETA : ET : DI 2 : 1 : 0 2 : 1 : 0.2 2 : 1 : 0.5 2 : 0 : 1		80	48	Flower Porous flower Belt-like Net-like	Wz Wz + Zb Wz + Zb Wz + Zb	92
			DETA : DI 6 : 1 1 : 1 2 : 5 1 : 6 DETA : DI 6 : 1 CA = HAD EN (18 ml)		180	12	Branched NWs Cage-microspheres Urchin like NFs (3.5 μm) Microspheres Micro-trees	Wz Wz Wz + Zb Wz + Zb Wz	93
CdS NPs (6 nm)	0.1 g				140	2 h	Nanorods (l = 400, d = 40)	Wz	121
	0.2 g 0.5 g 0.2 g				150	5 h	Nanorods (l = 2900, d = 40) Nanorods (l = 1400, d = 40) Nanorods (l = 800, d = 40)	Wz Wz Wz	
CdS NPs (6 nm)		S powder			180		Twinrod (l = 10–50, d < 6) tetrapod	Wz Wz	
	0.3 g CdS	CdS : S = 1 : 6							
Others									
CVD	CdS powder		Ar flow (150 sscm)		800	15	NPs (μm) Flowers	Wz Wz	97
					60	3	NFs (3 μm)	Wz + Zb	96
CBD	Cd(NO <sub>3</sub> ) <sub>2</sub>	0.05 M	TEA (0.04 M) + HCL (0.01 M)		60	8	NFs (700–2000)	Wz + Zb	
					90	12	NFs + Cube	Wz + Zb	
CC	Cd(Ac) <sub>2</sub>	0.05 mol L <sup>-1</sup>	CTAB 0.05 mol L <sup>-1</sup>		90	0.5	NFs (d = 30)	Wz	23

<sup>a</sup> CBD = chemical bath deposition, CVD = chemical vapour deposition, CC = colloidal chemistry, Zb = zinc blende, Wz = wurtzite Ac = acetate (CH<sub>3</sub>COO), TAA = thioacetamide (C<sub>2</sub>H<sub>5</sub>NS), EN = ethylenediamine [C<sub>2</sub>H<sub>4</sub>(NH<sub>2</sub>)<sub>2</sub>], EG = ethylene glycol [(CH<sub>2</sub>OH)<sub>2</sub>], DAA = dodecylamine (C<sub>12</sub>H<sub>27</sub>N), Na(DDTC) = sodium diethyldithiocarbamate (C<sub>5</sub>H<sub>10</sub>NS<sub>2</sub>Na), OM = Oleylamine, OTA = oleylamine, TU = thiourea [(NH<sub>2</sub>)<sub>2</sub>CS], HMT = hexamethylenetetramine [(CH<sub>2</sub>)<sub>6</sub>N<sub>4</sub>], ET = ethanol (C<sub>2</sub>H<sub>5</sub>OH), NMA = N-methylamine [C<sub>2</sub>H<sub>5</sub>NH(CH<sub>3</sub>)], TSC = thiosemicarbazide [(NH<sub>2</sub>)<sub>2</sub>NHCS], PVP = polyvinylpyrrolidone, DETA = diethylenetriamine [HN(CH<sub>2</sub>CH<sub>2</sub>NH<sub>2</sub>)<sub>2</sub>], TEA = triethanolamine (C<sub>6</sub>H<sub>15</sub>NO<sub>3</sub>), CTAB = cetyltrimethylammonium bromide (C<sub>19</sub>H<sub>42</sub>BrN), HAD = hexadecylamine (C<sub>16</sub>H<sub>33</sub>N).



Fig. 10 Representing photoactivity of CdS NPs on organic molecules under visible light irradiation.

Ganesh *et al.*<sup>95</sup> synthesized polyvinylpyrrolidone (PVP) capped CdS flower-like morphology consisting of sword-like nanorods as shown in Fig. 12a. Structural investigation was carried out using XRD pattern and bright field TEM as well as HR-TEM images of the CdS nanostructures which indicated a phase transition from the cubic zinc blend to the hexagonal phase of CdS powder when reaction time was increased during the synthesis. The photocatalytic activity of PVP-capped CdS flowers exhibited fast degradation of RhB dye (95% for 120 min) under visible light as shown in Fig. 12b. Similarly, Mao *et al.*<sup>23</sup> reported porous CdS nanoflowers with good photocatalytic properties against RhB. In this work, authors used the cationic ligand protection effect and the template effect of CTAB for the obtaining of uniform 3D porous CdS nanoflowers which not only served as the stabilizing surfactant for CdS but also as the organic template for the formation of 3D CdS mesoporous nanoarchitecture. The morphology was investigated by means of TEM and scanning TEM (STEM) which indicates spherical nanostructures of diameter around 30 nm. Further, SAED pattern exhibited the polycrystalline nature with high crystallinity of the CdS nanostructures. These CdS nanoflowers showed much better efficiency in the degradation of RhB compared with P25 due to the porous structure, and high photo stability with the protection of CTAB (Fig. 12c).

It is clear from the above discussion that the morphology of the CdS nanostructures is very important for tailoring the optical properties to harness the visible light for real practical applications. 3D nano-architecturing of CdS nanostructures is promising for tuning the various morphologies with the desired properties and has the potential to apply for various applications in the field of energy and environment. Furthermore, coupling these 3D CdS nanostructures with other functional nanomaterials or nanocomposite formation could enhance their optical and photocatalytic activities along with their stability which have been discussed in the next sections.

**3.1.2. CdS/carbon nanomaterials based 3D nano-architectures.** As discussed above, various CdS nanoarchitectures exhibited excellent photocatalytic visible light activity. However, the high recombination rate of photogenerated charge carriers makes it less efficient for photocatalytic applications.<sup>141</sup> To improve the photocatalytic efficiency and lower the recombination rate of photogenerated charge carriers, these

nanostructures have been modified by several ways. One of the simple ways is the coupling of CdS nanostructures with other semiconductors or functional nanomaterials. Several carbon-based nanomaterials including graphene nanostructures, polymers, *etc.* have been found very suitable for this purpose because of their excellent electron mobility properties.<sup>141–144</sup> Cui *et al.*<sup>142</sup> demonstrated that encapsulation of CdS in carbon nanotubes (CNTs) could be beneficial to avoid aggregation of CdS NPs. It further resulted in reduced surface area and enhanced photocorrosion inhibition. The combination with such carbon nanomaterials also provides photostability as well as a synergistic effect between CdS and carbon nanostructures resulting in enhanced photocatalytic activity of nanocomposite. Bhavsar *et al.*<sup>145</sup> synthesized activated carbon-loaded CdS nanoflower-based visible light photocatalyst for the removal of RhB dye molecules. The nanocomposites were confirmed by TEM and HRTEM analysis exhibiting CdS nanoflower like morphology with distinct grain boundaries. Additionally, SAED pattern exhibited the crystalline nature of the AC-CdS nanocomposite. The activated carbon and CdS nanoflower-based nanocomposites exhibited excellent adsorption of dyes and charge separation activities resulting in enhanced photocatalytic performance as compared to the CdS nanoflowers. It was concluded that the enhanced photocatalytic performance was due to the synergistic effect of adsorption and the enhanced photocatalysis process.

The conducting polymers are one of the promising materials that consists of  $\pi$  conjugated system that involves the delocalization of  $\pi$  electrons and provides excellent conducting properties. Sharma *et al.*<sup>141</sup> synthesized CdS/polyaniline (PANI) nanocomposite with different CdS morphologies like nanoflowers and nanorods. Through photoluminescence analysis, it was found that coupling of these CdS nanostructures with PANI showed better charge transfer producing more photogenerated  $e^-$  and  $h^+$  pairs as compared to CdS nanostructures. It was concluded that introducing PANI in CdS nanostructures facilitated the charge transfer at the interface and reduced the recombination rate of the photogenerated charge carriers. CdS nanoflowers/PANI nanocomposite exhibited better photocatalytic activity towards photodegradation of MB dye molecules as compared to only CdS nanoflowers and nanocomposites with nanorods which were attributed to the formation of higher interfacial sites between CdS nanoflowers and PANI. Recently, 3D hierarchical PANI/CdS nanocomposite, synthesized by hydrothermal and chemical route forming heterojunction photoanode system, were shown to exhibit significantly enhanced visible light driven photocatalytic and photoelectrochemical (PEC) activity.<sup>146</sup>

Fig. 13 shows the SEM, TEM, and HRTEM micrographs of the 3D CdS and PANI/CdS nanocomposite nanoarchitectures. 3D CdS nanoflowers were formed with a length of a few microns (Fig. 13a and c) which consisted of several interconnected primary branches originating from a common center. Further growth of many secondary branches led to the formation of nanocorn-like structures (Fig. 13c). Fig. 13b and d show the SEM micrographs of PANI/CdS nanocomposite showing the presence of CdS backbone with the covering of PANI over its surface and



Fig. 11 SEM image of CdS nanopetals (a, b) and nanoflowers (c, d). (e, f) EDX analysis (e) and XRD pattern (f) of CdS nanopetal and nanoflower respectively. (g) UV-visible absorption spectra of CdS nanostructures and (h) Band gap of CdS nanostructure using the Tauc equation. (i) Photocatalytic decomposition of RhB over CdS nanoflower and nanopetal under visible light irradiation. (j) The rate constants determination of CdS nanoflower and nanopetal for RhB degradation.<sup>65</sup>

boundaries. The corresponding TEM images as shown in Fig. 13e and f show similar morphology to SEM images. The photocatalytic performance of the nanostructures was investigated by conducting photodegradation experiments against rhodamine B (RhB) as the model pollutant under visible light

irradiation. After the completion of each photodegradation cycle, the concentration of the degraded dye is measured by recording the absorbance spectrum of the collected dye solution. Fig. 13g and h show the absorbance spectra of RhB solution over CdS and PANI/CdS nanocomposite, respectively after

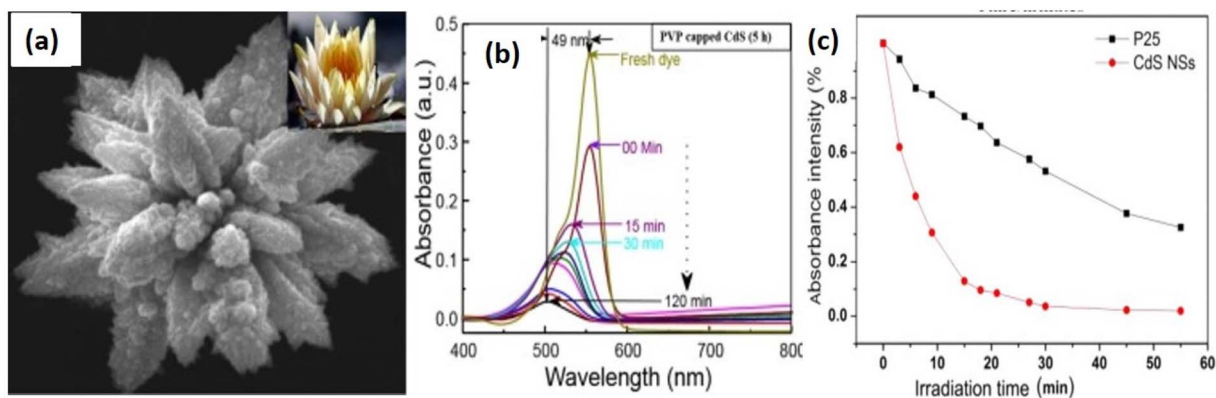


Fig. 12 (a and b) PVP-capped CdS flowers and degradation of RhB dye (95% for 120 min) by irradiation of visible light. Reprinted with permission from ref. 95. (c) Photocatalytic degradation of RhB in the presence of the CdS nanoflowers and P25. Reprinted with permission from ref. 23.

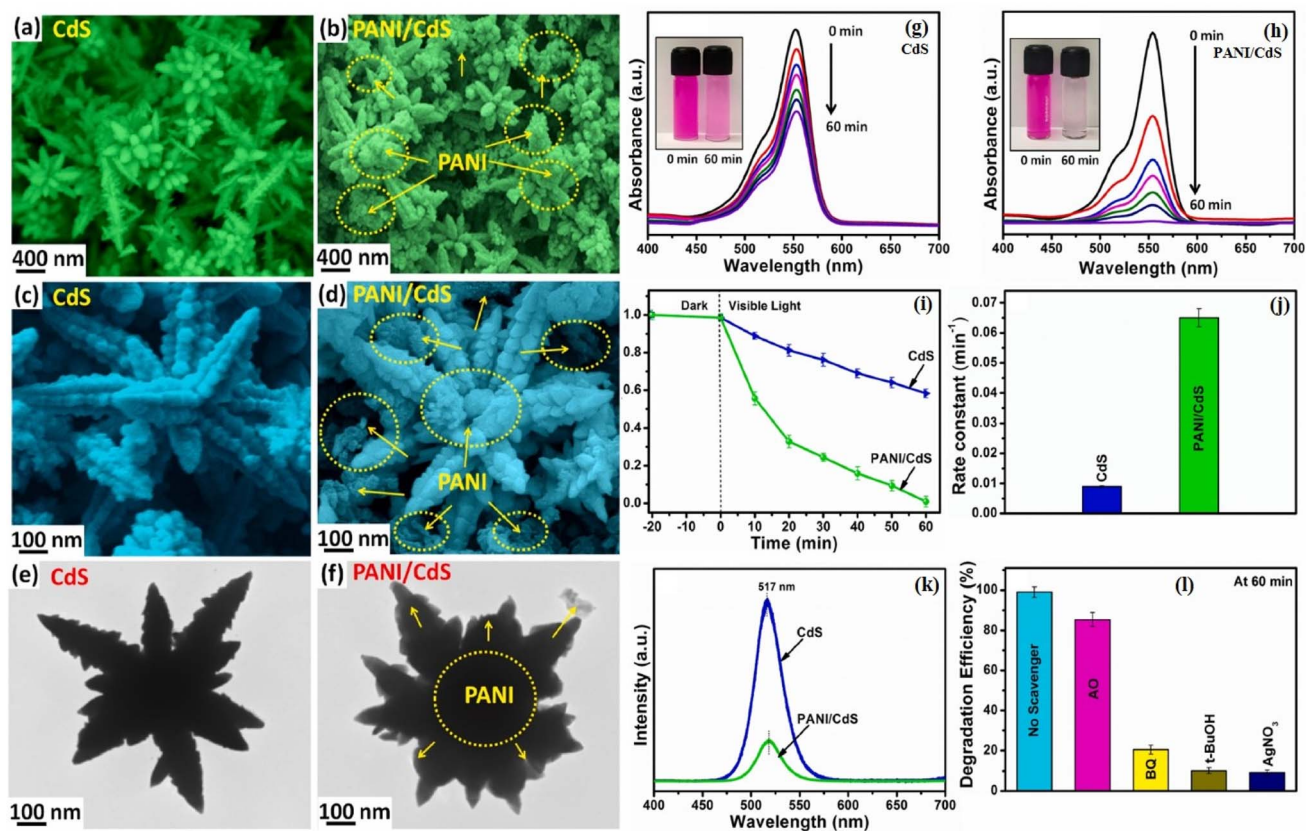


Fig. 13 SEM images of (a, c) CdS NFs and (b, d) PANI/CdS nanostructured samples, TEM images of (e) CdS NFs and (f) PANI/CdS nanostructured samples. UV-vis absorption spectral changes of aqueous RhB solution over (g) pristine CdS NFs and (h) PANI/CdS nanocomposite under equal time intervals of visible light irradiation with inset depicting RhB decoloration after 60 min of light exposure. A gradual decrease in the intensity of the absorption maxima with an increase in the time intervals of visible light illumination was observed suggesting the degradation of RhB over photocatalyst samples. However, the rate of decrement in the RhB absorption peak intensity over PANI/CdS was found to be higher as compared to the pristine CdS nanostructures. Fig. 13i illustrates a comparison of the relative concentration of RhB over CdS and PANI/CdS nanocomposite with time before and after visible

regular intervals of visible light illumination with the inset showing the RhB decoloration after 60 min of light exposure. A gradual decrease in the intensity of the absorption maxima with an increase in the time intervals of visible light illumination was observed suggesting the degradation of RhB over photocatalyst

samples. However, the rate of decrement in the RhB absorption peak intensity over PANI/CdS was found to be higher as compared to the pristine CdS nanostructures. Fig. 13i illustrates a comparison of the relative concentration of RhB over CdS and PANI/CdS nanocomposite with time before and after visible

light irradiation. A slight decrease in the concentration of RhB in the presence of both CdS and PANI/CdS samples in the dark for 20 min was observed indicating negligible adsorption of RhB on these nanostructures after attaining the adsorption-desorption equilibrium. The CdS/polymer nanocomposites showed a better photodegradation rate (Fig. 13j) as compared to only CdS nanostructures ( $\sim 8$  times higher) attributed to the occurrence of the faster rate of photocatalytic reactions at the surface and interfaces of the PANI/CdS photocatalysts. The PL spectra of the CdS and CdS/polymer nanocomposites as shown in Fig. 13k exhibited decreased PL intensity for the nanocomposite attributed to the interfacial contacts between CdS and PANI which facilitated the faster separation of the photo-induced charge carriers. It demonstrates the importance of polymer, *i.e.* PANI, that plays a significant role in separation and transportation of the photogenerated charge carriers enhancing the photocatalytic efficiency of the nanocomposites. Furthermore, the photocatalytic kinetic mechanism was also investigated by performing trapping photocatalytic activity using various scavengers such as benzoquinone (BQ), ammonium oxalate (AO), silver nitrate ( $\text{AgNO}_3$ ), and *tert*-butyl alcohol (*t*-

BuOH). Through this experiment, the photodegradation efficiency of PANI/CdS was studied as shown in Fig. 13l and it was concluded that holes were not the main active species responsible for dye RhB degradation.<sup>146</sup>

Zhang *et al.*<sup>143</sup> studied the CdS and graphene-based nanocomposite as visible-light-driven photocatalysts for selective oxidation of alcohols to corresponding aldehydes. It was found that the CdS NPs uniformly overspread on the graphene scaffold resulting in tunable characteristics, such as morphology and pore structure, and optical and electronic nature were found to be tailored and dependent on the amount of graphene. The resulting high photoactivity of CdS and graphene-based nanocomposite was attributed to enhanced light absorption intensity, high electron conductivity of graphene, and its significant influence on the morphology and structure of the nanocomposites. 3D CdS and graphene nanocomposite-based aerogels with superior adsorption capacity and photocatalytic activity were investigated by Wei *et al.*<sup>147</sup> for water purification. It has been demonstrated in the literature that graphene nanostructures participate as a charge carrier transporter in the photocatalysis process in combination with

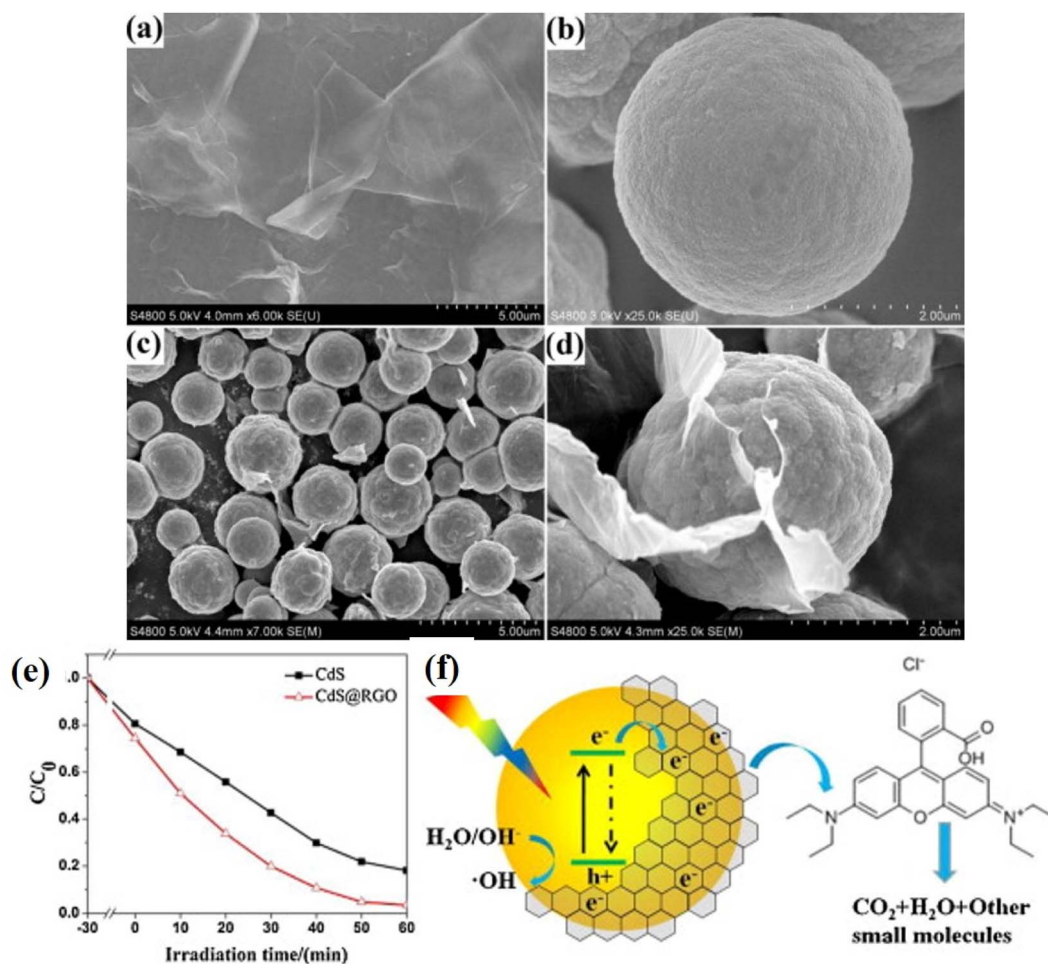


Fig. 14 FESEM images of (a) GO, (b) CdS and (c) CdS@RGO microspheres (in low magnification) and (d), CdS@RGO microspheres (in high magnification), (e) the degradation rate of RhB, ( $C/C_0$ ) as the function of irradiation time. (f) Schematic diagram of the charge transfer between RGO and CdS with photodegradation of RhB molecules under visible light irradiation. Reprinted with permission from ref. 148.

semiconductors inhibiting the rapid recombination of photoexcited electrons and holes resulting in the improved photocatalytic efficiency of semiconductor catalysts.<sup>147</sup> The CdS and graphene-based 3D hybrid hierarchical aerogels showed enhanced adsorption capacity and photocatalytic activity for several organic and pharmaceutical compounds under visible light conditions due to the strong electronic interaction of the counterparts.

Similarly, CdS microspheres and reduced graphene oxide (rGO) based core-shell structures synthesized *via* a two-step hydrothermal method have been reported with enhanced photocatalytic activity.<sup>148</sup> The core-shell structure was characterized by FESEM, Raman, XRD analyses. It was found that such core-shell nanocomposites structures with uniform size and morphology (as shown in Fig. 14a–d) exhibited multifunctional characteristics due to the presence of graphene such as enhanced photocatalytic activity, the effective protection of the internal CdS, enhanced absorption capability of dye molecules and facilitated the separation of photogenerated charges (as shown in Fig. 14e and f). Furthermore, the core-shell structure exhibited recyclable properties as compared to the pure CdS microsphere. Similarly, several 3D nanoarchitectures based on CdS and carbon quantum dots (CQDs) have been shown to exhibit superior photocatalytic activities in the field of water purification degrading harmful and toxic organic pollutants as well as in the energy field.<sup>149,150</sup>

The combination of 3D CdS nanoflowers with graphene and polymer-forming multicomponent nanocomposites has not been investigated so extensively. Ahmad *et al.*<sup>5</sup> explored the 3D CdS-based rGO and polymer *i.e.* polypyrrole (Ppy) nanocomposite visible light photocatalysts for the degradation of organic pollutants such as RhB, reactive blue-171 and toluene under the influence of visible light irradiation. Since Ppy is known to be a visible-light active conducting polymer catalyst, it provided a synergic effect with rGO and 3D CdS nanostructures in enhancing the photocatalytic activity of the nanocomposite. The excellent photocatalytic degradation of dyes was attributed to the formation of more interfacial reaction sites between Ppy and 3D CdS nanoflower structures. Furthermore, the introduction of rGO in the CdS/Ppy matrix enhanced the surface area and provided more reactive sites resulting in excellent nanocomposite photocatalysts for adsorption as well as photodegradation. Fig. 15a and b show the SEM images of 3D CdS nanostructures and their nanocomposites with Ppy as shown in Fig. 15c and d, indicating the uniform distribution of CdS nanoflowers covered on the Ppy sheet. Fig. 15e and f show the SEM micrographs of the nanocomposites *i.e.* Ppy/CdS/rGO exhibiting the scattered CdS NPs and Ppy matrix on the entire sheet of rGO. Fig. 15g and h show the photodegradation activities and kinetics of CdS, Ppy and Ppy/CdS/rGO nanocomposites by monitoring the degradation of RhB in visible light irradiation measuring the absorbance of the degraded aliquots using

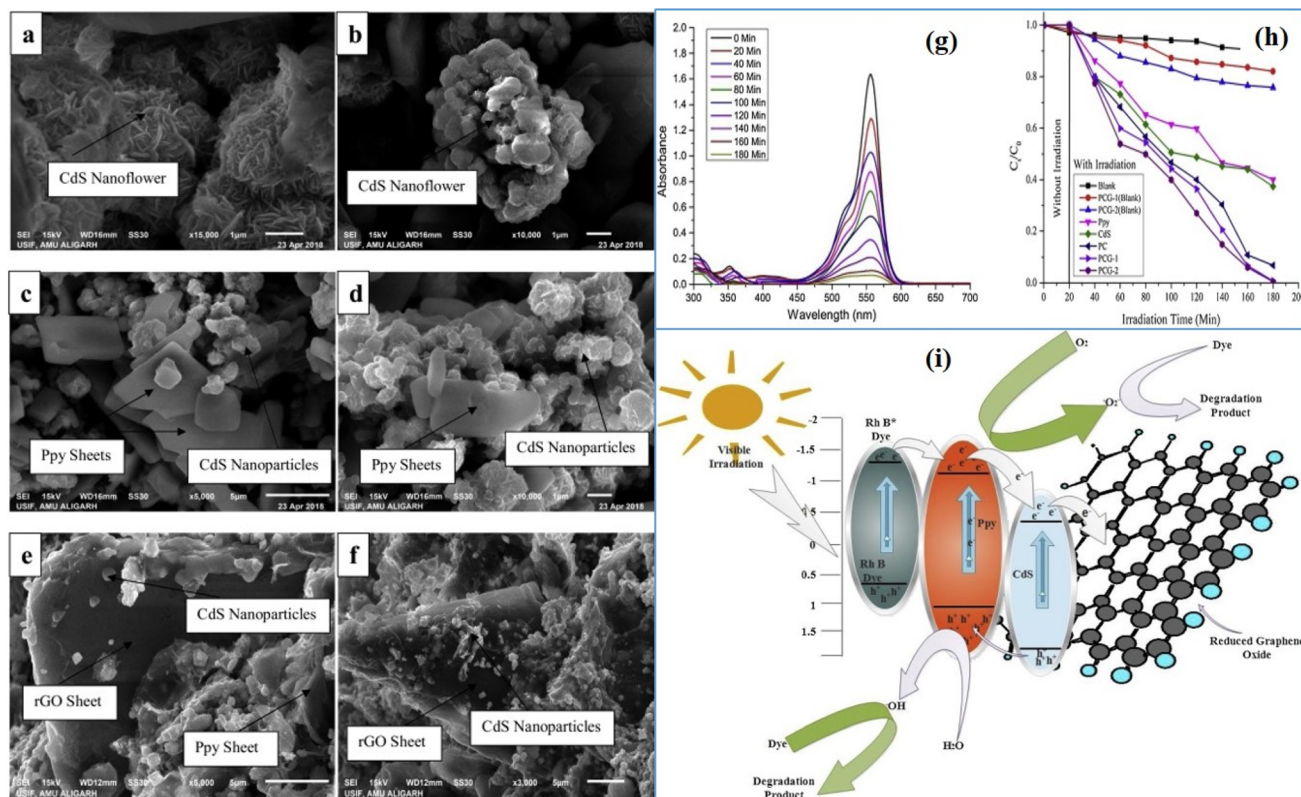


Fig. 15 SEM images of the CdS Nanoflower (a, b), Ppy/CdS (c, d) and Ppy/CdS/rGO (e, f). (g) UV-vis spectra of the degraded sample and (h) kinetics of photodegradation of the various photocatalyst, (here PC is Ppy/CdS, PCG-1, and PCG-2 are Ppy/CdS nanocomposites with 10 and 20% rGO respectively). (i) Proposed mechanism of the photodegradation of the RhB dye. Reprinted with permission from ref. 5.

UV-vis spectroscopy. It was found that after the addition of rGO to the Ppy/CdS nanocomposite, enhanced photocatalytic degradation with more than 99% degradation of RhB dyes in an aqueous solution was achieved in about 180 min. The enhanced photodegradation was explained on the basis of excellent transport properties of rGO sheets that provided the best pathway for the electron transfer useful in ROS generation and further photodegradation. The rGO sheets not only increased the surface area of the nanocomposite photocatalyst but also provided a less hindered path which improved the adsorption of the dye through the  $\pi$ - $\pi$  stacking between dye and rGO as shown in Fig. 15i. Similarly, various CdS nanostructures have been employed with many other graphene-like 2D nano-materials such as MoS<sub>2</sub>,<sup>151,152</sup> metal carbides,<sup>153</sup> *etc.* exhibiting greater photocatalytic activity as compared to the alone CdS nanostructures due to their synergistic effect.

Polydopamine (PDA) functionalized CdS nanostructures have also been studied owing to its unique advantages in surface modification resulting in enhanced photocatalytic properties.<sup>154</sup> Yang *et al.*<sup>155</sup> reported on fabrication of high performance g-C<sub>3</sub>N<sub>4</sub>/PDA/CdS nanophotocatalyst and its visible light activity towards degradation of organic pollutants. It exhibited 97% photodegradation of RhB dye molecules in 80 min under visible light irradiation attributed to the strong visible-light absorption and interfacial charge transfer facilitated by the PDA layer. A core/shell nanostructure composed of CdS/PDA/TiO<sub>2</sub> was produced by nanocoating of PDA plus TiO<sub>2</sub> on CdS nanospheres resulting in 3D nanosphere morphology.<sup>156</sup> The remarkably enhanced photocatalytic performance was observed attributed to enhanced light absorption and charge carrier separation efficiency due to the PDA layer on the surface of the CdS nanospheres. PDA is a kind of emerging biopolymer

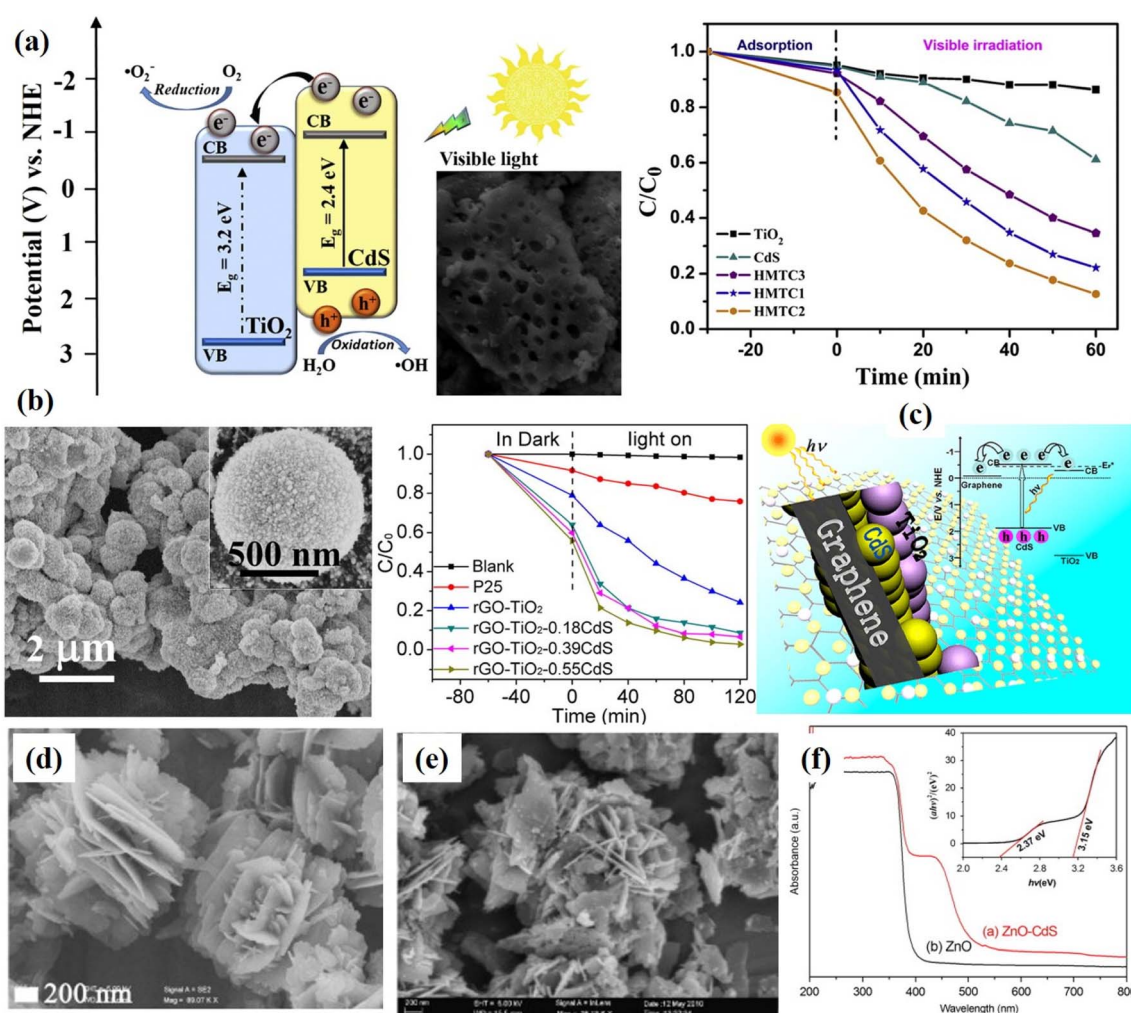


Fig. 16 (a) Hierarchically meso- and macroporous TiO<sub>2</sub>/CdS *i.e.* HMTc heterostructure materials and its visible light photocatalytic activity for the degradation of RhB. HMTc1, HMTc2, HMTc3 show different concentrations of CdS and HMTc2 is the optimized concentration. Reprinted with permission from ref. 157 (b) rGO/TiO<sub>2</sub>/CdS nanocomposites and degradation efficiency of towards MB aqueous solution, reprinted with permission from ref. 26 (c) a possible reaction mechanism of charge transfer in CdS/graphene/TiO<sub>2</sub> hybrid nanocomposites for excellent photocatalytic activity. Reprinted with permission from ref. 160 (d–f) FESEM micrographs of ZnO and ZnO/CdS hybrid nanostructures and UV-visible absorption spectra respectively. Reprinted with permission from ref. 161.

material and very effective in surface modification which can find better applications in the field of photocatalysts.

**3.1.3. CdS/metal oxide-based 3D nano-architectures.** As discussed above, CdS is a visible light active semiconductor photocatalyst having a band gap of approximately 2.42 eV. Therefore, it produced photogenerated electrons and holes under the influence of by solar light spectrum. These CdS nanostructures have also been found to enhance the photocatalytic efficiency of metal oxide semiconductors such as TiO<sub>2</sub> and ZnO by enhancing the photogenerated charge separation and by extending their photocatalytic performance towards the visible light range.<sup>157–159</sup>

Zhao *et al.*<sup>157</sup> demonstrated the role of CdS NPs in enhancing the photocatalytic activity of hierarchically meso- and macroporous TiO<sub>2</sub> photocatalysts forming hierarchically meso- and macroporous TiO<sub>2</sub>/CdS (HMTC) heterostructure materials. It was found that the textural mesopores/interconnected pore framework of TiO<sub>2</sub> photocatalysts enabled a better opportunity to absorb maximum light radiation and heterojunction formation with CdS NPs provided visible light photocatalytic activity as well as better charge separation efficiency resulting in excellent photodegradation efficiency of RhB dye molecules (Fig. 16a). Similarly, Li *et al.*<sup>158</sup> demonstrated the formation hierarchical TiO<sub>2</sub> pinecone-like structure decorated with CdS NPs forming a heterojunction and that could be rationally tailored by optimizing the annealing temperature, which significantly enhanced photocatalytic activity. It was found that the heterojunction nanocomposite optimized at 500 °C annealing temperature exhibited excellent photodegradation activity of MO (85% degradation in 180 minutes) under sunlight irradiation attributed to the synergic effects of the CdS, special surface structure, excellent crystallinity, higher electrical conductivity, and band structure matching. Tian *et al.*<sup>26</sup> demonstrated that ternary rGO/TiO<sub>2</sub>/CdS nanocomposites consisting of TiO<sub>2</sub> spheres (~1 μm), rGO framework uniformly decorated with CdS NPs (~30 nm) exhibited photodegradation of MB (more than 90%) and parachlorophenol (4-CP) (more than 60%) in 60 minutes under visible-light irradiation. The photodegradation activities were higher as compared to the TiO<sub>2</sub>/rGO nanocomposites which showed that the photocatalytic activity was improved due to the presence of CdS NPs (Fig. 16b). Similarly, Zhang *et al.*<sup>160</sup> proposed the ternary CdS/graphene/TiO<sub>2</sub> hybrid nanocomposites which exhibited enhanced photocatalytic activity as compared to the CdS/graphene nanocomposite attributed to the combined interaction of the longer lifetime of photogenerated electron-hole pairs, faster interfacial charge transfer rate, and larger surface area. They proposed the interfacial charge transfer as shown in Fig. 16c.

ZnO, another most extensively used photocatalyst with a bandgap of 3.37 eV, is known for its high photosensitivity and stability, however, the photocatalytic efficiency is not promising as it is UV light activated photocatalysts and also because of the fast recombination of the photogenerated electron-hole pairs. It has been reported that the energy band structures of CdS and ZnO are adequate for promoting the charge transfer process where photogenerated electrons can flow from CdS to ZnO.<sup>161,162</sup>

Xu *et al.*<sup>162</sup> synthesized hierarchical ZnO composed of ultrathin nanosheets decorated with CdS NPs (50–100 nm). These hybrid 3D ZnO/CdS nanostructures exhibited better photodegradation efficiency as compared to pure ZnO nanostructures under natural sunlight. CdS NPs were found to serve as photosensitizers extending the absorption spectrum in the visible region. Similarly, Li *et al.*<sup>161</sup> fabricated ZnO/CdS nano-heterostructure with flower-like morphology and enhanced visible light activity as well as photocatalytic properties as shown in Fig. 16d–f. Self-assembled flower-like CdS–ZnO nanocomposite with excellent charge transfer characteristics was fabricated by Jana *et al.*<sup>163</sup> Firstly, CdS NPs were synthesized followed by the formation of petal-like ZnO structures producing a flower-like nanostructure as shown in Fig. 17a. It was found that due to the formation of such hybrid flower-like structures, there was an excellent coupling of the two semiconductors resulting in the greater charge separation capability leading to better photocatalytic activity. Similarly, highly stable and surface-decorated Zn<sub>0.15</sub>Cd<sub>0.85</sub>S nanoflowers with TiO<sub>2</sub> were demonstrated to be highly effective visible light active photocatalysts towards the degradation of RhB.<sup>164</sup> Fig. 17b–f shows the SEM images of CdS, Zn<sub>0.15</sub>Cd<sub>0.85</sub>S and TiO<sub>2</sub>/Zn<sub>0.15</sub>Cd<sub>0.85</sub>S nanoflowers nanocomposites. It was found that TiO<sub>2</sub>/Zn<sub>0.15</sub>Cd<sub>0.85</sub>S nanoflowers composite with P25 : Cd ratio of 1 : 5 exhibited better photocatalytic performance towards the photodegradation of RhB under visible light irradiation as shown in Fig. 17g. It was explained based on the formation of heterojunction between TiO<sub>2</sub> and Zn<sub>0.15</sub>Cd<sub>0.85</sub>S nanoflowers leading to the greater separation of the photogenerated charge carriers and charge transport. Similarly, synthesized ZnO hierarchical nanoneedle structures sensitized by CdS NPs deposited on copper fiber (CF) that showed greater photocatalytic activity. The CF played an important role in supporting and transporting the charge carriers of CdS NPs/ZnO hybrid nanoneedles presenting the excellent photocatalytic performance under visible light, enabling the decomposition of organic dyes such as RhB within 60 min, with desirable cycling ability.

Various oxide semiconductor photocatalysts such as BiOBr, Bi<sub>2</sub>WO<sub>6</sub>, La<sub>2</sub>Ti<sub>2</sub>O<sub>7</sub>, and Bi<sub>4</sub>Ti<sub>3</sub>O<sub>12</sub> have been studied coupled with CdS forming 3D heterostructures with excellent photocatalytic activities.<sup>165–169</sup> The CdS/BiOBr 3D hybrid nanocomposite photocatalyst was found to exhibit 97% photodegradation of RhB under visible light irradiation and showed no apparent decrease in activity after five cycles.<sup>165</sup> The Bi<sub>2</sub>WO<sub>6</sub>/CdS hybrid 3D nanocomposite films based photocatalyst showed stable catalytic performance until seven successive runs with 92% of MB degradation<sup>166</sup> whereas, CdS QDs/Bi<sub>2</sub>WO<sub>6</sub> heterojunction exhibited 94.5% photocatalytic efficiency. Recently, Cheng *et al.*<sup>169</sup> developed 3D core-shell heterojunction photocatalysts by coating CdS NPs onto Bi<sub>4</sub>Ti<sub>3</sub>O<sub>12</sub> hierarchical microspheres and studied their photocatalytic activities towards the removal of organic pollutants and photocatalytically reduction of Cr(vi) ions.

**3.1.4. CdS/noble metal-based 3D nano-architectures.** Like other CdS-based hybrid nanostructures, CdS/noble metal-based hybrid nanostructures have also been studied as an important class of hybrid nanostructures owing to the plasmonic



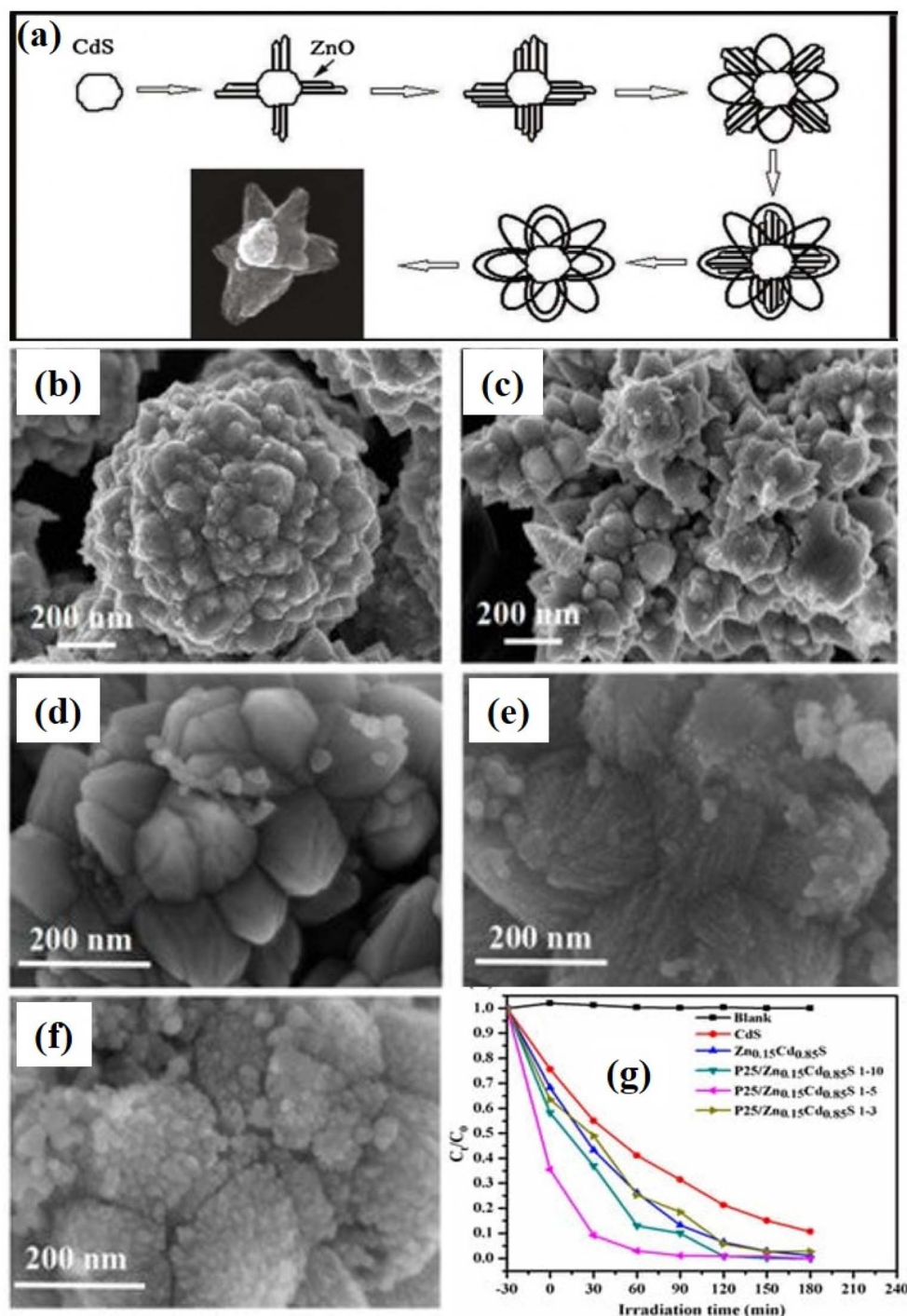


Fig. 17 (a) Schematic of the growth mechanism of flowerlike CdS–ZnO nanostructures.<sup>163</sup> SEM images of (b) pure CdS NPs, (c) Zn<sub>0.15</sub>Cd<sub>0.85</sub>S nanoflowers and (d) TiO<sub>2</sub>/Zn<sub>0.15</sub>Cd<sub>0.85</sub>S nanocomposite with P25: Cd of 1:10, (e) 1:5 and (f) 1:3. (g) Photo-degradation of RhB using TiO<sub>2</sub>/Zn<sub>0.15</sub>Cd<sub>0.85</sub>S nanocomposite with P25: Cd of 1:5.<sup>164</sup>

properties of the noble metal nanostructures and induced photocatalytic activities.<sup>70,170–172</sup> These noble metal-based nanostructures exhibit the better absorbing capability to concentrate light energy at the nanoscale that results from the collective oscillation of surface electrons of the metal with incident light at matching frequencies.<sup>30,70,171,173</sup> These plasmonic nanostructures, when coupled with semiconductors,

enhance the light absorption and furthermore photocatalytic efficiencies of the semiconductors in various fields of applications ranging from the environment to biomedical.<sup>144,174,175</sup> In the case of noble metal and CdS-based hybrid nanocomposite materials, both the CdS and noble metal nanostructures show absorbance in visible light and there may be a possibility of synergetic effect of photoinduced generation of electrons and

holes participating in the reduction and oxidation process to produce ROS. This may enhance the photocatalysis efficiency of the hybrid nanocomposite materials.<sup>70</sup> In this context, very few noble metal/CdS 3D nanostructures have been studied. For example, Kong *et al.*<sup>176</sup> demonstrated the synthesis of 3D Au/CdS heterostructured nanoflowers nanocrystals for the first time through an Au-nanorod-induced hydrothermal method. The Au/CdS nanoflowers were of an average size of about 350 nm containing the Au nanorods of an average diameter, length, and aspect ratio of approximately 50 nm, 100 nm, and 2,

respectively. It was concluded that the Au-nanorods played an important role in the formation of Au/CdS heterostructured nanoflowers.

Interestingly, Wang *et al.*<sup>70</sup> demonstrated the formation of flower-like Au@CdS-CdS NPs with hierarchical heterostructures composed of epitaxially grown 1D CdS nanorods on the surfaces of Au@CdS core-shell NPs as shown in Fig. 18. It was found that these Au and CdS-based 3D hybrid nanoflowers exhibited absorption covering the whole visible region with enhanced photocatalytic activity as compared to only core-shell or CdS

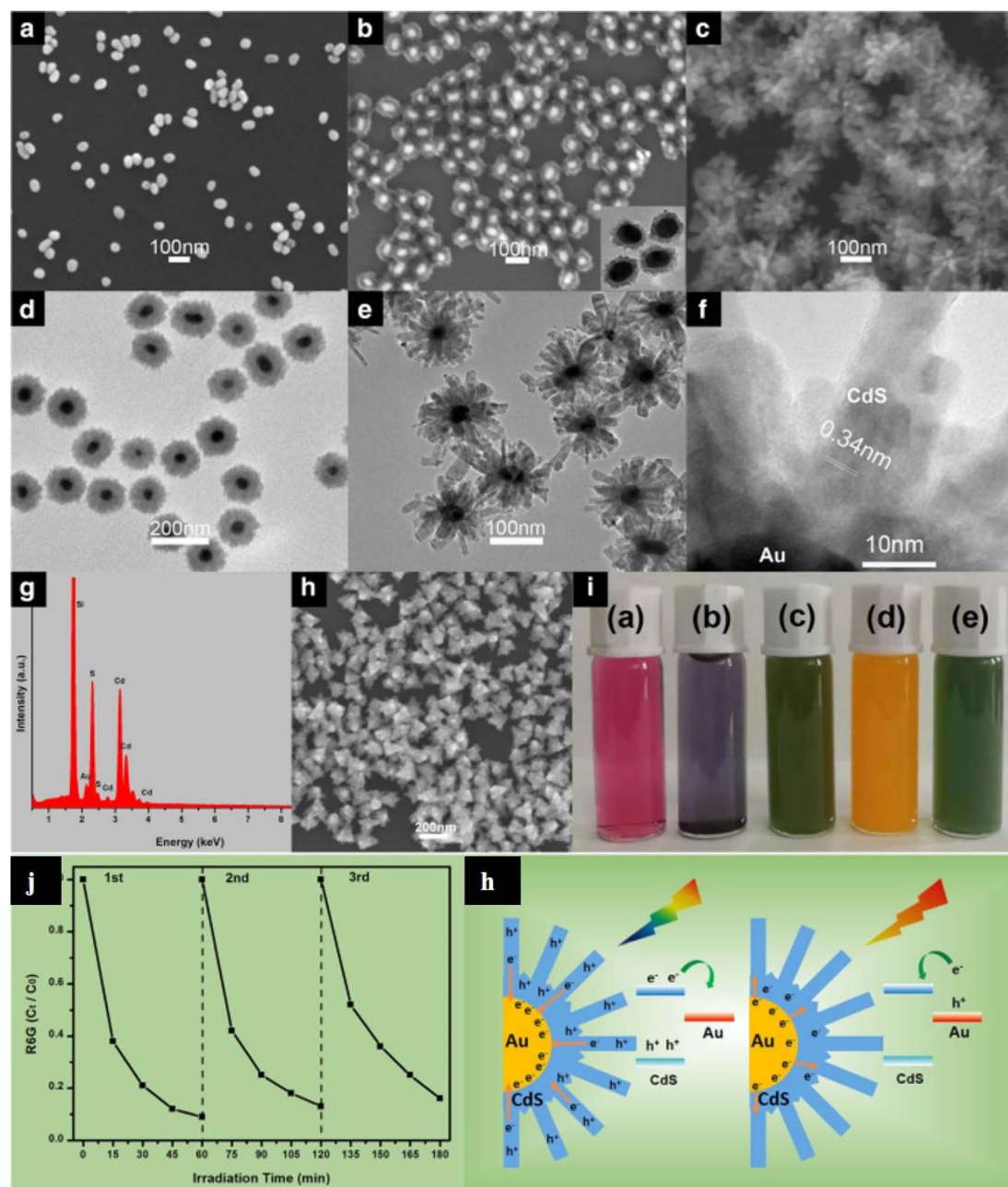


Fig. 18 (a, b and h) SEM images of Au nanoparticles, Au@CdS with a thin shell, and CdS counterparts, respectively. (d) TEM images of Au@CdS with a thick shell. (c, e, f and g) SEM, TEM, HR-TEM image, and EDS profile of Au@CdS-CdS nanoflowers. (i) Photographs of their solution colors. (j) The cycling runs for the photocatalytic degradation of R6G dye over the Au@CdS-CdS nanoflowers under visible light irradiation (400–780 nm). (k) Two charge separation mechanisms for Au@CdS-CdS nanoflowers under 400–780 nm and 600–780 nm irradiation, respectively.<sup>70</sup>

nanostructures. SEM micrographs in Fig. 18a–c show the uniform and well-dispersed Au NPs, Au@CdS core-shell NPs and Au@CdS-CdS NPs respectively. The SEM image of Au@CdS-CdS NPs shows clear flower-like nanostructures. Furthermore, TEM and HR-TEM images (Fig. 18d–f) show clearly the Au@CdS core-shell NPs with a thick CdS shell and nanoflowers structures of Au@CdS-CdS NPs with epitaxially grown 1D CdS nanorods on the surface of Au@CdS core-shell NPs. The diameter and the length of the CdS nanorod were found to be about 16 nm and 40 nm, respectively. The EDS spectrum as shown in Fig. 18g confirms the presence of various elements *i.e.* Au, Cd, S. The CdS nanocrystals are shown in Fig. 18h. In addition, the colors of the solution of Au colloids, Au@CdS core-shell NPs, Au@CdS-CdS nanoflowers NPs, CdS counterparts, are shown in Fig. 18i. These CdS–Au hybrid nanoflowers structures were used for the photocatalytic degradation of R6G dye molecules under visible light which showed excellent photodegradation activity and recyclability as shown in Fig. 18j and corresponding mechanism including two different charge transfer routes has been shown in Fig. 18k. Here, the constituent elements *i.e.* both Au and CdS are visible light active materials and can generate photoinduced charge carriers. As shown in Fig. 18k, there might be two charge separation processes of excitations of individual Au and CdS and transfer of photoexcited electrons from one to another. In case, when CdS would be excited, the photoexcited electrons would jump from the CB of CdS to the Au and in the case when Au would be excited, photoexcited electrons would jump from the surface plasmon state of Au to the CB of CdS. There might be another case when both the elements would be excited, then both the mechanism of photoexcited electrons would be possible. However, it has been reported that the transfer of photoexcited electrons from semiconductor to metal is more probable.<sup>79</sup> Similarly, CdS nanosheets/NPs on Ag nanowires, *i.e.* Ag@CdS core-shell NPs with Ag nanowire structures, were produced by a wet-chemistry approach at low temperatures. These hierarchical nanostructures were found to be excellent photocatalysts as exhibited efficient photocatalytic performance in photodegradation of MO *i.e.* 96% of MO within 240 min due to the broad absorbance from the UV to the near-infrared region leading to the enhance the photocatalytic performance.<sup>177</sup>

In addition to the hybrid 3D photocatalysts of CdS-based nanoflower structures with noble metals, there are several multicomponent plasmonic hybrid CdS nanostructures including other photocatalyst nanomaterials.<sup>178,179</sup> For example, Zhang *et al.*<sup>180</sup> synthesized BiOX(Cl, Br)-Au-CdS photocatalysts exhibiting excellent visible-light-driven photocatalytic activity as compared to BiOX or BiOX(Cl, Br)-Au only toward the degradation of RhB dye molecules. These multi-element photocatalysts with the inclusion of CdS and also with Z-scheme showed improved charge separation efficiency of photo-generated charge carriers. Similarly, Li *et al.*<sup>178</sup> reported on Z-scheme CdS/Au/TiO<sub>2</sub> nanobelt hybrid photocatalyst for eliminating norfloxacin from water. For such architecture, it was concluded that TiO<sub>2</sub> nanostructures provided mainly the absorption/reaction sites, CdS NPs enhanced the overall light harvesting, whereas Au NPs played the role of an electron

transfer mediator. All these contributed to the fast interfacial charge transfer leading to the efficient photoexcited charge carrier separation.

**3.1.5. CdS/other photocatalyst-based hybrid 3D nano-architectures.** There are several semiconductors or photocatalyst nanomaterials other than those mentioned above such as Bi<sub>2</sub>S<sub>3</sub>, CuS,<sup>181,182</sup> SnS<sub>2</sub>, metal-organic frameworks (MOFs), *etc.* which have been used as one of the important components in CdS based hybrid nanocomposites in order to enhance the overall optoelectronic properties leading to the excellent photocatalysts. For example, Deng *et al.*<sup>181</sup> demonstrated the hydrothermal synthesis of CdS/CuS microflower-like structures with tunable morphology and enhanced photocatalytic activities. By varying the composition of the reactants, the morphology of the nanocomposite was tuned from messy to flower-like morphologies with multiple porous densities. The optimized 3D flower structure showed the best photocatalytic activity with a maximum photocatalytic efficiency of 93% for MO dye photodegradation in 150 min under visible light irradiation. It was proposed that the higher photocatalytic activity of such nanoflower structures depended on several factors including the composition, surface area, structure, and morphology, *etc.* Similarly, Wan *et al.*<sup>182</sup> fabricated the first 3D hierarchical lily-like CdS microflowers with several single ultrathin nanosheets as building blocks followed by synthesis of 3D hierarchical CdS/Cu<sub>7</sub>S<sub>4</sub> flower nanostructures by Cu cation exchange (Fig. 19a and b). Through the introduction of Cu ions, the morphology and band gap of the nanocomposites could be tailored for maximum absorption of solar irradiation as shown in Fig. 19c and d. It was noticed that morphology tuning took place from smooth nanosheets to the nanosheets composed of many NPs, further endowing CdS/Cu<sub>7</sub>S<sub>4</sub> quantum dots (QDs) material with the larger specific surface area and more active sites. The hybrid nanomaterials with enhanced optical properties showed better results in dye photodegradation (MB and RB molecules) as compared to only CdS, *i.e.* about ten times higher. Due to the introduction of Cu ions, Fenton like catalysis mechanism in combination of photocatalysis mechanism was proposed as shown in Fig. 19e.

Huang *et al.*<sup>149</sup> fabricated carbon QDs (CQDs) based flower spherical-like CQDs@CdIn<sub>2</sub>S<sub>4</sub>/CdS 3D nanostructures with up-conversion properties by the microwave-assisted method. These 3D hybrid nanostructures with up-conversion properties were able to convert long-wavelength light into short wavelength and showed excellent photodegradation ability where CQDs played an important role of spectral converters, electron transport mediators and acceptors. Shi *et al.*<sup>183</sup> prepared hierarchical Z-scheme Bi<sub>2</sub>S<sub>3</sub>/CdS heterojunctions with dandelion-like structures which showed efficient bacteria-killing activity under visible light irradiation. A hybrid CdS-based flower-like 3D structure with excellent visible light activity composed of hexagonal pencil-shaped nanorod CdS and flower-like morphology SnS<sub>2</sub> was proposed by Huang *et al.*<sup>184</sup> It was found that such nanocomposite exhibited high separation of photoinduced charge carriers along with faster interfacial charge transfer under the influence of sunlight irradiation. These CdS/SnS<sub>2</sub> 3D nanocomposite photocatalysts showed

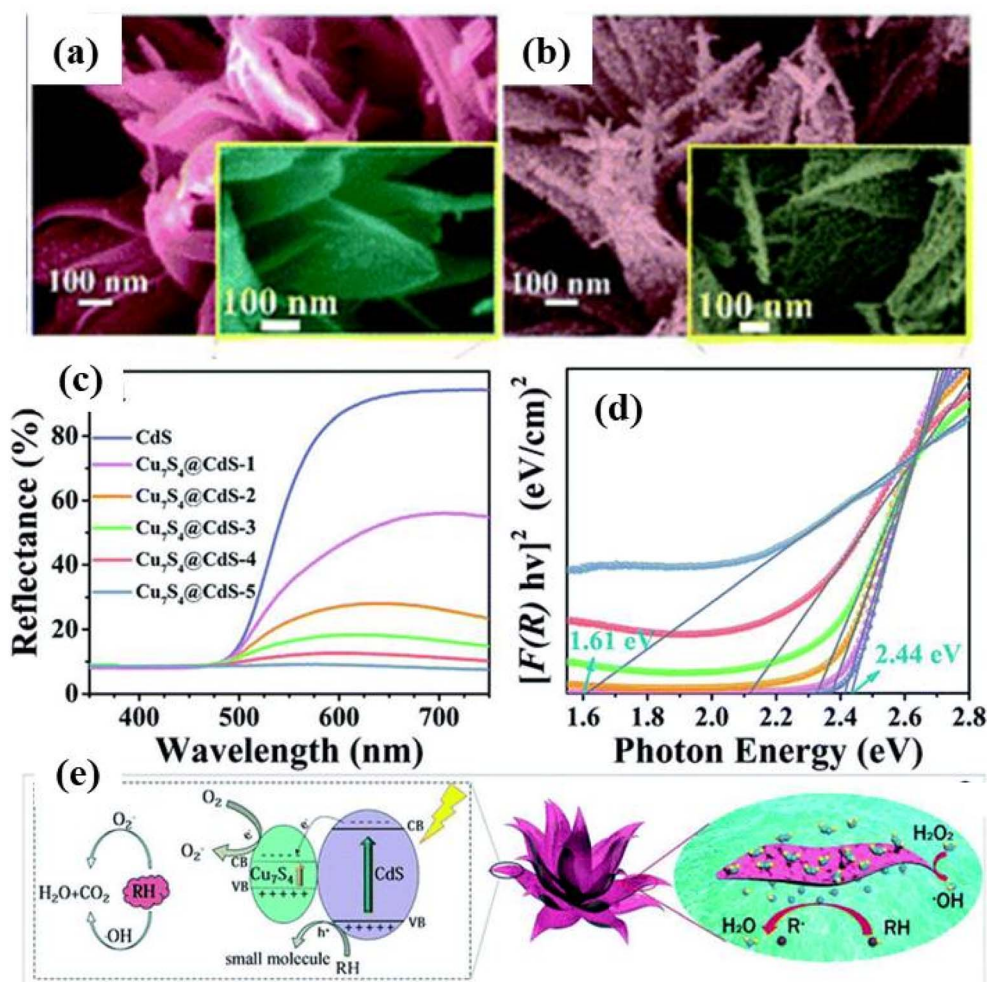


Fig. 19 Low and high-magnification SEM image of (a) CdS, (b) CdS/Cu<sub>7</sub>S<sub>4</sub>. (c) UV-vis diffuse reflectance spectra for the CdS and various compositions of CdS/Cu<sub>7</sub>S<sub>4</sub> nanomaterials, (d) Kubelka–Munk-transformed diffuse reflectance spectra for the CdS and various compositions of CdS/Cu<sub>7</sub>S<sub>4</sub> nanomaterials along with estimated band gap, (e) a schematic of the synergistic catalytic mechanism of CdS/Cu<sub>7</sub>S<sub>4</sub> catalysts.<sup>182</sup>

better photodegradation of MO dye molecules with 85.3% degradation within 120 min with reaction rate constant 9.2 times and 5.32 times higher than that of pure CdS and SnS<sub>2</sub> samples, respectively.

The above discussion on various 3D CdS based nanostructures and their photocatalytic activity towards photodegradation of organic pollutants shows that the morphology plays an important role in degradation efficiency/process. The tailoring of morphology tunes the optical properties of nanostructures and in turn provide tunable characteristics to the materials for enhancing the photodegradation efficiency. Some important CdS based photocatalysts, their optical properties, degradation of various pollutants and photodegradation efficiencies have been summarized in Table 2.

As per the discussion above, it seems that CdS based 3D nanomaterials are very interesting photocatalysts with attractive optoelectronic properties in the field of photocatalytic degradation of organic pollutants. The sole CdS as well as its hybrid composite nano-architectures are very promising with ease of modification and tunability of their morphological, structural

and optical properties. In recent years, these nano-architectures have shown great interest in other fields of photocatalytic applications such as photocatalytic hydrogen production and CO<sub>2</sub> reduction which have been discussed in the next sections.

### 3.2. Photocatalytic H<sub>2</sub> production

Hydrogen, as a clean, efficient, sustainable, and eco-friendly energy source, is considered an important alternative to fossil fuels (such as coal, gasoline, natural gas, *etc.*).<sup>185–188</sup> Water splitting driven by sunlight and photocatalysts, called photocatalysis has been a promising way of achieving solar hydrogen production for decades. Fujishima and Honda, for the first time, discovered the splitting of H<sub>2</sub>O into H<sub>2</sub> and O<sub>2</sub> via ultra-violet light-induced electrocatalysis using TiO<sub>2</sub> as a photoanode in a photoelectrochemical solar cell in 1972.<sup>189</sup> Since then, many types of semiconductor-based photocatalysts have been developed to drive catalytic H<sub>2</sub> evolution under solar irradiation. Such as metal oxides (ZnO, TiO<sub>2</sub>, WO<sub>3</sub>, Cu<sub>2</sub>O, FeO, *etc.*), metal sulfides (CdS, ZnS<sub>2</sub>, MoS<sub>2</sub>, *etc.*), metal nitrides (GaN, InN, *etc.*), organic materials, metal–organic frameworks, metal halide

Table 2 Comparison of photocatalytic degradation activities of the CdS-based catalysts in literature

Catalysts	Optical properties (band gap)	Pollutants	Light source	Photodegradation results/efficiency	Ref.
CdS nanoflower & CdS nanopetals	Band gap $\sim 2.3$ eV for nanoflower and (2.39 eV for nanopetal)	RhB	Simulated sunlight	78% (nanoflowers) and 63% (nanopetal) in 4 h with rate constant $2.6 \times 10^{-3}$ and $4.05 \times 10^{-3} \text{ min}^{-1}$ respectively	65
3D flower-like CdS nanostructures	2.25 eV	MB	Simulated visible light	90.4%	71
CdS nanoflower-based thin films	2.34 to 2.17 eV	MB, MV	40 mW xenon light	96% for MB and 84% for MV in 260 min	140
CdS flower-like morphology composed of word-like nanorods	Red shift in UV visible absorption spectra	RhB	Visible light	95% in 120 min	95
Porous CdS nanoflowers	Absorption in visible range	RhB	Visible light	90% (in 10 min) and complete degradation in 30 min	23
Activated carbon-loaded CdS nanoflower	Varies between 1.85 to 2.51 eV for different compositions	RhB	Visible light	98.12% in 150 min	145
PANI/CdS-composite nanoflowers	2.53 eV	MB	Visible light	Rate constant of PANI/CdS-nanoflower was found to be enhanced by $\sim 1.9$ times over pure CdS-nanoflower	141
3D hierarchical PANI/CdS nanocomposite	2.48 eV	RhB	Visible light, halogen lamp (150 W)	Rate constant of CdS was enhanced by 8 times after coupling with PANI	146
3D hierarchical CdS and graphene nanocomposite	Visible light absorption	RhB, MB, MO	300 W xenon lamp	99.4% (RhB), 88.3% (MB), 73.0% (MO) in 60 minutes	147
CdS@rGO microspheres	Visible light absorption	RhB	500 W xenon lamp	95.2% in 50 min	148
Flower spherical-like composites	Visible light absorption and band gap $< 2.4$ eV	MO	Ultraviolet and simulated visible light	97% in 20 min and better in visible light	149
CQDs@CdIn <sub>2</sub> S <sub>4</sub> /CdS	—				
Z-scheme CdS/CQDs/BiOCl heterojunction	Visible light absorption	RhB and phenol	500 W xenon lamp and 500 W mercury lamp	99.5% within 105 min under UV light irradiation	150
Ppy/CdS-nanoflower/rGO	Visible light absorption	RhB	Visible lamp (power 500 W)	99.1% in 180 min	5
TiO <sub>2</sub> /CdS pinecone-like structure heterojunction	—	MO	Sunlight	85% degradation in 180 minutes	158
rGO/TiO <sub>2</sub> /CdS	(More than 90%) and parachlorophenol (4-CP) (more than 60%) in 60 minutes under	MB, 4-CP	Visible-light	MB more than 90% and (4-CP) more than 60% in 60 minutes	26
Hierarchically meso-macroporous TiO <sub>2</sub> /CdS heterojunction	Visible light absorption	RhB	300 W Xe lamp	87% in 60 min	157
Ternary CdS/graphene/TiO <sub>2</sub> hybrid nanocomposites	Visible light absorption	Alcohols	300 W Xe arc lamp	Enhanced photocatalytic activities as compared to individual catalysts	160
ZnO/CdS nanoflower-heterostructure	2.37 eV	RhB	300 W Xe lamp	100% in 90 min	161
ZnO/CdS nanoflower-P25/Zn <sub>0.15</sub> Cd <sub>0.85</sub> S nanoflower	—	RhB	1000 W halogen lamp	90% in min	163
Flower-like Au@CdS-CdS NPs	2.23 eV	RhB	350 W xenon lamp	100% in 60 min	164
Ag@CdS core-shell NPs	Visible light absorption	R6G	Visible light	86% in 40 min	177
BiOx(Cl,Br)-Au-CdS	UV-visible to NIR absorption	MO	LSC-100 solar simulator	96% in 240 min	180
Z-scheme CdS/Au/TiO <sub>2</sub> nanobelt	Visible light absorption	RhB	300 W xenon lamp	100% in 40 min	178
3D hierarchical CdS/Cu <sub>2</sub> S lily like nanoflower	—	Norfloxacin	35 W xenon lamp	65%	182
CQDs@CdIn <sub>2</sub> S <sub>4</sub> /CdS 3D nanostructures	Visible light absorption	MO	Visible light	98% in 20 min (MB)	149
			Ultraviolet light, visible light and simulated sunlight	97% in 20 min	

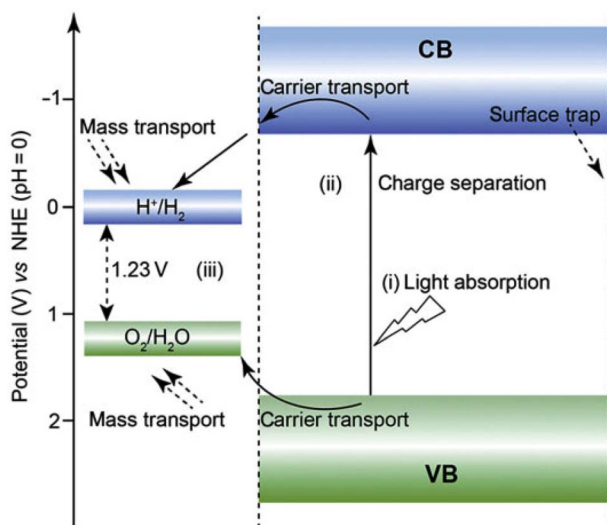
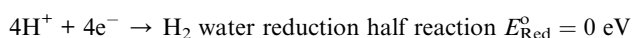
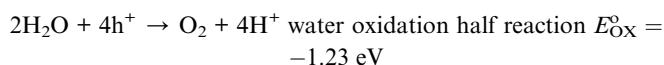


Fig. 20 Schematic illustration of the main processes for photocatalytic water splitting over a semiconductor photocatalyst. Reprinted with permission from ref. 193.

perovskite ( $\text{CsPbBr}_3$ , *etc.*), *etc.*<sup>45,61,190–192</sup> Among them, CdS has drawn much attention from researchers due to its narrow band gap width, effective mass, strong quantum size effect, and promising photocatalytic activity under visible light irradiation<sup>61,192</sup> as also discussed above. In addition, the efficiency of photocatalytic hydrogen production for CdS-based materials can be coordinated by adjusting the morphology, and structure of CdS, as well as the different co-catalysts. The mechanism for photocatalytic  $\text{H}_2$  production using a suitable semiconductor is illustrated in Fig. 20.<sup>193</sup> The photocatalytic hydrogen generation from  $\text{H}_2\text{O}$  includes two half reactions. One is water oxidation, and the other is the water reduction.



In detail, the basic process of a semiconductor photocatalyst for hydrogen evolution from water splitting includes the following steps: first, light energy is converted into chemical energy, and electrons will transfer from the VB to the CB, creating photoproduced electron-hole pairs. Then, the electrons and holes can drive the  $\text{H}_2\text{O}$  to  $\text{H}_2$  and  $\text{O}_2$ , respectively. The minimum energy required to drive the reaction referred to that of two moles of impinging photons is 1.23 eV. It is worth noting that the band gap for CdS is  $\sim 2.4$  eV, and the CB position of CdS is more negative than the redox potential of  $E_{\text{H}_2/\text{H}_2\text{O}}$ , while the VB position is more positive than the redox potential of  $E_{\text{O}_2/\text{H}_2\text{O}}$ .<sup>89,194</sup> In other words, CdS is an appropriate photocatalyst for catalytic hydrogen generation.<sup>188</sup>

As mentioned above, CdS has emerged as one of the most promising photocatalysts for catalytic hydrogen generation under visible light. However, monovalent CdS possess low photocatalytic activity, due to its suffering from several vital disadvantages, such as, low stability in a wide pH range, serious photo-corrosion, fast recombination of photogenerated electron-hole pairs, *etc.* Therefore, in order to enhance the photocatalytic hydrogen generation activity of monovalent CdS, a variety of strategies have been developed. The first one consists of adjusting the morphology, size, crystallinity, *etc.* of CdS. The second way consists of coupling the CdS with other materials (such as carbon materials, noble/non-noble metal-based materials, *etc.*), creating CdS-based heterostructures that can form a Schottky barrier and overcoming the disadvantages of monovalent CdS.

**3.2.1. CdS based sole 3D nano-architectures.** First, the photocatalytic hydrogen generation efficiency of CdS can be adjusted by controlling the size, morphology, and crystallinity of the CdS photocatalysts.<sup>89,195</sup> Pan and co-workers<sup>196</sup> demonstrated that the CdS with nanosphere, nanosheet and nanorod morphological characteristics can be prepared by changing the synthesis conditions (Fig. 21a–c). Compared to CdS-nanosphere and CdS-nanosheet, the CdS-nanorod exhibits the highest photoinduced electrons and holes separation efficiency. Thus, the CdS-nanorod exhibits the best photocatalytic  $\text{H}_2$  production activity with 3.23% solar-to-hydrogen (STH) efficiency (Fig. 21d).<sup>196</sup> Additionally, Vaquero *et al.*<sup>197</sup> reported that CdS crystals with different morphologies (nanorods, sheets, microspheres and irregular particles) can be prepared by changing the solvothermal solvent (ethylenediamine, diethylenetriamine, triethanolamine and ethanol) (Fig. 21e). The hydrogen production rate on CdS samples increased in the order: microspheres < irregular particles < sheets < nanorods (Fig. 21f).<sup>197</sup> The authors further demonstrated that the CdS nanorods exhibit the highest crystallinity and surface area. Therefore, the CdS nanorods show the best photocatalytic  $\text{H}_2$  generation performance. It is demonstrated that the 3D microporous structure of CdS can significantly improve the light absorption and utilization efficiency of CdS. However, rational design and construction of a thin film with a 3D porous structure is still a great challenge. Interestingly, an etched Ti plate supported 3D sponge-like microporous CdS thin-film photocatalyst has been synthesized by Feng *et al.*<sup>136</sup> via the solvothermal method (Fig. 21g). As expected, the 3D microporous CdS film significantly increases the light absorption and utilization of CdS, and the small surface work function allows the photoinduced electrons generated by CdS to quickly escape from the surface of the CdS film. As a result, the photoinduced current density of 3D porous CdS reaches  $4.9 \text{ mA cm}^{-2}$ , and its photoelectric conversion efficiency is up to 47.6% under simulated sunlight illumination (Fig. 21h).<sup>136</sup> In addition, according to Wang *et al.*,<sup>133</sup> CdS with [0001] facets are found to be more reactive as they possess higher surface energy. Through one-pot synthesis, they synthesized different morphologies of CdS nanocrystals by changing the  $\text{Cd}^{2+}$  ions injection rate along [0001] and [101 1] directions, leading to tunable morphologies like nanocones, nanofrustums and nanoplates; among these,

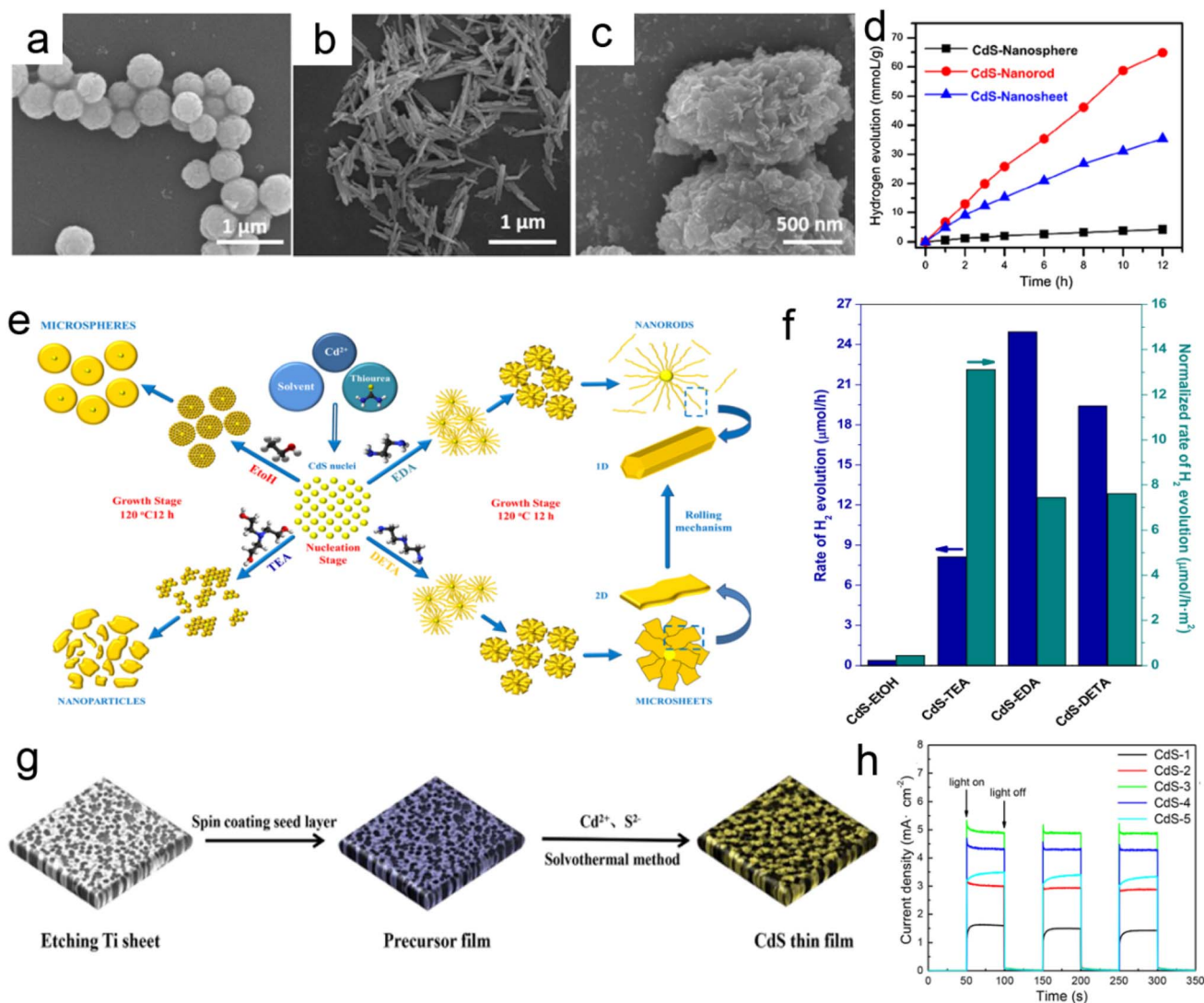


Fig. 21 The SEM images of (a) CdS-nanosphere, (b) CdS-nanorod and (c) CdS nanosheet. (d) Photocatalytic hydrogen evolution rates in 12 h for CdS-based nanosphere, nanorod, and nanosheet. Reprinted with permission from ref. 196. (e) Schematic diagram showing the formation of CdS structures with various morphologies by the solvothermal method using different solvents. (f) Comparison of rate of hydrogen production over CdS photocatalysts with different morphologies. Reprinted with permission from ref. 197. (g) Schematic illustration of the preparation process of the 3D sponge-like microporous CdS thin-film photoelectrode. (h) The photoinduced  $i-t$  curves at 0 V (vs. Ag/AgCl) of the prepared CdS photoelectrodes. Reprinted with permission from ref. 136.

nanoplates are found to be most photocatalytic efficient for photocatalytic hydrogen production.

Up to now, despite changing the morphology, structure, and crystallinity to promote the photocatalytic  $H_2$  generation activity of CdS, further large-scale applications of CdS photocatalysts are still restricted due to their unstable chemical properties and serious photocorrosion under visible light irradiation for a long time. To solve these problems, it can be demonstrated to be useful that combine CdS with other stable materials (such as, noble metal, metal oxides, sulfides, carbon, organic materials, etc.) to fabricate CdS-based nanohybrids.<sup>61</sup>

**3.2.2. CdS/noble metal based 3D nano-architectures.** As mentioned above, the photocatalytic activity of CdS can be modified by the incorporation of some other stable materials. It is reported that noble metals (such as Au, Ag, Pd, Pt, or Rh, etc.)

are widely used as the co-catalyst because noble metals could improve the photogenerated electrons and holes separation and enhance the photo-efficiency of CdS.<sup>198–200</sup> For example, Fang *et al.*<sup>201</sup> adopted the butterfly wings from *Morpho didius* (M) as biotemplates to fabricate 3D hierarchical CdS/Au wing scales for photocatalytic hydrogen generation (Fig. 22a–c). Owing to the effective potentiation effect of localized surface plasmon resonance (LSPR) generated by multilayer metallic rib structures and a good interface bonding state between CdS and Au nanoparticles, the 3D hierarchical CdS/Au structure show an excellent photocatalytic activity with  $221.8 \mu\text{mol h}^{-1}$  hydrogen production rate under visible light (420–780 nm) (Fig. 22d).<sup>201</sup> Moreover, Soto *et al.*<sup>202</sup> proposed a work in which they modified CdS nanorods with Ag metal using a solvothermal process. They further indicated that the following three factors affect the

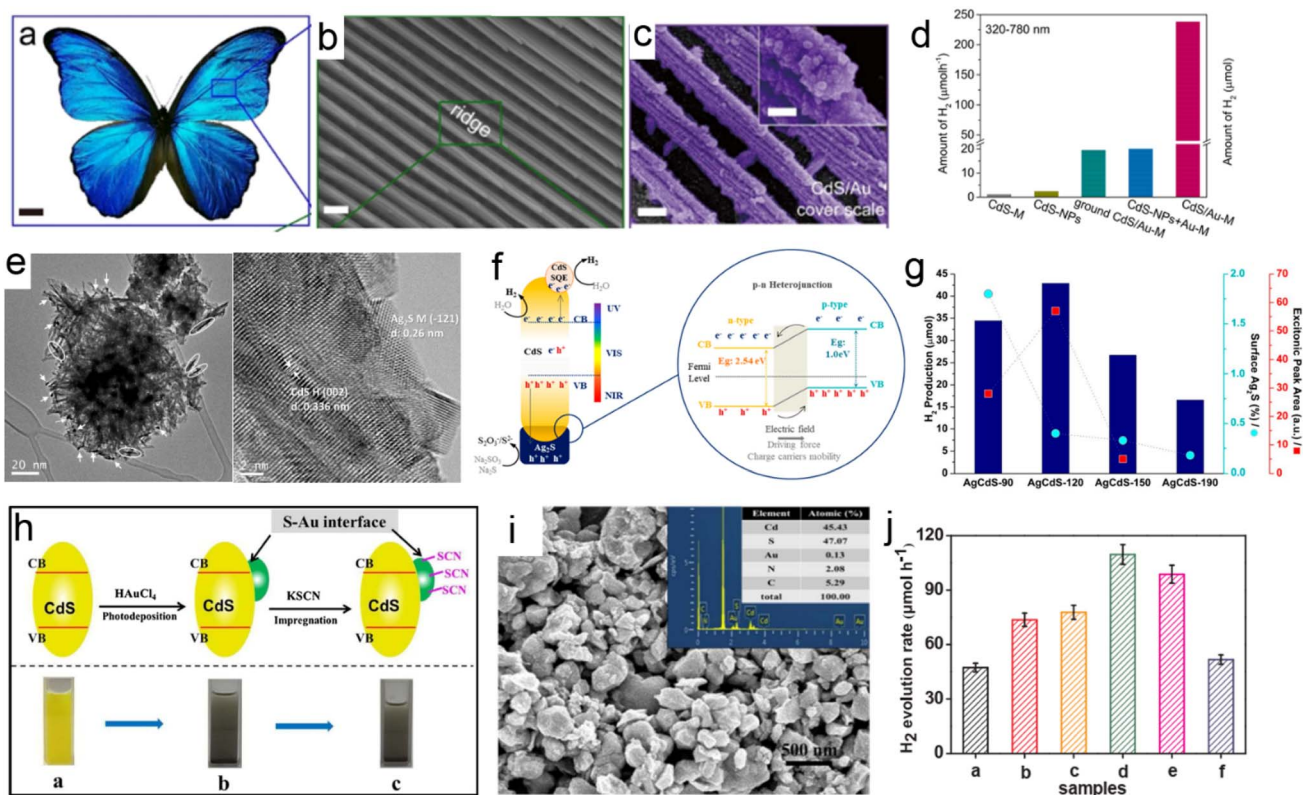


Fig. 22 (a) Optical photograph of *Morpho didius*. SEM images of the (b) wing scales and (c) CdS/Au-M. (d) Photocatalytic activities of different samples for H<sub>2</sub> production under 320–780 nm. Reprinted with permission from ref. 201. (e) TEM and HR-TEM images of AgCdS-120 sample. (f) Schematic diagram showing the combination of factors that operates in the AgCdS-T photocatalysts. (g) Relationship between H<sub>2</sub> evolution for AgCdS-T with respect to the Ag<sub>2</sub>S surface concentration and concentration of quantum dots.<sup>202</sup> (h) Graphical illustration for the synthesis of CdS, CdS/Au, and (c) CdS/Au-SCN. (i) FESEM/EDX of CdS/Au-SCN (0.5 mM). (j) The photocatalytic H<sub>2</sub>-evolution activity performance of different samples. Reprinted with permission from ref. 203.

efficiency of the photocatalytic hydrogen production significantly, such as the crystallinity of the CdS samples, the existence of small CdS nanocrystals and whether presence of Ag<sub>2</sub>S species (The Ag<sup>+</sup> ions in the presence of S<sup>2-</sup> ions formed Ag<sub>2</sub>S (bandgap ≈ 1 eV), which in the presence of CdS behaved like an effective p–n heterojunction, resulting better photoactivity due to their confinement effect). Since the Ag–CdS sample prepared at 120 °C can optimize those factors, the best efficiency for hydrogen production was obtained (Fig. 22e–g).<sup>202</sup>

In addition, it is reported that the H<sub>2</sub>-production rate on the sample surface plays an important role for the noble metal cocatalyst-modified photocatalysts. To confirm this phenomenon, Wang *et al.*<sup>203</sup> demonstrated that the selective modification of SCN<sup>-</sup> on the Au surface can obviously enhance the photocatalytic activity of CdS/Au due to the possible synergistic effect of Au as an electron-transfer mediator and SCN<sup>-</sup> as the interfacial catalytic active-sites (Fig. 22h and i). Specifically, the CdS/Au-SCN exhibited better photocatalytic activity (109.60 μmol h<sup>-1</sup>) than that of CdS/Au (73.70 μmol h<sup>-1</sup>) as shown in Fig. 22j.

**3.2.3. CdS/transition metal based 3D nano-architectures.** Noble metals such as Pt, Ag, Au, *etc.*, can serve as highly efficient cocatalysts to enhance the photocatalytic hydrogen generation performance of CdS.<sup>204</sup> However, the high cost and limited

resources of precious metals limit their widespread application. Therefore, numerous studies have been concentrated on combining the transition metal (including Mo, W, Co, Ti, Zn and Ni, *etc.*)-based oxides/sulfides/selenides with CdS-based 3D nano-architectures to promote the efficiency of photocatalytic hydrogen generation for CdS.<sup>149,205–209</sup> For example, as shown in the SEM and TEM images (Fig. 23a and b), Zhong *et al.*<sup>210</sup> synthesized a novel rods-on-rods heterostructure 3D CdS branched TiO<sub>2</sub> nanoarrays *via* a simple *in situ* growth method. The unique 3D porous rods-on-rods structure not only benefits the visible light scattering and absorption on the surface of the material, but also effectively enhance the photogenerated electrons and holes separation and transportation. As a result, this CdS/TiO<sub>2</sub> 3D nanocomposite exhibits advantageous efficiency and durability in both photoelectrochemical and self-bias photocatalytic hydrogen generation systems with H<sub>2</sub> evolution rate of 51.6 and 11.9 μmol cm<sup>-2</sup> h<sup>-1</sup>, respectively (Fig. 23c).<sup>210</sup>

In addition, Zhang *et al.*<sup>211</sup> reported a novel β-NiS film modified CdS nanoflowers (NiS/CdS NFs) heterostructure by one-pot hydrothermal method. Because the surface of CdS nanoflowers has been covered by the highly conductive β-NiS film, it could benefit the transfer of photogenerated e<sup>-</sup> and facilitate the separation of e<sup>-</sup>–h<sup>+</sup> pairs. As a consequence, the



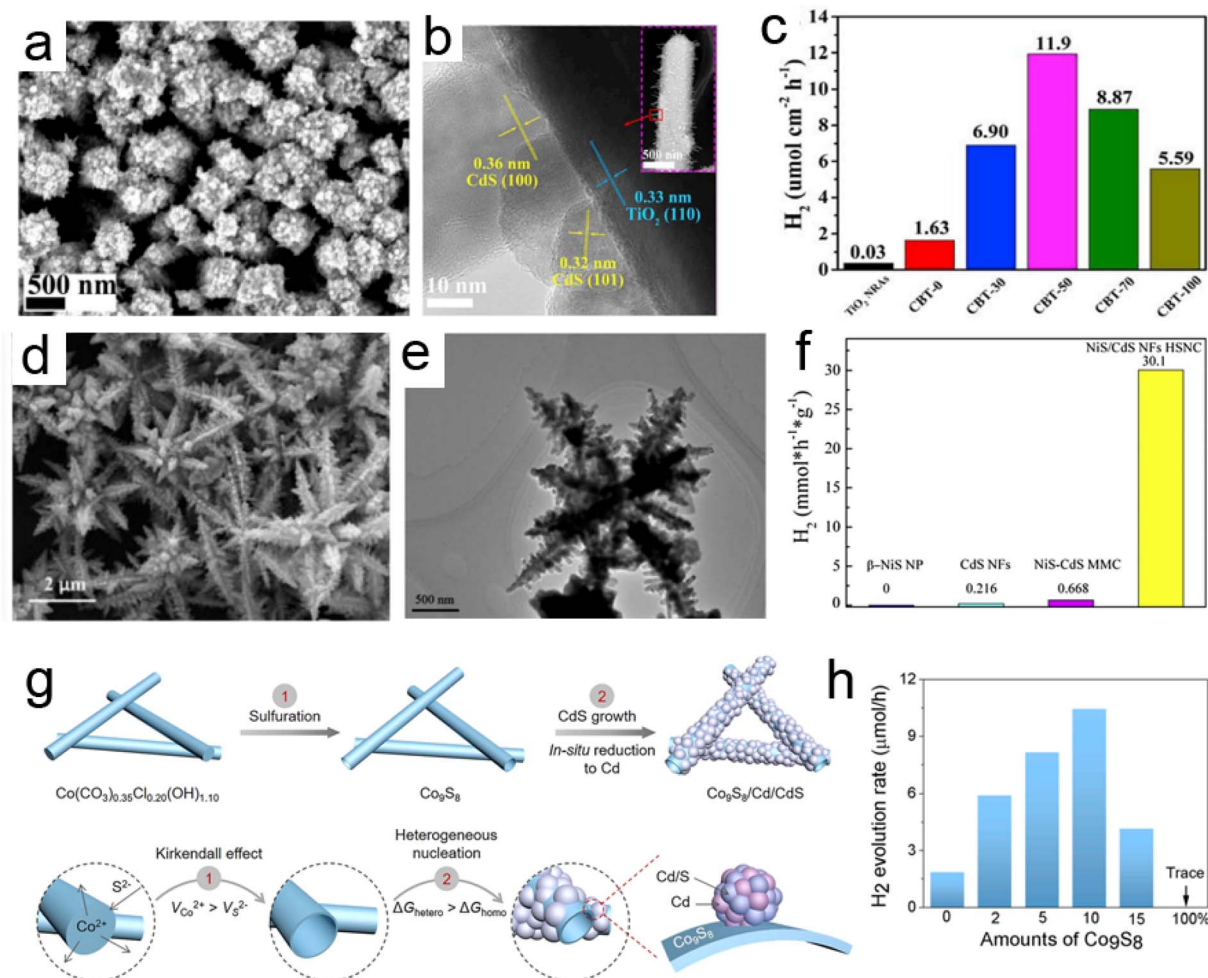


Fig. 23 (a and b) SEM and HRTEM images of the CBT-50. (c) The average rate of photocatalytic H<sub>2</sub> generation over all the CBT-x samples. Reprinted with permission from ref. 210. (d, e) SEM and TEM images of the NiS/CdS NFs HSNC. Reprinted with permission from ref. 211. (g) Schematic diagram illustrating the synthesis process of the Co<sub>9</sub>S<sub>8</sub>@Cd/CdS heterostructure. (h) Photocatalytic H<sub>2</sub> evolution rates over the prepared samples. Reprinted with permission from ref. 212.

NiS/CdS NFs can achieve a recorded value for an H<sub>2</sub> production rate of about 30.1 mmol h<sup>-1</sup> g<sup>-1</sup> (Fig. 23d–f).

In addition to the metal oxides/sulfides/selenides-CdS based binary nanocomposites could be used as a co-catalyst to enhance the photocatalytic H<sub>2</sub> production efficiency for CdS. Recently, some studies have tried to combine CdS with two or more other co-catalysts to form a multicomponent such as CdS/Au/ZnO, Ti<sub>3</sub>CN@TiO<sub>2</sub>/CdS-based photocatalysts, which further showed that the photocatalytic performance of CdS-based multicomponent nanocomposites was obviously enhanced.<sup>213</sup> For example, a hollow Co<sub>9</sub>S<sub>8</sub>/Cd/CdS Z-scheme tubular hybrid heterostructure has been reported by Zhang *et al.*<sup>212</sup> (Fig. 23g). Based on the high-density catalytic sites, good solar light capture by small band gap Co<sub>9</sub>S<sub>8</sub>/CdS, and incorporation of Cd in Co<sub>9</sub>S<sub>8</sub>/CdS could offer a fast charge separation and smooth transfer, the obtained Co<sub>9</sub>S<sub>8</sub>/Cd/CdS nanocomposite shows an H<sub>2</sub> production rate about 10.42 μmol h<sup>-1</sup> without an obvious decrease in activity after several cycles (Fig. 23h).<sup>212</sup>

**3.2.4. CdS/organic materials-based 3D nano-architectures.** Compare with inorganic materials, organic materials are

characterized by flexibility, workability, and controllability, being easy to purify and to be modified with molecules. Based on these typical characteristics of organic materials, the combination of CdS with organic molecules is a possible way to further enhance the photostability and carriers' mobility of CdS. As an example, Lv *et al.*<sup>214</sup> is reported that DETA was successfully used to modify the structure of CdS and enhance the photocatalytic H<sub>2</sub> generation activity of CdS (Fig. 24a and b). They further demonstrated that the organic–inorganic CdS/DETA nanocomposites have several advantages in comparison with single CdS, such as higher surface area, more active sites, and better charge carriers' mobility. Therefore, the CdS/DETA hybrid structure exhibits excellent photocatalytic activity with an H<sub>2</sub>-generation rate of about 8059 μmol g<sup>-1</sup> h<sup>-1</sup> under solar light and satisfactory durability (Fig. 24c).<sup>214</sup> Additionally, CdS combination with conducting organic polymer also has attracted great interest due to its outstanding conductivity and durability, ease of preparation and good environmental compatibility.<sup>215</sup> As illustrated in Fig. 24d, monodisperse polyaniline@CdS (PANI@CdS) core–shell nanospheres were

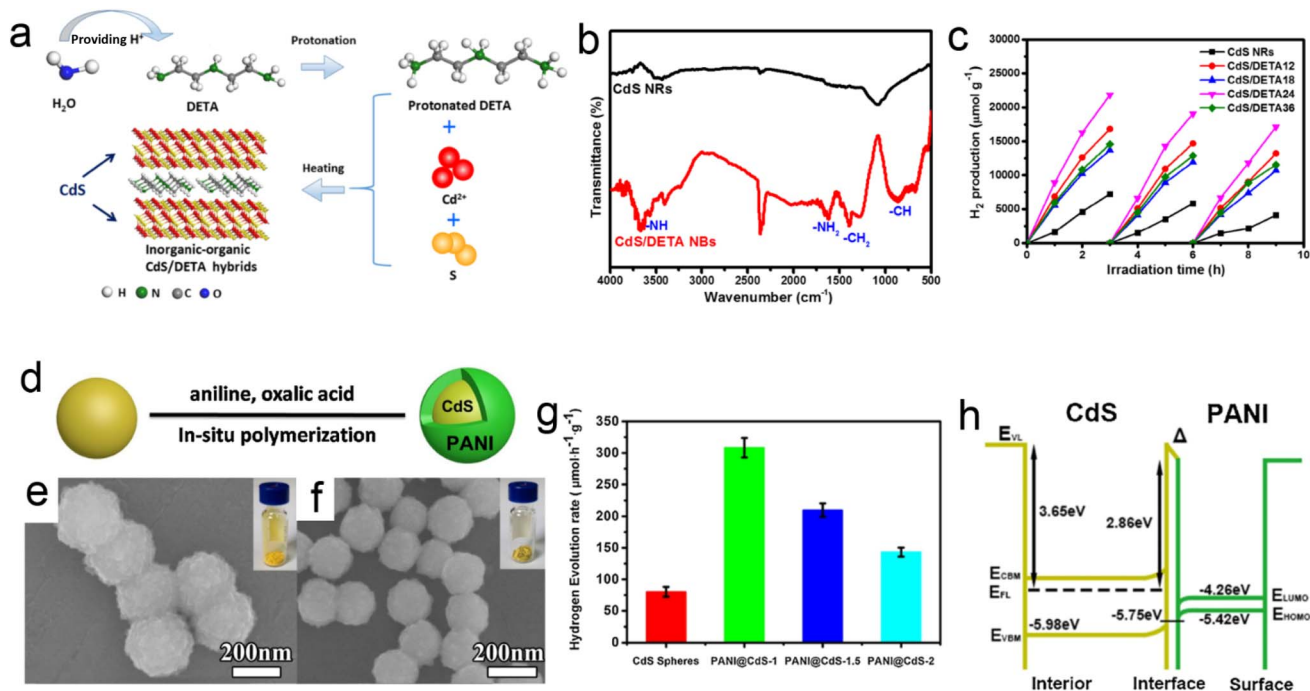


Fig. 24 (a) The synthetic illustration of CdS/DETA hybrids. (b) Fourier-transform infrared spectroscopy (FT-IR) spectra of CdS NRs and CdS/DETA. (c) The cycling test of PHE over CdS and CdS/DETA composites. Reprinted with permission from ref. 214 (d) schematic illustration of PANI shell coating on the CdS nanospheres surface. SEM images of the (e) porous CdS nanospheres and (f) PANI@CdS core-shell nanospheres. (g) The photocatalytic hydrogen production rates of porous CdS nanospheres and PANI@CdS core-shell nanospheres. (h) Schematic energy level diagram of the component materials used in the inverted configuration. Reprinted with permission from ref. 215.

rationally designed and synthesized by Wang *et al.* (Fig. 24e and f).<sup>215</sup> When PANI@CdS core-shell nanospheres were further used as a photocatalyst for H<sub>2</sub> generation, the PANI@CdS heterostructure exhibited better photocorrosion inhibition and photocatalytic H<sub>2</sub> production performance than the pure CdS. In particular, the PANI@CdS hybrid structure with the thinnest PANI shell has the best H<sub>2</sub>-evolution rate of 310 mol h<sup>-1</sup> g<sup>-1</sup> and without degradation after 30 h (Fig. 24g). Moreover, they further suggested that the photogenerated holes migrating from VB of CdS to the highest occupied molecular orbital (HOMO) of PANI lead to improved photocatalytic H<sub>2</sub> evolution (Fig. 24h).<sup>215</sup>

**3.2.5. CdS/carbon based 3D nano-architectures.** Research has shown that carbon-based materials have good mobility of charge carriers and excellent electronic conductivity. Theoretically, carbon-based materials can be served as excellent electron acceptors in photocatalysis. In other words, when using CdS-carbon based nanocomposites as the photocatalysts, the photo-generated electron can be effectively transferred *via* the carbon-based materials. Indeed, Li *et al.*<sup>27</sup> achieved the preparation of graphene-supported CdS by a solvothermal method (Fig. 25a and b), when directly used as a photocatalyst for H<sub>2</sub> production, the optimal CdS/graphene catalyst reach an excellent H<sub>2</sub>-production rate of 1.12 mmol h<sup>-1</sup> under solar-light irradiation and corresponding quantum efficiency of 22.5% at 420 nm (Fig. 25c and d).<sup>27</sup> In contrast, it is suggested that another graphene-like photocatalytic material, g-C<sub>3</sub>N<sub>4</sub>, can be used as an excellent hole-transfer cocatalyst to enhance the rapid transfer of photo-generated holes from the CdS surface (Fig. 25e). Yun *et al.*<sup>216</sup>

reported that the CdS/g-C<sub>3</sub>N<sub>4</sub> heterostructure photocatalyst was prepared by a simple high-temperature self-transformation strategy using melamine and CdS as the precursor (Fig. 25f). The SEM and TEM images shown in Fig. 25g and h revealed that g-C<sub>3</sub>N<sub>4</sub> nanoparticles are uniformly distributed on the CdS surface. The optimal CdS/g-C<sub>3</sub>N<sub>4</sub> nanocomposites exhibited a high H<sub>2</sub> generation rate of about 5303 mol h<sup>-1</sup> g<sup>-1</sup> (Fig. 25i).<sup>216</sup>

As discussed in last Section 3.1, PDA as an emerging polymeric materials has great efficiency to boost the photocatalytic properties of the photocatalysts by providing a thin layer on their surface that facilitates the tunneling of photoelectrons which further improves the wettability of catalysts, and provides a passivating surface.<sup>217,218</sup> Wang *et al.*<sup>218</sup> demonstrated that PDA possessed a good photothermal effect in boosting photocatalytic H<sub>2</sub> production by studying the photocatalytic activity of PDA/CdS nanocomposites under the xenon lamp irradiation. Interestingly, it was observed that PDA layer prevented the CdS nanostructures from photo corrosion and served as a photothermal matrix resulting in increasing the reaction temperature which improved the H<sub>2</sub> production as compared to the production obtained at room temperature. Similarly, Liu *et al.*<sup>219</sup> demonstrated that CdS@PDA@SnO<sub>2</sub> nanostructures exhibited enhanced photocatalytic H<sub>2</sub> production and inhibited photocorrosion of CdS nanostructures.

In recent years, the photocatalytic hydrogen production using CdS-based materials, especially 3D hierarchical nano-architectures, has shown great progress with better production efficiency and seems to be a potential alternative in the

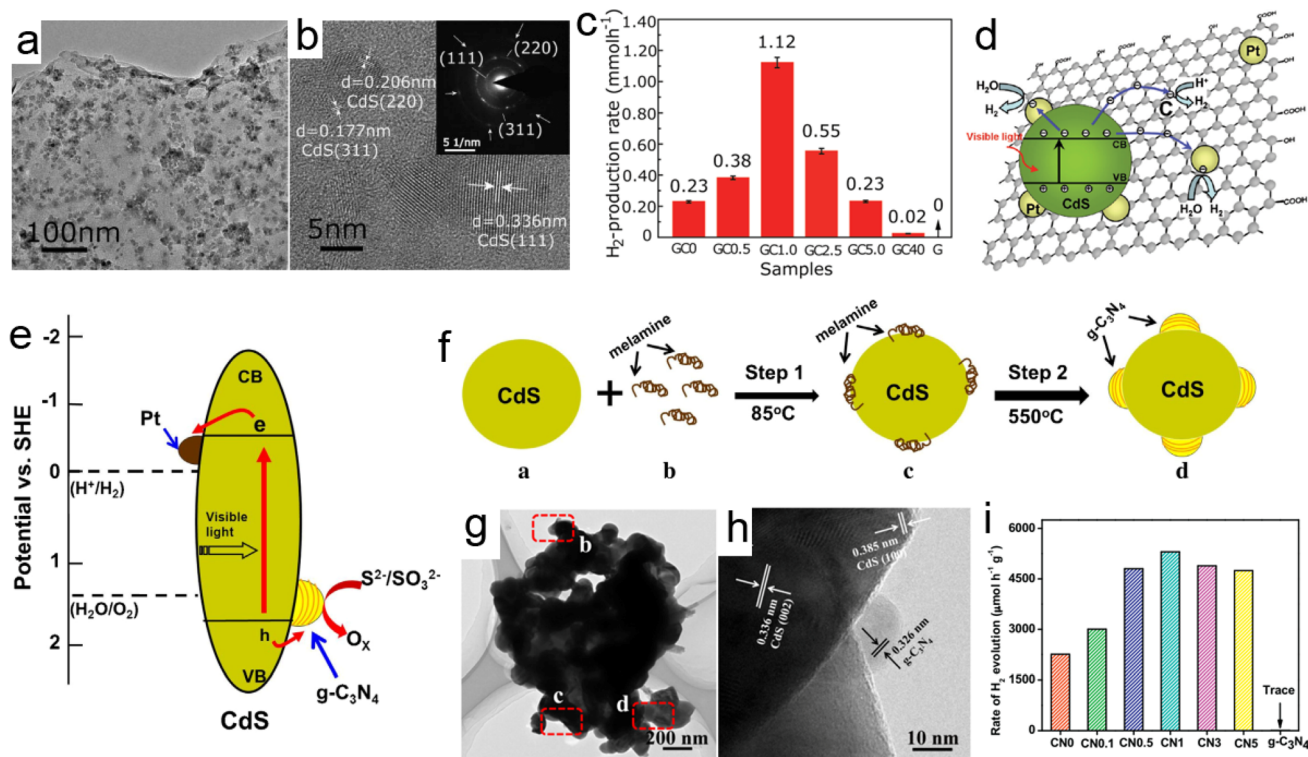


Fig. 25 (a) TEM and (b) HRTEM images of CdS/graphene sample. (c) The photocatalytic activity for  $\text{H}_2$ -production and (d) the schematic illustration for the charge separation and transfer in the CdS/graphene system under visible light. Reprinted with permission from ref. 27. (e) The schematic illustration for the proposed  $\text{g-C}_3\text{N}_4$ -cocatalyst modified CdS heterostructure. (f) Graphical illustration for the synthesis of  $\text{g-C}_3\text{N}_4/\text{CdS}$  composite photocatalysts. (g and h) TEM images of the CdS/ $\text{g-C}_3\text{N}_4$ . (i) The photocatalytic  $\text{H}_2$ -production activities of the CdS/ $\text{g-C}_3\text{N}_4$  samples. Reprinted with permission from ref. 216.

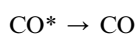
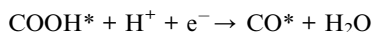
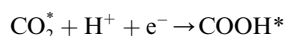
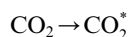
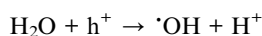
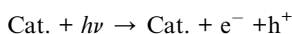
Table 3 Comparison of photocatalytic hydrogen evolution activities of the CdS-based catalysts in literature

Catalyst	Light source	$\text{H}_2$ evolution rates	Solar-to-hydrogen (STH) efficiency/quantum efficiency	Ref.
Hexagonal CdS	300 W Xe lamp	$5.4 \text{ mmol g}^{-1} \text{ h}^{-1}$	3.23%	183
CdS nanorods	Visible light	$24.94 \text{ } \mu\text{mol h}^{-1}$	—	184
CdS branched $\text{TiO}_2$	Simulated sunlight	$11.9 \text{ } \mu\text{mol cm}^{-2} \text{ h}^{-1}$	1.5%	129
CdS nanoplates	300 W Xe lamp	$1.61 \text{ mmol g}_{\text{CdS}}^{-1} \text{ h}^{-1}$	—	126
NiS loaded on CdS nanoplates	300 W Xe lamp	$22.3 \text{ mmol g}_{\text{CdS}}^{-1} \text{ h}^{-1}$	18%	126
RhP/CdS	Visible light ( $\lambda > 420 \text{ nm}$ )	$32.54 \text{ } \mu\text{mol mg}^{-1} \text{ h}^{-1}$	—	185
Ru-CdS-ZnO-CdO	Visible light	$\sim 22.5 \text{ } \mu\text{mol g}^{-1} \text{ h}^{-1}$	—	187
3D CdS/Au	Visible light	$221.8 \text{ } \mu\text{mol h}^{-1}$	—	188
Ag-CdS	Xenon arc lamp (150 W)	$\sim 1.60 \text{ mmol g}_{\text{CdS}}^{-1} \text{ h}^{-1}$	—	189
CdS/Au-SCN	350 W xenon lamp ( $\lambda \geq 420 \text{ nm}$ )	$109.60 \text{ } \mu\text{mol h}^{-1}$	$\sim 11.25\%$	190
CQDs@CdIn <sub>2</sub> S <sub>4</sub> /CdS	UV-vis	$397.2 \text{ } \mu\text{mol g}^{-1} \text{ h}^{-1}$	—	140
CuS/CdS(H)/CdS(C)	Visible-light irradiation ( $>420 \text{ nm}$ )	$2042 \text{ mmol g}^{-1} \text{ h}^{-1}$	—	192
$\text{TiO}_2/\text{CdS}$		$51.4 \text{ mol h}^{-1}$	—	193
ZnO/CdS	350 W xenon lamp	$4134 \text{ } \mu\text{mol g}^{-1} \text{ h}^{-1}$	—	194
$\text{In}_2\text{Se}_3/\text{CdS}$	300 W Xe lamp	$1.632 \text{ mmol g}^{-1} \text{ h}^{-1}$	—	196
CdS branched $\text{TiO}_2$ nanoarrays	Solar light	$11.9 \text{ } \mu\text{mol cm}^{-2} \text{ h}^{-1}$	—	197
NiS/CdS NFs	300 W Xe lamp ( $>420 \text{ nm}$ )	$30.1 \text{ mmol h}^{-1} \text{ g}^{-1}$	43%	198
$\text{Co}_9\text{S}_8/\text{Cd}/\text{CdS}$	Visible-light	$10.42 \text{ } \mu\text{mol h}^{-1}$	—	199
CdS/Au/ZnO	300 W Xe lamp with a 420 nm	$102.9 \text{ mmol h}^{-1}$	9.6%	200
CdS/DETA	Solar light	$8059 \text{ } \mu\text{mol g}^{-1} \text{ h}^{-1}$	—	201
PANI@CdS	Visible-light	$310 \text{ mol h}^{-1} \text{ g}^{-1}$	—	202
G-CdS	Visible-light	$1.12 \text{ mmol h}^{-1}$	22.5%	27
$\text{g-C}_3\text{N}_4/\text{CdS}$	UV cutoff filter ( $\geq 420 \text{ nm}$ )	$5303 \text{ } \mu\text{mol h}^{-1} \text{ g}^{-1}$	—	203

field of semiconductor photocatalysts. Table 3 lists the photocatalytic hydrogen evolution activities of the CdS-based catalysts. However, much more research is still required to make it more successful for commercial applications.

### 3.3. Photocatalytic CO<sub>2</sub> reduction

The CO<sub>2</sub> concentration in the atmosphere keeps increasing owing to the consumption of fossil fuels. The climate change issues served by the over-emitted CO<sub>2</sub> and the energy shortage crisis become a great concern of human society. The photocatalytic reduction of CO<sub>2</sub> that uses clean solar light as the power to drive the catalytic reactions is considered one of the most desirable approaches to alleviate the energy and environmental issues simultaneously.<sup>220</sup> Briefly, the photocatalytic CO<sub>2</sub> reduction usually involves several steps (taking CO<sub>2</sub> to CO as an example): (1) the photogeneration of the electron and holes; (2) the oxidation of H<sub>2</sub>O to generate H<sup>+</sup>; (3) the activation of CO<sub>2</sub> to generate CO<sub>2</sub><sup>\*</sup>; (4) the proton-coupled reduction process of CO<sub>2</sub><sup>\*</sup> to CO<sup>\*</sup>; (5) the desorption of CO.<sup>221</sup>



As illustrated in the equations above, many steps in the photoreduction of CO<sub>2</sub> require large energy inputs. The energy of the photo-induced electrons should be more negative than the redox potential of the CO<sub>2</sub> reduction reactions (*e.g.*  $-0.53$  V for  $\text{CO}_2 + 2\text{H}^+ + 2e^- \rightarrow \text{CO} + \text{H}_2\text{O}$  at pH 7 in an aqueous solution *versus* a Normal Hydrogen Electrode (NHE)),<sup>222</sup> while the energy of the photo-induced holes should be more positive than the redox potential of the H<sub>2</sub>O oxidation. It demands that the photocatalysts applied in the CO<sub>2</sub> reduction provide at least equivalent CB and VB positions to proceed with the reduction processes. CdS with the ability to harvest visible light (bandgap of around 2.4 eV) while affording suitable CB and VB potentials attracts much attention in the field.<sup>59,75,78</sup>

**3.3.1. The Z-scheme charge transfer of CdS heterostructures.** The high charge recombination rate of CdS is always a problem for photocatalytic performance. To improve the separation efficiency of photo-generated electron-hole pairs, constructing the photocatalysts with a Z-scheme charge transfer route is effective.<sup>223</sup> Long *et al.*<sup>223</sup> designed an  $\alpha\text{-Fe}_2\text{O}_3$ @CdS with the 2D/2D bilayer structure for the photocatalytic reduction of CO<sub>2</sub> to CO. The 2D/2D hetero-nanostructure was fabricated by anchoring the  $\alpha\text{-Fe}_2\text{O}_3$  nanosheets (NSs) with strong photooxidation ability on the ultrathin flower-shaped CdS NSs with strong photoreduction ability (Fig. 26a). This 2D/2D heterostructure generated the heterointerface electronic regulations in the catalysts, constructing an internal built-in electric field from CdS to  $\alpha\text{-Fe}_2\text{O}_3$ . Fig. 26b depicts the built-in electric field in the interface between CdS and  $\alpha\text{-Fe}_2\text{O}_3$  where the photo-induced electron from the CB of  $\alpha\text{-Fe}_2\text{O}_3$  would recombine with the photo-induced holes from the VB of CdS to form the Z-scheme charge transfer pathway. It prohibited the charge recombination of the most effective photo-induced electron and holes in  $\alpha\text{-Fe}_2\text{O}_3$ @CdS and promoted photocatalytic performance. The  $\alpha\text{-Fe}_2\text{O}_3$ @CdS catalyst achieved highly selective and continuous CO production reaching  $9 \mu\text{mol g}^{-1}$  under simulated solar light irradiation in the first hour of the reaction (Fig. 26c). The better photocatalytic CO production efficiency

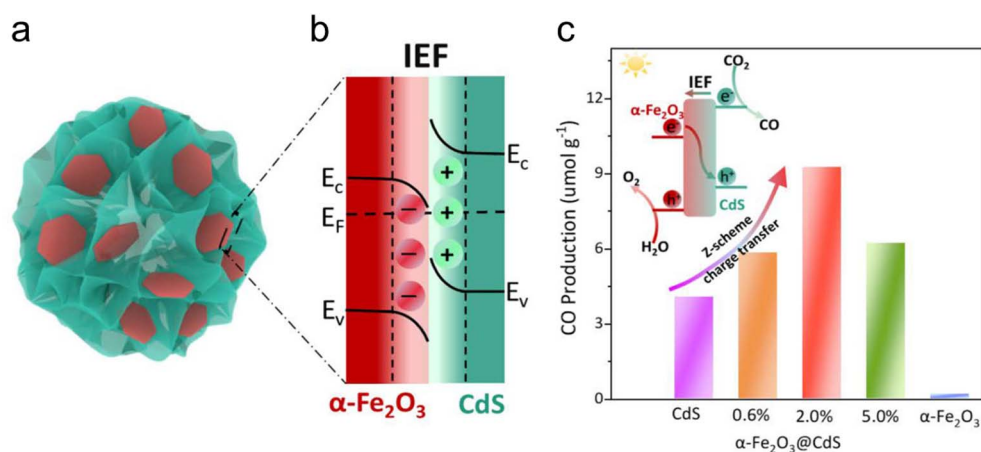


Fig. 26 (a) The illustration of the 2D/2D  $\alpha\text{-Fe}_2\text{O}_3$ @CdS heterostructure. (b) The illustration of the energy band offsets and the heterointerface electronic property of the 2D/2D  $\alpha\text{-Fe}_2\text{O}_3$ @CdS heterostructure. (c) The CO production of photocatalytic CO<sub>2</sub> conversion changes along with the time of simulated solar light irradiation. Comparison of photocatalytic activity over different samples in the first hour. (Inset) The Z-scheme charge transfer pathway for the photocatalytic CO<sub>2</sub> conversion and H<sub>2</sub>O oxidation.<sup>223</sup>

than that of the pure CdS and  $\alpha$ -Fe<sub>2</sub>O<sub>3</sub> was attributed to the formation of an internal electric field directed from CdS to  $\alpha$ -Fe<sub>2</sub>O<sub>3</sub>, resulting in the efficient Z-scheme charge transfer in the heterostructure (Fig. 26c, insert).<sup>223</sup>

**3.3.2. CdS/other semiconductor-based hierarchical 3D nano-architectures.** In addition to the Z-scheme strategy, common heterojunctions are more easily to be constructed in CdS-based semiconductor photocatalysts. Besides, the porous or hierarchical structures that increase the surface area bring

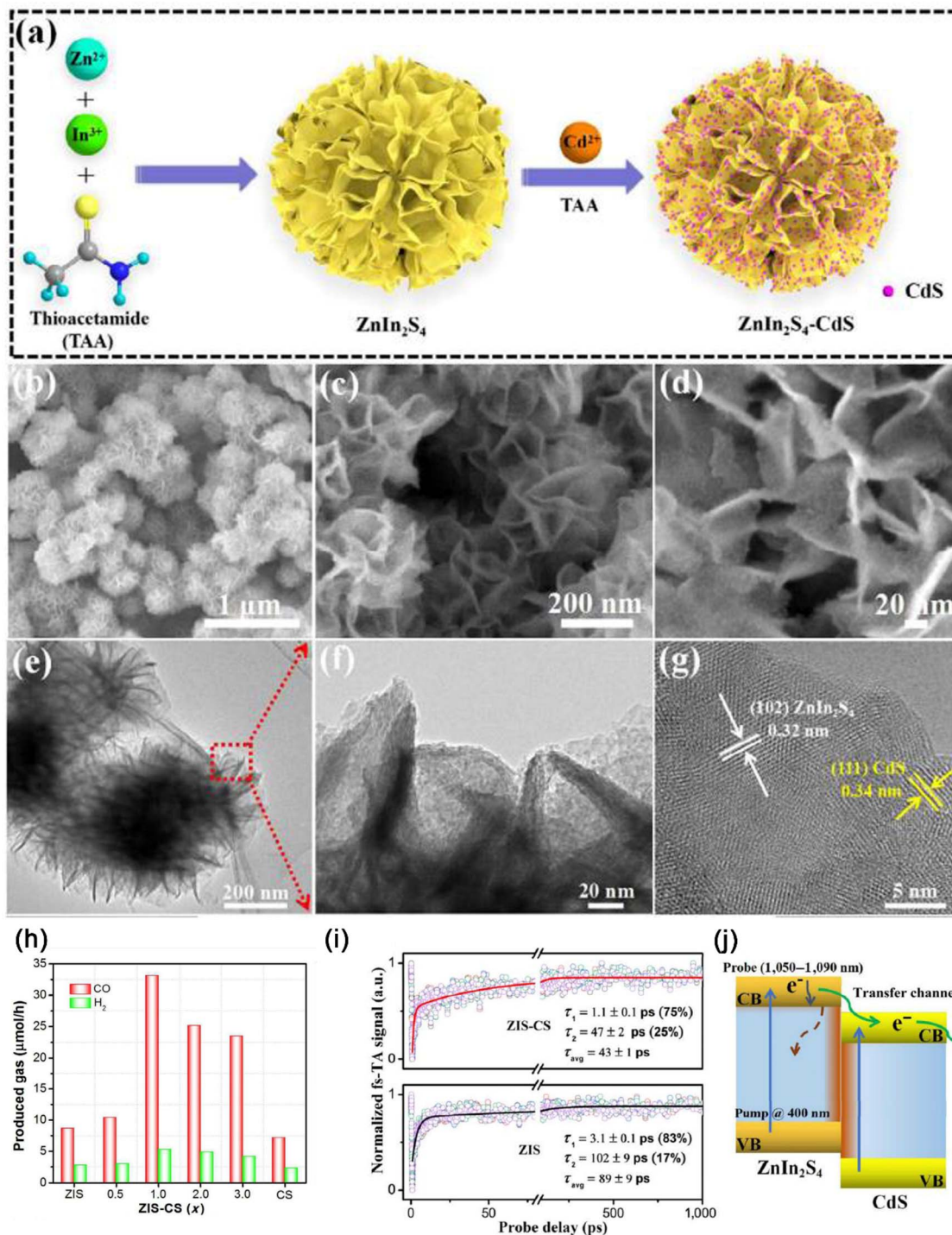


Fig. 27 (a) The schematic of the synthetic procedure of CdS QDs/ZIS NFs composites, (b)–(d) SEM, (e)–(g) TEM, and HR-TEM images of the CdS QDs/ZIS NFs composites. (h) The photocatalytic CO<sub>2</sub> reduction rates for ZnIn<sub>2</sub>S<sub>4</sub>-CdS, ZnIn<sub>2</sub>S<sub>4</sub>, and CdS catalysts, (i) the ultrafast kinetics and the global fitting results (probing in the range 1050–1090 nm using a 10 nm interval) for ZnIn<sub>2</sub>S<sub>4</sub>-CdS, ZnIn<sub>2</sub>S<sub>4</sub>. (j) The schematic illustration of the photogenerated electrons. Reprinted with permission from ref. 224.

extra benefits to photocatalytic CO<sub>2</sub> reduction. Coupling the heterostructure strategy with the hierarchical structure construction can further improve the photocatalytic performance of CO<sub>2</sub> reduction. The confining of 0D CdS quantum dots on 3D nanostructures is a good way to achieve the hierarchical heterostructure of CdS-based catalysts. Zhu *et al.*<sup>224</sup> constructed the 0D CdS quantum dots on the 3D ZnIn<sub>2</sub>S<sub>4</sub> nanoflowers for photocatalytic CO<sub>2</sub> reduction. Through a two-step synthetic method, 0D CdS quantum dots were confined on the 3D ZnIn<sub>2</sub>S<sub>4</sub> nano-flowers (CdS QDs/ZIS NFs, Fig. 27a–g). The hierarchical heterostructured CdS QDs/ZIS NFs showed excellent photocatalytic performances toward CO production with a remarkable CO yield rate of 33.4 μmol h<sup>-1</sup> (3340 μmol h<sup>-1</sup> g<sup>-1</sup>) and an 86.7% product selectivity of CO *versus* H<sub>2</sub> under visible light irradiation, which is superior to those of the pure ZnIn<sub>2</sub>S<sub>4</sub> and CdS catalysts (Fig. 27h). The ultrafast transient absorption (TA) spectroscopy demystified that the channels formed in heterostructures promoted the electron transfer between ZnIn<sub>2</sub>S<sub>4</sub> and CdS (Fig. 27i, Fig. 27j depicts the charge transfer pathway of CdS QDs/ZIS NFs). The heterojunction in the interface between ZnIn<sub>2</sub>S<sub>4</sub> and CdS facilitates the transfer of the photo-induced electron from the CB of ZnIn<sub>2</sub>S<sub>4</sub> to the CB of CdS. It helps the separation of the photo-induced carriers, resulting in augmented photocatalytic performance. The hierarchical nanohybrids of CdS QDs/ZIS NFs are effective to promote photocatalytic CO<sub>2</sub> reduction with the promoted electron transfer efficiency and exposed active sites and areas for the reaction and light-harvesting.<sup>224</sup>

**3.3.3. CdS/MOF-based 3D nano-architectures.** The MOF materials with tunable flexibilities in the metal nodes and topology structures are widely studied in the field of CO<sub>2</sub> reduction.<sup>225,226</sup> MOF-based materials can also be used as the hierarchical-structured substrate to host the 0D CdS catalysts.<sup>221</sup>

Xu *et al.*<sup>221</sup> fabricated a CdS/Ni-MOF catalyst with the 3D hierarchical heterostructure for the photoreduction of CO<sub>2</sub> into CO. The flower-shaped Ni-MOF was prepared through a simple hydrothermal method. Then, CdS particles were grown on the hierarchical Ni-MOF substrate to form the 3D heterostructure (Fig. 28a). The CB and VB values of Ni-MOF and CdS are -1.37 eV and +1.93 eV, -0.94 eV, and +1.06 eV, respectively. It meets the requirements of CO<sub>2</sub> reduction. The 3D hierarchical heterostructure prevented the aggregation of CdS, increased the active surface area, and improved light-harvesting while promoting the separation of the photogenerated electron-hole pairs. The synergy of these benefits resulted in enhanced photocatalytic CO<sub>2</sub> reduction performance (Fig. 28b). The CdS/Ni-MOF catalysts inhibited the H<sub>2</sub> production but promoted the CO and CH<sub>4</sub> yields (Fig. 28c, e and f). The catalyst of 20%-CdS/Ni-MOF exhibited the best performance for photocatalytic reduction of CO<sub>2</sub> to CO with the CO yield of 7.47 μmol g<sup>-1</sup> in the fourth hour, which was almost 16 times and 7 times that of the Ni-MOF and pure CdS (Fig. 28c and d). The CO yield of 30%-CdS/Ni-MOF and 40%-CdS/Ni-MOF decreased quickly. This may be due to the excessive loading of CdS, damaging the hierarchical structure of the CdS/Ni-MOF catalyst, which resulted in a severe decrease in photocatalytic activity. The 3D hierarchical heterostructure of CdS/Ni-MOF is essential to the enhancement of photocatalytic performance.<sup>221</sup> Hollow structures also allow the catalysts to exhibit a big surface area for the abundant active sites for the catalytic reactions. Besides, hollow-structured photocatalysts can further enhance their catalytic performance with the high utilization efficiency of light harvesting by the scattering and reflection effects.<sup>227</sup>

Zhang *et al.*<sup>227</sup> fabricated CdS hierarchical multi-cavity hollow particles (HMCHPs) through a Zn-based zeolitic imidazolate framework (ZIF-8)-template method. ZIF-8 was first grown on the cobalt glycerate solid spheres (Co-G SSS) to

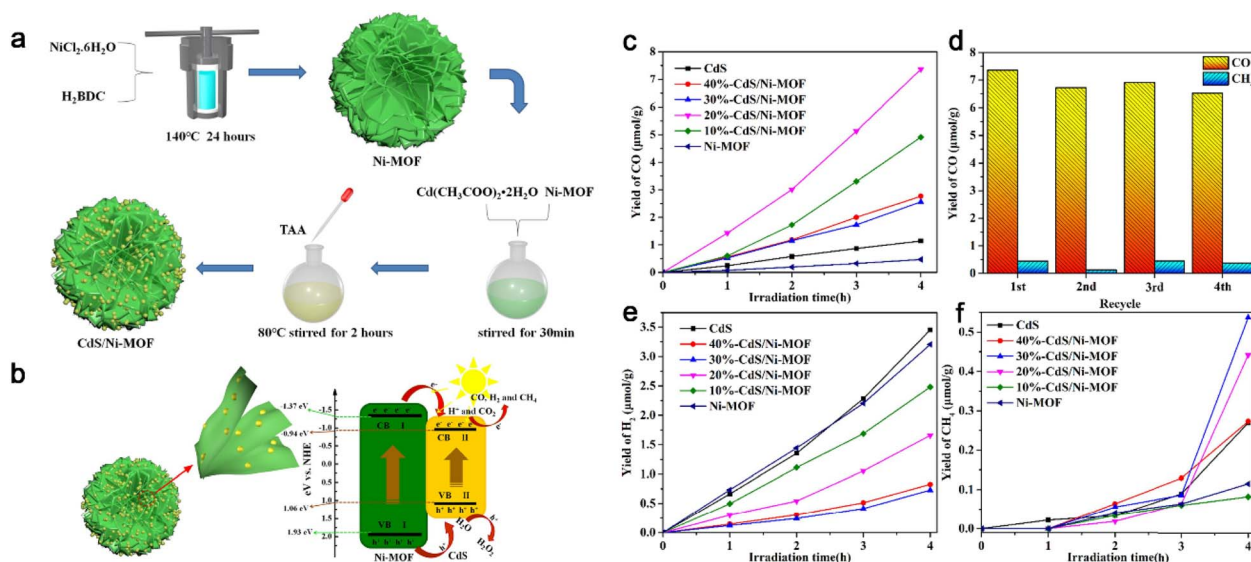


Fig. 28 (a) The schematic of the synthetic procedure of CdS/Ni-MOF. (b) The schematic of CdS/Ni-MOF for photocatalytic reduction of CO<sub>2</sub>. (c) CO yield; (d) repeat experiment diagram; (e and f) yields of H<sub>2</sub> and CH<sub>4</sub>. Reprinted with permission from ref. 221.

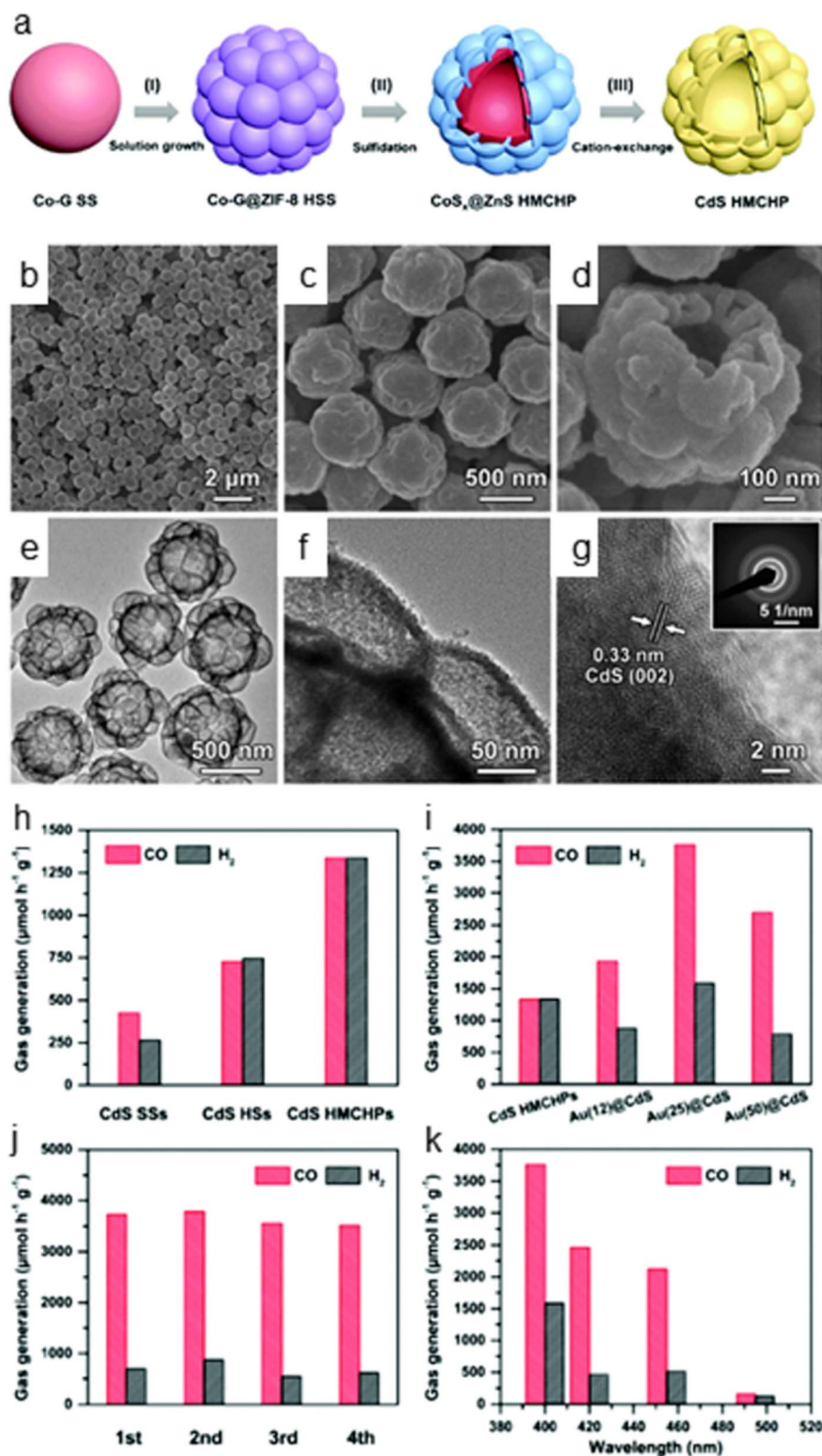


Fig. 29 (a) The schematic of the synthetic process of CdS HMCHPs. (I) Synthesis of Co-G@ZIF-8 HSSs by growing ZIF-8 onto Co-G SSs through a solution growth approach. (II) Conversion of Co-G@ZIF-8 HSSs into CoS<sub>x</sub>@ZnS HMCHPs via a sulfidation treatment. (III) Conversion of CoS<sub>x</sub>@ZnS HMCHPs into CdS HMCHPs through a cation-exchange reaction. (b–d) The FESEM images and (e and f) TEM images of the CdS HMCHPs. (g) The HRTEM image of the CdS HMCHP (inset: the SAED pattern). (h) The photocatalytic CO<sub>2</sub> reduction performance of HMCHPs, CdS SSs, and HSs. (i) The photocatalytic CO<sub>2</sub> reduction performance of the CdS HMCHPs with different loadings of Au. (j) The CO and H<sub>2</sub> stability tests for Au(25)@CdS HMCHPs. (k) The wavelength-dependent yields of CO and H<sub>2</sub> for Au(25)@CdS HMCHPs. Reprinted with permission from ref. 227.

Table 4 The photocatalytic activities of some typical CdS-based semiconductor catalysts

Catalyst	Light source	Production rate	Stability	Ref.
CdS-S <sup>2-</sup>	340 nm > λ > 450 nm	CO: 2130 μmol g <sup>-1</sup> h <sup>-1</sup>	6 h	228
CdS/NC	Visible light (λ > 420 nm)	CO: 2130 μmol g <sup>-1</sup> h <sup>-1</sup>	5 h	229
α-Fe <sub>2</sub> O <sub>3</sub> /CdS	AM 1.5G light	CO: 9.3 μmol g <sup>-1</sup> h <sup>-1</sup>	6 h	223
ZnIn <sub>2</sub> S <sub>4</sub> -CdS	Visible light (λ > 420 nm)	CO: 2182.5 μmol g <sup>-1</sup> h <sup>-1</sup>	20 h	224
CdS/Ni-MOF	300 W xenon lamp	CO: 7.47 μmol g <sup>-1</sup> h <sup>-1</sup>	16 h	221
CoS <sub>x</sub> @ZnS HMCHPs	Visible light (λ > 400 nm)	CO: 1337 μmol h <sup>-1</sup> g <sup>-1</sup>	4 h	227

construct Co-G@ZIF-8 hierarchical solid spheres. Followed by a sulfidation reaction, CoS<sub>x</sub>@ZnS HMCHPs were prepared (Fig. 29a). TEM revealed that the CoS<sub>x</sub>@ZnS HMCHPs particles were made of a central spherical chamber covered by interconnected small cavities. The shell of the hollow-structured particles was composed of small cavities generated from the transformation from quasi-spherical ZIF-8 particles to sulfide materials (Fig. 29b–g). CdS HMCHPs had the best catalytic performance with a CO yield rate of around 1337 μmol h<sup>-1</sup> g<sup>-1</sup> among all the comparisons (Fig. 29h). With the addition of Au particles to the catalysts, the CO generation rate could be further promoted (Fig. 29i) with excellent stability (Fig. 29j) and visible light response (Fig. 29k).

The CdS-based hierarchical 3D nano-architectures have the potential to be promising visible light active materials with better stability and corrosion-resistant capability. The application of such nanomaterials especially CO<sub>2</sub> reduction has been an emerging area and great efforts are being done in the field, as listed in Table 4 below.

## 4. Challenges

As a robust photocatalytic material, CdS has received a lot of attention. Its potential for producing solar fuel and cleaning the environment has also seen some notable advancements. Numerous studies have demonstrated that altering external factors such as the polytropic synthesis parameters, the type and concentration of reactants, morphology, size, structures, and other factors can change the photocatalytic activity of CdS photocatalysts. However, CdS-based nanomaterials have several challenges that need to be addressed to fully realize their potential in a wide range of applications such as:

- CdS is a toxic element and exposure to it can negatively affect the environment and human health. Due to this, it is essential to develop more efficient ways to recover and recycle CdS. Furthermore, the potential release of CdS nanoparticles into the environment can adversely affect wildlife, plants, and human health. Therefore, toxicity and environmental studies are needed to assess the risk of CdS-based nanomaterials.<sup>230,231</sup>

- Photocorrosion is a general phenomenon during the photocatalytic process for CdS-based photocatalysts resulting in its limited application in the industrial sector. The causes of the photocorrosion are: (i) the oxidation of sulfur ions into sulfur by photogenerated holes and (ii) the occurrence of redox reactions on the surface of CdS under anaerobic environment. Therefore, more investigation is required to determine the cause of the

photocorrosion of CdS and increased lattice stress-strain when exposed to an air environment during photocatalysis.<sup>18</sup>

- It has been found that the size and shape of nanostructures show significant influence on their physical/chemical properties and further on their functionality. Hence, morphology is an important parameter that influences photocatalytic activity. However, fabricating such nanostructures or hybrid nanostructures with complex morphology is challenging as they require high preparation skills. Therefore, synthesizing CdS nanoparticles is challenging and not well-controlled yet, making it difficult to produce large quantities of efficient CdS-based nanomaterials.<sup>232</sup>

- CdS-based photocatalysts can be made in a variety of ways, but it is still challenging to produce them on a large scale with high quality. In addition, the CdS-based photocatalysts should exhibit high performance with excellent properties such as desired size and ideal morphology.

- The photocatalytic reaction mechanism of CdS-based photocatalysts is still unclear; however, most reports suggest that the separation of charge carriers and the interaction of reactive oxygen species (ROS) like hydroxyl radicals were responsible for the enhanced photocatalytic activity. It appears that additional parameters, such as crystal size, morphology, and shape, can also affect the performance of CdS-based photocatalysts. It is important to continue researching and developing new methods to fully address these challenges to fully realize the potential of CdS-based nanomaterials.

## 5. Conclusion & future perspectives

CdS is a type of semiconductor material that has been widely studied for its potential use as a photocatalyst, due to its ability to absorb light and convert it into chemical energy. CdS nanomaterials, specifically, have been shown to have high photocatalytic activity for a wide range of applications, including CO<sub>2</sub> reduction, water splitting and complex organic pollutant mineralization.

In the current review, we have given a broad overview of the different morphologies of CdS nanostructures, as well as their photocatalytic characteristics and mechanisms under varied morphologies. Additionally, particular focus has been placed on several photocatalytic applications for CdS-based 3D nano-architectures, including the degradation of complex organic pollutants, the production of H<sub>2</sub> by water splitting, and the photoreduction of CO<sub>2</sub>. Based on their intended uses, CdS-based nanomaterials are further divided into polymer-based,



carbon-based, metal oxide-based, nanocomposites-based, transition metal-based, organic material-based, and MOF-based categories.

Even though CdS-based catalysts have already made considerable progress, more work needs to be done before they can be used in competitive and realistic industrial-scale applications. Exploring research areas like:

- Charge transfer properties for CdS-based photocatalysts are an area that has not been sufficiently researched. Therefore, further modification is required to improve the charge separation and transfer. This can be achieved by using advanced materials and structures such as quantum dots, core-shell structures, and doped CdS photocatalysts. For instance, Li *et al.*, synthesized  $\text{Ti}_3\text{CN@TiO}_2/\text{CdS}$  heterojunction, which showed excellent stability and photocatalytic performance.<sup>233</sup> To effectively prevent photo-corrosion of CdS-based structures, interface engineering can be used to avoid recombining produced electron-hole pairs and accelerate charge separation.

- It is desirable to design Z-scheme structures for CdS-based nanomaterials, which ensures close contact between CdS and other materials resulting in high  $\text{H}_2$  production efficiency. For instance, Meng *et al.* created Z-scheme CdS/ $\text{TiO}_2$  hierarchical systems for photocatalytic hydrogen generation through water splitting under solar irradiation, and the  $\text{H}_2$  production rate could reach  $51.4 \text{ mol h}^{-1}$ .<sup>206</sup>

- A deep understanding of reaction mechanisms and the transfer of electrons between the interfaces could result in significant improvement in the process efficiency. In the future, more significant effort should be put into examining the linkages between the structures, functions, and mechanisms of photocatalytic processes.<sup>234</sup> Further other factors of CdS-based photocatalysts also affect the overall activity, such as morphological properties, crystal size, shape, *etc.* Therefore, more attention should be given to this aspect as these factors are also crucial for controlling and designing of CdS based photocatalytic nanomaterials.

- New strategies must be used to create new CdS-based catalysts, including selective doping, defect engineering, nanostructural modification, increased porosity, conductivity management, and temperature control. Using an alternative way to increase the activity of CdS and CdS-based photocatalysts can be highly beneficial by decorating them with single atoms. The individual atoms may be placed into the CdS layer or onto the interior or exterior of CdS nanorods, nanowires, hollow shells, and nanotubes, resulting in outstanding photocatalytic performance in surface reactions, extensive atomic exploitation, and charge trapping. PDA based surface modification could be promising which also helps in inhibiting photocorrosion.

- The stability of CdS-based photocatalysts is still far from the essential requirement of practical application. The construction of an anti-photocorrosion layer over a CdS photocatalyst and a more effective oxygen separation technology should be the focus of future research to remove nascent oxygen and prevent oxygen-related photocorrosion.<sup>235</sup> It has been shown that adding the right dual cocatalysts to CdS and creating heterojunctions can speed up the transfer and

migration of photogenerated charge carriers and, to some extent, inhibit the photo-corrosion process.

- There aren't many microscopic investigations of  $\text{CO}_2$  photoreduction over CdS-based photocatalysts. Theoretical information can be obtained *via* DFT calculations, an essential academic research tool, to examine the electron excitation process, energy band structure, adsorption properties, and reaction mechanism. Studying the mechanism of  $\text{CO}_2$  conversion can be aided by examining the adsorption energy of intermediates on photocatalytic materials and the related activation energy.

Furthermore, the study of dimensional anisotropy of CdS-based nanomaterials is a new subject that needs to be explored, since it may offer fresh insight into the formation of the functional heterostructure. These new research directions can increase the photocatalytic efficiencies and therefore the use of CdS-based nanomaterials in photocatalytic processes for energy and environmental applications along with other fields of applications.

## Conflicts of interest

There are no conflicts to declare.

## Acknowledgements

The author (JP) thanks the Department of Science and Technology (DST), India, for the prestigious INSPIRE Faculty award [INSPIRE/04/2015/002452(IFA15-MS-57)] along with research grant.

## References

- 1 J. Liu, X. Wei, W. Sun, X. Guan, X. Zheng and J. Li, Fabrication of S-scheme CdS-g- $\text{C}_3\text{N}_4$ -graphene aerogel heterojunction for enhanced visible light driven photocatalysis, *Environ. Res.*, 2021, **197**, 111136.
- 2 C. Zhu, X. Zhang, Y. Zhang, Y. Li, P. Wang and Y. Jia, Ultrasonic-Assisted Synthesis of CdS/Microcrystalline Cellulose Nanocomposites With Enhanced Visible-Light-Driven Photocatalytic Degradation of MB and the Corresponding Mechanism Study, *Front. Chem.*, 2022, **10**, 892680.
- 3 P. Wang, X. Zhou, Y. Shao, D. Li, Z. Zuo and X. Liu, CdS quantum dots-decorated InOOH: Facile synthesis and excellent photocatalytic activity under visible light, *J. Colloid Interface Sci.*, 2021, **601**, 186–195.
- 4 J. Jin, J. Yu, G. Liu and P. K. Wong, Single crystal CdS nanowires with high visible-light photocatalytic  $\text{H}_2$ -production performance, *J. Mater. Chem. A*, 2013, **1**, 10927–10934.
- 5 N. Ahmad, S. Sultana, S. Sabir and M. Z. Khan, Exploring the visible light driven photocatalysis by reduced graphene oxide supported Ppy/CdS nanocomposites for the degradation of organic pollutants, *J. Photochem. Photobiol., A*, 2020, **386**, 112129.

- 6 S. Sampath and K. Sellappa, Visible-light-driven photocatalysts for hydrogen production by water splitting, *Energy Sources, Part A*, 2020, **42**, 719–729.
- 7 D.-S. Chuu and C.-M. Dai, Quantum size effects in CdS thin films, *Phys. Rev. B: Condens. Matter Mater. Phys.*, 1992, **45**, 11805–11810.
- 8 H. Li, H. An, B. Chong, G. Yang and L. Wang, Homogeneous dual-site P lattice doping in CdS quantum rods for visible-light photocatalytic water splitting, *Chem. Eng. Sci.*, 2021, **238**, 116594.
- 9 R. S. Ibrahim, A. A. Azab and A. M. Mansour, Synthesis and structural, optical, and magnetic properties of Mn-doped CdS quantum dots prepared by chemical precipitation method, *J. Mater. Sci.: Mater. Electron.*, 2021, **32**, 19980–19990.
- 10 M. J. Iqbal Khan and Z. Kanwal, Investigation of optical properties of CdS for various Na concentrations for nonlinear optical applications (A DFT study), *Optik*, 2019, **193**, 162985.
- 11 S. Xiong, X. Zhang and Y. Qian, CdS with Various Novel Hierarchical Nanostructures by Nanobelts/Nanowires Self-Assembly: Controllable Preparation and Their Optical Properties, *Cryst. Growth Des.*, 2009, **9**, 5259–5265.
- 12 K. Wright and J. D. Gale, Interatomic potentials for the simulation of the zinc-blende and wurtzite forms of ZnS and CdS: Bulk structure, properties, and phase stability, *Phys. Rev. B: Condens. Matter Mater. Phys.*, 2004, **70**, 035211.
- 13 M. A. Nusimovici and J. L. Birman, Lattice Dynamics of Wurtzite: CdS, *Phys. Rev.*, 1967, **156**, 925–938.
- 14 Y.-X. Han, C.-L. Yang, Y.-T. Sun, M.-S. Wang and X.-G. Ma, The novel optical properties of CdS caused by concentration of impurity Co, *J. Alloys Compd.*, 2014, **585**, 503–509.
- 15 T. Zhai, X. Fang, L. Li, Y. Bando and D. Golberg, One-dimensional CdS nanostructures: synthesis, properties, and applications, *Nanoscale*, 2010, **2**, 168–187.
- 16 B.-S. Moon, J.-H. Lee and H. Jung, Comparative studies of the properties of CdS films deposited on different substrates by R. F. sputtering, *Thin Solid Films*, 2006, **511–512**, 299–303.
- 17 L. Ma, M. Liu, D. Jing and L. Guo, Photocatalytic hydrogen production over CdS: effects of reaction atmosphere studied by *in situ* Raman spectroscopy, *J. Mater. Chem. A*, 2015, **3**, 5701–5707.
- 18 X. Ning and G. Lu, Photocorrosion inhibition of CdS-based catalysts for photocatalytic overall water splitting, *Nanoscale*, 2020, **12**, 1213–1223.
- 19 L. Wei, Z. Guo and X. Jia, Probing Photocorrosion Mechanism of CdS Films and Enhancing Photoelectrocatalytic Activity via Cocatalyst, *Catal. Lett.*, 2021, **151**, 56–66.
- 20 X. Ning, J. Li, B. Yang, W. Zhen, Z. Li, B. Tian, *et al.*, Inhibition of photocorrosion of CdS via assembling with thin film TiO<sub>2</sub> and removing formed oxygen by artificial gill for visible light overall water splitting, *Appl. Catal., B*, 2017, **212**, 129–139.
- 21 A. Singh, D. Singh, B. Ahmed and A. K. Ojha, Sun/UV-light driven photocatalytic degradation of rhodamine B dye by Zn doped CdS nanostructures as photocatalyst, *Mater. Chem. Phys.*, 2022, **277**, 125531.
- 22 Y. Tang, X. Hu and C. Liu, Perfect inhibition of CdS photocorrosion by graphene sheltering engineering on TiO<sub>2</sub> nanotube array for highly stable photocatalytic activity, *Phys. Chem. Chem. Phys.*, 2014, **16**, 25321–25329.
- 23 J. Mao, X. M. Chen and X. W. Du, Facile synthesis of three dimensional CdS nanoflowers with high photocatalytic performance, *J. Alloys Compd.*, 2016, **656**, 972–977.
- 24 Q. Wang, J. Lian, J. Li, R. Wang, H. Huang, B. Su, *et al.*, Highly Efficient Photocatalytic Hydrogen Production of Flower-like Cadmium Sulfide Decorated by Histidine, *Sci. Rep.*, 2015, **5**, 13593.
- 25 J. Yu, Y. Yu, P. Zhou, W. Xiao and B. Cheng, Morphology-dependent photocatalytic H<sub>2</sub>-production activity of CdS, *Appl. Catal., B*, 2014, **156–157**, 184–191.
- 26 Z. Tian, N. Yu, Y. Cheng, Z. Wang, Z. Chen and L. Zhang, Hydrothermal synthesis of graphene/TiO<sub>2</sub>/CdS nanocomposites as efficient visible-light-driven photocatalysts, *Mater. Lett.*, 2017, **194**, 172–175.
- 27 Q. Li, B. Guo, J. Yu, J. Ran, B. Zhang, H. Yan, *et al.*, Highly Efficient Visible-Light-Driven Photocatalytic Hydrogen Production of CdS-Cluster-Decorated Graphene Nanosheets, *J. Am. Chem. Soc.*, 2011, **133**, 10878–10884.
- 28 J. Xu, W.-M. Yang, S.-J. Huang, H. Yin, H. Zhang, P. Radjenovic, *et al.*, CdS core-Au plasmonic satellites nanostructure enhanced photocatalytic hydrogen evolution reaction, *Nano Energy*, 2018, **49**, 363–371.
- 29 N. Singh, J. Prakash and R. K. Gupta, Design and engineering of high-performance photocatalytic systems based on metal oxide–graphene–noble metal nanocomposites, *Mol. Syst. Des. Eng.*, 2017, **2**, 422–439.
- 30 J. Prakash, S. Sun, H. C. Swart and R. K. Gupta, Noble metals-TiO<sub>2</sub> nanocomposites: From fundamental mechanisms to photocatalysis, surface enhanced Raman scattering and antibacterial applications, *Appl. Mater. Today*, 2018, **11**, 82–135.
- 31 Q. Li, X. Li, S. Wageh, A. A. Al-Ghamdi and J. Yu, CdS/Graphene Nanocomposite Photocatalysts, *Adv. Energy Mater.*, 2015, **5**, 1500010.
- 32 P. Kumar, M. C. Mathpal, J. Prakash, S. Hamad, S. V. Rao, B. C. Viljoen, *et al.*, Study of Tunable Plasmonic, Photoluminescence, and Nonlinear Optical Behavior of Ag Nanoclusters Embedded in a Glass Matrix for Multifunctional Applications, *Phys. Status Solidi A*, 2019, **216**, 1800768.
- 33 P. Kumar, M. Chandra Mathpal, J. Prakash, G. Jagannath, W. D. Roos and H. C. Swart, Plasmonic and nonlinear optical behavior of nanostructures in glass matrix for photonics application, *Mater. Res. Bull.*, 2020, **125**, 110799.
- 34 J. Prakash, R. A. Harris and H. C. Swart, Embedded plasmonic nanostructures: synthesis, fundamental aspects and their surface enhanced Raman scattering applications, *Int. Rev. Phys. Chem.*, 2016, **35**, 353–398.

- 35 M. C. Mathpal, P. Kumar, S. Kumar, A. K. Tripathi, M. K. Singh, J. Prakash, *et al.*, Opacity and plasmonic properties of Ag embedded glass based metamaterials, *RSC Adv.*, 2015, 5, 12555–12562.
- 36 J. Prakash, J. C. Pivin and H. C. Swart, Noble metal nanoparticles embedding into polymeric materials: From fundamentals to applications, *Adv. Colloid Interface Sci.*, 2015, 226, 187–202.
- 37 J. Prakash, K. A. Samriti, H. Dai, B. C. Janegitz, V. Krishnan, *et al.*, Novel rare earth metal-doped one-dimensional TiO<sub>2</sub> nanostructures: Fundamentals and multifunctional applications, *Mater. Today Sustain.*, 2021, 13, 100066.
- 38 J. Prakash, Fundamentals and applications of recyclable SERS substrates, *Int. Rev. Phys. Chem.*, 2019, 38, 201–242.
- 39 J. Prakash, P. Kumar, R. A. Harris, C. Swart, J. H. Neethling, A. J. van Vuuren, *et al.*, Synthesis, characterization and multifunctional properties of plasmonic Ag–TiO<sub>2</sub> nanocomposites, *Nanotechnology*, 2016, 27, 355707.
- 40 A. Chakraborty, R. O. Samriti, R. K. Gupta, J. Cho and J. Prakash, TiO<sub>2</sub> nanoflower photocatalysts: Synthesis, modifications and applications in wastewater treatment for removal of emerging organic pollutants, *Environ. Res.*, 2022, 212, 113550.
- 41 N. Singh, J. Prakash, M. Misra, A. Sharma and R. K. Gupta, Dual Functional Ta-Doped Electrospun TiO<sub>2</sub> Nanofibers with Enhanced Photocatalysis and SERS Detection for Organic Compounds, *ACS Appl. Mater. Interfaces*, 2017, 9, 28495–28507.
- 42 C. Yang, Y. Zhang, F. Xiong and Y. Sun, Photocorrosion of CdS nanorod arrays and fabrication of CdS@TiO<sub>2</sub> core@shell nanorod arrays by atomic layer deposition for improved photostability, *Opt. Mater.: X*, 2021, 9, 100070.
- 43 X. Yang, G. Zhang, J. Prakash, Z. Chen, M. Gauthier and S. Sun, Chemical vapour deposition of graphene: layer control, the transfer process, characterisation, and related applications, *Int. Rev. Phys. Chem.*, 2019, 38, 149–199.
- 44 Y.-P. Lin, Y. Ksari, J. Prakash, L. Giovanelli, J.-C. Valmalette and J.-M. Themlin, Nitrogen-doping processes of graphene by a versatile plasma-based method, *Carbon*, 2014, 73, 216–224.
- 45 M. Samriti, Z. Chen, S. Sun and J. Prakash, Design and engineering of graphene nanostructures as independent solar-driven photocatalysts for emerging applications in the field of energy and environment, *Mol. Syst. Des. Eng.*, 2022, 7, 213–238.
- 46 Z. Chen, G. Zhang, J. Prakash, Y. Zheng and S. Sun, Rational Design of Novel Catalysts with Atomic Layer Deposition for the Reduction of Carbon Dioxide, *Adv. Energy Mater.*, 2019, 9, 1900889.
- 47 J. Prakash, A. Tripathi, S. A. Khan, J. C. Pivin, F. Singh, J. Tripathi, *et al.*, Ion beam induced interface mixing of Ni on PTFE bilayer system studied by quadrupole mass analysis and electron spectroscopy for chemical analysis, *Vacuum*, 2010, 84, 1275–1279.
- 48 J. Prakash, H. C. Swart, G. Zhang and S. Sun, Emerging applications of atomic layer deposition for the rational design of novel nanostructures for surface-enhanced Raman scattering, *J. Mater. Chem. C*, 2019, 7, 1447–1471.
- 49 P. Sharma, J. Kherb, J. Prakash and R. Kaushal, A novel and facile green synthesis of SiO<sub>2</sub> nanoparticles for removal of toxic water pollutants, *Appl. Nanosci.*, 2021, 13, 735–747.
- 50 T. Gupta, Samriti, J. Cho and J. Prakash, Hydrothermal synthesis of TiO<sub>2</sub> nanorods: formation chemistry, growth mechanism, and tailoring of surface properties for photocatalytic activities, *Mater. Today Chem.*, 2021, 20, 100428.
- 51 P. Samriti, M. C. Joshi, R. K. Gupta and J. Prakash, Hydrothermal synthesis and Ta doping of TiO<sub>2</sub> nanorods: Effect of soaking time and doping on optical and charge transfer properties for enhanced SERS activity, *Mater. Chem. Phys.*, 2022, 278, 125642.
- 52 J. Prakash, Samriti, D. N. Wijesundera, I. Rajapaksa and W.-K. Chu, Ion beam nanoengineering of surfaces for molecular detection using surface enhanced Raman scattering, *Mol. Syst. Des. Eng.*, 2022, 7, 411–421.
- 53 P. Sharma, J. Prakash and R. Kaushal, An insight into the green synthesis of SiO<sub>2</sub> nanostructures as a novel adsorbent for removal of toxic water pollutants, *Environ. Res.*, 2022, 212, 113328.
- 54 S. Ghosh, A. Datta and A. Saha, Single step synthesis of highly stable good quality water soluble semiconductor/dendrimer nanocomposites through irradiation route, *Colloids Surf., A*, 2010, 355, 130–138.
- 55 J. Liu, X. Liang, Y. Wang, B. Wang, T. Zhang and F. Yi, Preparation of CdS nanorods on silicon nanopillars surface by hydrothermal method, *Mater. Res. Bull.*, 2019, 120, 110591.
- 56 M. Liu, X. Xie, L. Chen, X. Wang, Y. Cheng, F. Lu, *et al.*, A Rational Design of Heterojunction Photocatalyst CdS Interfacing with One Cycle of ALD Oxide, *J. Mater. Sci. Technol.*, 2016, 32, 489–495.
- 57 A. R. Kuldeep, R. D. Waghmare and K. M. Garadkar, Green synthesis of TiO<sub>2</sub>/CDs nanohybrid composite as an active photocatalyst for the photodegradation of methyl orange, *J. Mater. Sci.: Mater. Electron.*, 2022, 33, 7933–7944.
- 58 S. G. Kumar, R. Kavitha and P. M. Nithya, Tailoring the CdS surface structure for photocatalytic applications, *J. Environ. Chem. Eng.*, 2020, 8, 104313.
- 59 S. Chandramohan, R. Sathyamoorthy, P. Sudhagar, D. Kanjilal, D. Kabiraj and K. Asokan, Swift heavy ion beam irradiation induced modifications in structural, morphological and optical properties of CdS thin films, *Nucl. Instrum. Methods Phys. Res., Sect. B*, 2007, 254, 236–242.
- 60 S. Soundeswaran, O. Senthil Kumar, P. Ramasamy, D. Kabi Raj, D. K. Avasthi and R. Dhanasekaran, Effect of Si ion irradiation on polycrystalline CdS thin film grown from novel photochemical deposition technique, *Phys. B*, 2005, 355, 222–230.
- 61 L. Cheng, Q. Xiang, Y. Liao and H. Zhang, CdS-Based photocatalysts, *Energy Environ. Sci.*, 2018, 11, 1362–1391.
- 62 A. Priyam, S. Ghosh, S. C. Bhattacharya and A. Saha, Supersaturation driven tailoring of photoluminescence

- efficiency and size distribution: A simplified aqueous approach for producing high-quality, biocompatible quantum dots, *J. Colloid Interface Sci.*, 2009, **333**, 195–201.
- 63 F. Chen, R. Zhou, L. Yang, N. Liu, M. Wang and H. Chen, Large-Scale and Shape-Controlled Syntheses of Three-Dimensional CdS Nanocrystals with Flowerlike Structure, *J. Phys. Chem. C*, 2008, **112**, 1001–1007.
- 64 T. Di Luccio, A. M. Laera, L. Tapfer, S. Kempter, R. Kraus and B. Nickel, Controlled Nucleation and Growth of CdS Nanoparticles in a Polymer Matrix, *J. Phys. Chem. B*, 2006, **110**, 12603–12609.
- 65 M. Iqbal, A. Ali, N. A. Nahyoon, A. Majeed, R. Pothu, S. Phulpoto, *et al.*, Photocatalytic degradation of organic pollutant with nanosized cadmium sulfide, *Mater. Sci. Energy Technol.*, 2019, **2**, 41–45.
- 66 A. M. A. Al-Hussam and S. A.-J. Jassim, Synthesis, structure, and optical properties of CdS thin films nanoparticles prepared by chemical bath technique, *J. Assoc. Arab Univ. Basic Appl. Sci.*, 2012, **11**, 27–31.
- 67 S. Yan, L. Sun, P. Qu, N. Huang, Y. Song and Z. Xiao, Synthesis of uniform CdS nanowires in high yield and its single nanowire electrical property, *J. Solid State Chem.*, 2009, **182**, 2941–2945.
- 68 H. Li, S. Xiao, J. Zhou, J. Zhao, F. Liu, G. Li, *et al.*, A flexible CdS nanorods-carbon nanotubes/stainless steel mesh photoanode for boosted photoelectrocatalytic hydrogen evolution, *Chem. Commun.*, 2019, **55**, 2741–2744.
- 69 S. Shenoy, E. Jang, T. J. Park, C. S. Gopinath and K. Sridharan, Cadmium sulfide nanostructures: Influence of morphology on the photocatalytic degradation of erioglaucine and hydrogen generation, *Appl. Surf. Sci.*, 2019, **483**, 696–705.
- 70 L. Wang, Z. Liu, J. Han, R. Li and M. Huang, Stepwise Synthesis of Au@CdS-CdS Nanoflowers and Their Enhanced Photocatalytic Properties, *Nanoscale Res. Lett.*, 2019, **14**, 148.
- 71 X. Yang, Y. Yang, B. Wang, T. Wang, Y. Wang and D. Meng, Synthesis and photocatalytic property of cubic phase CdS, *Solid State Sci.*, 2019, **92**, 31–35.
- 72 S. Ghosh, S. C. Bhattacharya and A. Saha, Probing of ascorbic acid by CdS/dendrimer nanocomposites: a spectroscopic investigation, *Anal. Bioanal. Chem.*, 2010, **397**, 1573–1582.
- 73 H. Zhao and Y. Lei, 3D Nanostructures for the Next Generation of High-Performance Nanodevices for Electrochemical Energy Conversion and Storage, *Adv. Energy Mater.*, 2020, **10**, 2001460.
- 74 T. Kalsi, H. Mitra, T. K. Roy, S. K. Godara and P. Kumar, Comprehensive Analysis of Band Gap and Nanotwinning in Cd<sub>1-x</sub>Mg<sub>x</sub>S QDs, *Cryst. Growth Des.*, 2020, **20**, 6699–6706.
- 75 P. Kumar, N. Saxena, V. Gupta, F. Singh and A. Agarwal, Correlation between surface phonon mode and luminescence in nanocrystalline CdS thin films: An effect of ion beam irradiation, *J. Appl. Phys.*, 2014, **116**, 043517.
- 76 P. Kumar, N. Saxena and V. Gupta, Vital role of Ar ambient pressure in controlled properties of nanocrystalline CdS thin films, *J. Mater. Sci.: Mater. Electron.*, 2020, **31**, 6755–6763.
- 77 P. Kumar, N. Saxena, A. Agarwal and V. Gupta, Swift Heavy Ion Induced Functionality In Nanocrystalline CdS Thin Films: Role Of Growth Temperature, *Adv. Mater. Lett.*, 2015, **6**, 820–827.
- 78 P. Kumar, N. Saxena, R. Chandra, V. Gupta, A. Agarwal and D. Kanjilal, Nanotwinning and structural phase transition in CdS quantum dots, *Nanoscale Res. Lett.*, 2012, **7**, 584.
- 79 N. Saxena, P. Kumar, V. Gupta and D. Kanjilal, Radiation stability of CBD grown nanocrystalline CdS films against ion beam irradiation for solar cell applications, *J. Mater. Sci.: Mater. Electron.*, 2018, **29**, 11013–11019.
- 80 N. Saxena, P. Kumar and V. Gupta, Effect of rapid thermal annealing temperature on the dispersion of Si nanocrystals in SiO<sub>2</sub> matrix, *AIP Conf. Proc.*, 2015, **1661**, 080026.
- 81 P. Kumar, N. Saxena, F. Singh and V. Gupta, Ion beam assisted fortification of photoconduction and photosensitivity, *Sens. Actuators, A*, 2018, **279**, 343–350.
- 82 T. Kalsi and P. Kumar, Cd<sub>1-x</sub>Mg<sub>x</sub>S CQD thin films for high performance and highly selective NIR photodetection, *Dalton Trans.*, 2021, **50**, 12708–12715.
- 83 R. Grover, R. Srivastava, O. Rana, A. K. Srivastava, K. K. Maurya, K. N. Sood, *et al.*, Electroluminescence from hybrid organic-inorganic LEDs based on thermally evaporated CdS thin films, *J. Lumin.*, 2012, **132**, 330–336.
- 84 X. Jin, Y. Fang, T. Salim, M. Feng, Z. Yuan, S. Hadke, *et al.*, Controllable Solution-Phase Epitaxial Growth of Q1D Sb<sub>2</sub>(S,Se)<sub>3</sub>/CdS Heterojunction Solar Cell with 9.2% Efficiency, *Adv. Mater.*, 2021, **33**, 2104346.
- 85 Y. Bao, Y. Yu, H. Xu, C. Guo, J. Li, S. Sun, *et al.*, Full-colour nanoprint-hologram synchronous metasurface with arbitrary hue-saturation-brightness control, *Light: Sci. Appl.*, 2019, **8**, 95.
- 86 P. Kumar, N. Saxena, S. Dewan, F. Singh and V. Gupta, Giant UV-sensitivity of ion beam irradiated nanocrystalline CdS thin films, *RSC Adv.*, 2016, **6**, 3642–3649.
- 87 N. Saxena, P. Kumar and V. Gupta, CdS nanodroplets over silica microballs for efficient room-temperature LPG detection, *Nanoscale Adv.*, 2019, **1**, 2382–2391.
- 88 S.-T. Liu, X.-P. Liu, J.-S. Chen, C.-j Mao and B.-K. Jin, Highly sensitive photoelectrochemical biosensor for microRNA159c detection based on a Ti<sub>3</sub>C<sub>2</sub>:CdS nanocomposite of breast cancer, *Biosens. Bioelectron.*, 2020, **165**, 112416.
- 89 Y.-J. Yuan, D. Chen, Z.-T. Yu and Z.-G. Zou, Cadmium sulfide-based nanomaterials for photocatalytic hydrogen production, *J. Mater. Chem. A*, 2018, **6**, 11606–11630.
- 90 N. Saxena, T. Kalsi, P. Uttam and P. Kumar, Morphological evolution in nanocrystalline CdS thin films from flowers to salt rock like structures, *Opt. Mater.*, 2018, **84**, 625–630.
- 91 X.-L. Fu, Z.-J. Peng, D. Li, L. Zhang, J.-H. Xiao, J.-Y. Li, *et al.*, Self-assembly of tetrapod-shaped CdS nanostructures into 3D networks by a transverse growth process, *Nanotechnology*, 2011, **22**, 175601.

- 92 Y. Liu, Y. Ma, W. Liu, Y. Shang, A. Zhu, P. Tan, *et al.*, Facet and morphology dependent photocatalytic hydrogen evolution with CdS nanoflowers using a novel mixed solvothermal strategy, *J. Colloid Interface Sci.*, 2018, **513**, 222–230.
- 93 W.-T. Yao, S.-H. Yu, S.-J. Liu, J.-P. Chen, X.-M. Liu and F.-Q. Li, Architectural Control Syntheses of CdS and CdSe Nanoflowers, Branched Nanowires, and Nanotrees *via* a Solvothermal Approach in a Mixed Solution and Their Photocatalytic Property, *J. Phys. Chem. B*, 2006, **110**, 11704–11710.
- 94 S. M. H. Al-Jawad, N. J. Imran and K. H. Aboud, Synthesis and characterization of Mn:CdS nanoflower thin films prepared by hydrothermal method for photocatalytic activity, *J. Sol-Gel Sci. Technol.*, 2021, **100**, 423–439.
- 95 R. S. Ganesh, S. K. Sharma, E. Durgadevi, M. Navaneethan, S. Ponnusamy, C. Muthamizhchelvan, *et al.*, Growth, microstructure, structural and optical properties of PVP-capped CdS nanoflowers for efficient photocatalytic activity of Rhodamine B, *Mater. Res. Bull.*, 2017, **94**, 190–198.
- 96 H. S. H. Mohamed, M. Rabia, M. Shaban and S. Taha, Controlled synthesis of CdS nanoflowers thin films for H<sub>2</sub> electro-generation, *Mater. Sci. Semicond. Process.*, 2020, **120**, 105307.
- 97 G. Murali, D. Amaranatha Reddy, G. Giribabu and R. P. Vijayalakshmi, Growth and characterization of rose-flower-like CdS microstructures, *Ceram. Int.*, 2014, **40**, 11813–11817.
- 98 K. Zhong, K. Song and K. Clays, Hollow spheres: crucial building blocks for novel nanostructures and nanophotonics, *J. Nanophotonics*, 2018, **7**, 693–713.
- 99 X. Lai, J. E. Halpert and D. Wang, Recent advances in micro-/nano-structured hollow spheres for energy applications: From simple to complex systems, *Energy Environ. Sci.*, 2012, **5**, 5604–5618.
- 100 H. Gröger, C. Kind, P. Leidinger, M. Roming and C. Feldmann, Nanoscale Hollow Spheres: Microemulsion-Based Synthesis, Structural Characterization and Container-Type Functionality, *Materials*, 2010, **3**, 4355–4386.
- 101 C. Wang, Y. Ao, P. Wang, J. Hou, J. Qian and S. Zhang, Controlled synthesis in large-scale of CdS mesospheres and photocatalytic activity, *Mater. Lett.*, 2010, **64**, 439–441.
- 102 M. Kaur and C. M. Nagaraja, Template-free syntheses of CdS microspheres composed of ultrasmall nanocrystals and their photocatalytic study, *RSC Adv.*, 2014, **4**, 18257–18263.
- 103 M. Kaur and C. M. Nagaraja, Template-Free Synthesis of Zn<sub>1-x</sub>Cd<sub>x</sub>S Nanocrystals with Tunable Band Structure for Efficient Water Splitting and Reduction of Nitroaromatics in Water, *ACS Sustainable Chem. Eng.*, 2017, **5**, 4293–4303.
- 104 J. D. Patel, F. Mighri, A. Ajji and T. K. Chaudhuri, Fatty acid-assisted synthesis of CdS microspheres: physicochemical properties and photocatalytic activity, *Mater. Lett.*, 2013, **110**, 94–97.
- 105 C. Wei, W. Zang, J. Yin, Q. Lu, Q. Chen and R. Liu, Biomolecule-Assisted Construction of Cadmium Sulfide Hollow Spheres with Structure-Dependent Photocatalytic Activity, *ChemPhysChem*, 2013, **14**, 591–596.
- 106 S. Han, L. Hu, N. Gao, A. A. Al-Ghamdi and X. Fang, Efficient Self-Assembly Synthesis of Uniform CdS Spherical Nanoparticles-Au Nanoparticles Hybrids with Enhanced Photoactivity, *Adv. Funct. Mater.*, 2014, **24**, 3725–3733.
- 107 P. A. L. Lopes, M. Brandão Santos, A. J. S. Mascarenhas and L. A. Silva, Synthesis of CdS nano-spheres by a simple and fast sonochemical method at room temperature, *Mater. Lett.*, 2014, **136**, 111–113.
- 108 R. S. Ganesh, S. K. Sharma, E. Durgadevi, M. Navaneethan, H. S. Binitha, S. Ponnusamy, *et al.*, Surfactant free synthesis of CdS nanospheres, microstructural analysis, chemical bonding, optical properties and photocatalytic activities, *Superlattices Microstruct.*, 2017, **104**, 247–257.
- 109 Z. Wang, X. Yang, H. Jia and Y. Wang, Preparation of self-assembled hollow microsphere CdS *via* solvothermal method and its optical properties, *J. Mater. Sci.: Mater. Electron.*, 2016, **27**, 9725–9733.
- 110 X. Li, J. Yu and M. Jaroniec, Hierarchical photocatalysts, *Chem. Soc. Rev.*, 2016, **45**, 2603–2636.
- 111 Z. Xu, W. Deng and X. Wang, 3D Hierarchical Carbon-Rich Micro-/Nanomaterials for Energy Storage and Catalysis, *Electrochem. Energy Rev.*, 2021, **4**, 269–335.
- 112 S. Xiong, B. Xi and Y. Qian, CdS Hierarchical Nanostructures with Tunable Morphologies: Preparation and Photocatalytic Properties, *J. Phys. Chem. C*, 2010, **114**, 14029–14035.
- 113 V. U. Pandit, S. S. Arbuj, R. R. Hawaldar, P. V. Kshirsagar, A. J. Deshmukh, J. D. Ambekar, *et al.*, Hierarchical CdS nanostructure by Lawesson's reagent and its enhanced photocatalytic hydrogen production, *RSC Adv.*, 2015, **5**, 13715–13721.
- 114 Z. Yu, X. Wu, J. Wang, W. Jia, G. Zhu and F. Qu, Facile template-free synthesis and visible-light driven photocatalytic performances of dendritic CdS hierarchical structures, *Dalton Trans.*, 2013, **42**, 4633–4638.
- 115 S. N. Jamble, K. P. Ghoderao and R. B. Kale, Studies on growth mechanism and physical properties of hydrothermally synthesized CdS with novel hierarchical superstructures and their photocatalytic activity, *J. Phys. Chem. Solids*, 2018, **114**, 109–120.
- 116 X. Yang, Z. Wang, X. Lv, Y. Wang and H. Jia, Enhanced photocatalytic activity of Zn-doped dendritic-like CdS structures synthesized by hydrothermal synthesis, *J. Photochem. Photobiol., A*, 2016, **329**, 175–181.
- 117 K. Dai, J. Lv, J. Zhang, Q. Li, L. Geng and C. Liang, Controlled synthesis of novel 3D CdS hierarchical microtremella for photocatalytic H<sub>2</sub> production, *Mater. Lett.*, 2019, **235**, 11–14.
- 118 Q. Shen, J. Xue, J. Liu, H. Jia, X. Liu and B. Xu, Shape-controlled synthesis of three-dimensional branched CdS nanostructure arrays: structural characteristics and

- formation mechanism, *CrystEngComm*, 2013, **15**, 1007–1014.
- 119 W. Qiu, M. Xu, X. Yang, F. Chen, Y. Nan and H. Chen, Novel hierarchical CdS crystals by an amino acid mediated hydrothermal process, *J. Alloys Compd.*, 2011, **509**, 8413–8420.
- 120 L. Yan, A. Uddin and H. Wang, ZnO Tetrapods: Synthesis and Applications in Solar Cells, *Nanomater. Nanotechnol.*, 2015, **5**, 19.
- 121 M. Chen, Y. Xie, J. Lu, Y. Xiong, S. Zhang, Y. Qian, *et al.*, Synthesis of rod-, twinrod-, and tetrapod-shaped CdS nanocrystals using a highly oriented solvothermal recrystallization technique, *J. Mater. Chem.*, 2002, **12**, 748–753.
- 122 Y. K. Mishra and R. Adelung, ZnO tetrapod materials for functional applications, *Mater. Today*, 2018, **21**, 631–651.
- 123 K. Balasubramanian, A. Kumar Pandey, R. Abolhassani, H.-G. Rubahn, S. Rahman and Y. Kumar Mishra, Tetrapods based engineering of organic phase change material for thermal energy storage, *Chem. Eng. J.*, 2023, **462**, 141984.
- 124 Y. K. Mishra, G. Modi, V. Cretu, V. Postica, O. Lupan, T. Reimer, *et al.*, Direct Growth of Freestanding ZnO Tetrapod Networks for Multifunctional Applications in Photocatalysis, UV Photodetection, and Gas Sensing, *ACS Appl. Mater. Interfaces*, 2015, **7**, 14303–14316.
- 125 J. Rodrigues, M. Hoppe, N. Ben Sedrine, N. Wolff, V. Duppel, L. Kienle, *et al.*, ZnAl<sub>2</sub>O<sub>4</sub> decorated Al-doped ZnO tetrapolar 3D networks: microstructure, Raman and detailed temperature dependent photoluminescence analysis, *Nanoscale Adv.*, 2020, **2**, 2114–2126.
- 126 A. Vaneski, J. Schneider, A. S. Sussha and A. L. Rogach, Aqueous synthesis of CdS and CdSe/CdS tetrapods for photocatalytic hydrogen generation, *APL Mater.*, 2014, **2**, 012104.
- 127 J. E. Govan, E. Jan, A. Querejeta, N. A. Kotov and Y. K. Gun'ko, Chiral luminescent CdS nano-tetrapods, *Chem. Commun.*, 2010, **46**, 6072–6074.
- 128 H. Chu, X. Li, G. Chen, W. Zhou, Y. Zhang, Z. Jin, *et al.*, Shape-Controlled Synthesis of CdS Nanocrystals in Mixed Solvents, *Cryst. Growth Des.*, 2005, **5**, 1801–1806.
- 129 F. Xue, W. Fu, M. Liu, X. Wang, B. Wang and L. Guo, Insight into Cd<sub>0.9</sub>Zn<sub>0.1</sub>S solid-solution nanotetrapods: Growth mechanism and their application for photocatalytic hydrogen production, *Int. J. Hydrogen Energy*, 2016, **41**, 20455–20464.
- 130 X. Wang, Z. Feng, D. Fan, F. Fan and C. Li, Shape-Controlled Synthesis of CdS Nanostructures via a Solvothermal Method, *Cryst. Growth Des.*, 2010, **10**, 5312–5318.
- 131 J. Yu, Y. Yu and B. Cheng, Enhanced visible-light photocatalytic H<sub>2</sub>-production performance of multi-armed CdS nanorods, *RSC Adv.*, 2012, **2**, 11829–11835.
- 132 A. Vaneski, J. Schneider, A. S. Sussha and A. L. Rogach, Aqueous synthesis of CdS and CdSe/CdS tetrapods for photocatalytic hydrogen generation, *APL Mater.*, 2014, **2**, 012104.
- 133 X. Wang, M. Liu, Z. Zhou and L. Guo, Toward Facet Engineering of CdS Nanocrystals and Their Shape-Dependent Photocatalytic Activities, *J. Phys. Chem. C*, 2015, **119**, 20555–20560.
- 134 L. Zhang, Z. Cheng, D. Wang and J. Li, Preparation of popcorn-shaped CdS nanoparticles by hydrothermal method and their potent photocatalytic degradation efficiency, *Mater. Lett.*, 2015, **158**, 439–441.
- 135 X. Kong, F. Yu, H. Zhang, F. Lv, Y. Wang, L. Yin, *et al.*, Synthesis and study of morphology regulation, formation mechanism and photocatalytic performance of CdS, *Appl. Surf. Sci.*, 2022, **576**, 151817.
- 136 C. Feng, Z. Chen, J. Jing, M. Sun, J. Tian, J. Han, *et al.*, Synthesis of a novel three-dimensional sponge-like microporous CdS film with high photoelectrochemical performance and stability, *J. Electroanal. Chem.*, 2020, **874**, 114524.
- 137 M. Salavati-Niasari and A. Sobhani, Single-Source Molecular Precursor for Synthesis of CdS Nanoparticles and Nanoflowers, *High Temp. Mater. Processes*, 2012, **31**, 157–162.
- 138 Y. Du, B. Chen, Z. Yin, Z. Liu and H. Zhang, Phosphine-Free, Low-Temperature Synthesis of Tetrapod-Shaped CdS and Its Hybrid with Au Nanoparticles, *Small*, 2014, **10**, 4727–4734.
- 139 T. Senasu and S. Nanan, Photocatalytic performance of CdS nanomaterials for photodegradation of organic azo dyes under artificial visible light and natural solar light irradiation, *J. Mater. Sci.: Mater. Electron.*, 2017, **28**, 17421–17441.
- 140 H. K. Aboud, M. H. S. AL-Jawad and N. Jamal Imran, Preparation and Characterization of Hierarchical CdS Nanoflowers for Efficient Photocatalytic Degradation, *J. Nanostruct.*, 2022, **12**, 316–329.
- 141 S. Sharma, S. Singh and N. Khare, Synthesis of polyaniline/CdS (nanoflowers and nanorods) nanocomposites: a comparative study towards enhanced photocatalytic activity for degradation of organic dye, *Colloid Polym. Sci.*, 2016, **294**, 917–926.
- 142 X. Cui, Y. Wang, G. Jiang, Z. Zhao, C. Xu, A. Duan, *et al.*, The encapsulation of CdS in carbon nanotubes for stable and efficient photocatalysis, *J. Mater. Chem. A*, 2014, **2**, 20939–20946.
- 143 N. Zhang, Y. Zhang, X. Pan, X. Fu, S. Liu and Y.-J. Xu, Assembly of CdS Nanoparticles on the Two-Dimensional Graphene Scaffold as Visible-Light-Driven Photocatalyst for Selective Organic Transformation under Ambient Conditions, *J. Phys. Chem. C*, 2011, **115**, 23501–23511.
- 144 J. Prakash, S. B. N. Krishna, P. Kumar, V. Kumar, K. S. Ghosh, H. C. Swart, *et al.*, Recent Advances on Metal Oxide Based Nano-Photocatalysts as Potential Antibacterial and Antiviral Agents, *Catalysts*, 2022, **12**, 1047.
- 145 K. S. Bhavsar, P. K. Labhane, R. B. Dhake and G. H. Sonawane, Solvothermal synthesis of activated carbon loaded CdS nanoflowers: Boosted

- photodegradation of dye by adsorption and photocatalysis synergy, *Chem. Phys. Lett.*, 2020, **744**, 137202.
- 146 S. Sharma, D. Kumar and N. Khare, Hierarchical PANI/CdS nanoarchitecture system for visible light induced photocatalytic dye degradation and photoelectrochemical water splitting, *Polymer*, 2021, **231**, 124117.
- 147 X.-N. Wei, C.-L. Ou, S.-S. Fang, X.-C. Zheng, G.-P. Zheng and X.-X. Guan, One-pot self-assembly of 3D CdS-graphene aerogels with superior adsorption capacity and photocatalytic activity for water purification, *Powder Technol.*, 2019, **345**, 213–222.
- 148 H. Liu, T. Lv, X. Wu, C. Zhu and Z. Zhu, Preparation and enhanced photocatalytic activity of CdS@RGO core-shell structural microspheres, *Appl. Surf. Sci.*, 2014, **305**, 242–246.
- 149 J. Huang, L. Li, J. Chen, F. Ma and Y. Yu, Broad spectrum response flower spherical-like composites CQDs@CdIn<sub>2</sub>S<sub>4</sub>/CdS modified by CQDs with up-conversion property for photocatalytic degradation and water splitting, *Int. J. Hydrogen Energy*, 2020, **45**, 1822–1836.
- 150 J. Pan, J. Liu, S. Zuo, U. A. Khan, Y. Yu and B. Li, Structure of Z-scheme CdS/CQDs/BiOCl heterojunction with enhanced photocatalytic activity for environmental pollutant elimination, *Appl. Surf. Sci.*, 2018, **444**, 177–186.
- 151 M. Alomar, Y. Liu, W. Chen and H. Fida, Controlling the growth of ultrathin MoS<sub>2</sub> nanosheets/CdS nanoparticles by two-step solvothermal synthesis for enhancing photocatalytic activities under visible light, *Appl. Surf. Sci.*, 2019, **480**, 1078–1088.
- 152 C. Liu, J. Chen, H. Che, K. Huang, P. A. Charpentier, W. Z. Xu, *et al.*, Construction and enhanced photocatalytic activities of a hydrogenated TiO<sub>2</sub> nanobelt coated with CDs/MoS<sub>2</sub> nanosheets, *RSC Adv.*, 2017, **7**, 8429–8442.
- 153 D. Vikraman, S. S. Patil, S. Hussain, M. Hussain, K. Karuppasamy, P. Santhoshkumar, *et al.*, Decoration of X<sub>2</sub>C nanoparticles on CdS nanostructures for highly efficient photocatalytic wastewater treatment under visible light, *Appl. Surf. Sci.*, 2022, **583**, 152533.
- 154 N. Li, Q. Zhang, L. Han, J. Huang, X. Luo and X. Li, Recent advances in polydopamine and its derivatives assisted electrocatalysis and photocatalysis, *Int. J. Hydrogen Energy*, 2023, **48**, 7004–7018.
- 155 D. Yang, W. Wang, X. Zhao, Z. Zhou, H. Ren, Y. Chen, *et al.*, Synthesis of high-efficient g-C<sub>3</sub>N<sub>4</sub>/polydopamine/CdS nanophotocatalyst based on bioinspired adhesion and chelation, *Mater. Res. Bull.*, 2020, **131**, 110970.
- 156 M. Wang, Z. Cui, M. Yang, L. Lin, X. Chen, M. Wang, *et al.*, Core/shell structured CdS/polydopamine/TiO<sub>2</sub> ternary hybrids as highly active visible-light photocatalysis, *J. Colloid Interface Sci.*, 2019, **544**, 1–7.
- 157 H. Zhao, S. Cui, L. Yang, G. Li, N. Li and X. Li, Synthesis of hierarchically meso-macroporous TiO<sub>2</sub>/CdS heterojunction photocatalysts with excellent visible-light photocatalytic activity, *J. Colloid Interface Sci.*, 2018, **512**, 47–54.
- 158 S.-Y. Li, Z.-L. Liu, G.-X. Xiang, B.-H. Ma, X.-D. Meng and Y.-L. He, Influence of calcination temperature on the photocatalytic performance of the hierarchical TiO<sub>2</sub> pinecone-like structure decorated with CdS nanoparticles, *Ceram. Int.*, 2019, **45**, 767–776.
- 159 F. Tian, D. Hou, F. Hu, K. Xie, X. Qiao and D. Li, Porous TiO<sub>2</sub> nanofibers decorated CdS nanoparticles by SILAR method for enhanced visible-light-driven photocatalytic activity, *Appl. Surf. Sci.*, 2017, **391**, 295–302.
- 160 N. Zhang, Y. Zhang, X. Pan, M.-Q. Yang and Y.-J. Xu, Constructing Ternary CdS-Graphene-TiO<sub>2</sub> Hybrids on the Flatland of Graphene Oxide with Enhanced Visible-Light Photoactivity for Selective Transformation, *J. Phys. Chem. C*, 2012, **116**, 18023–18031.
- 161 B. Li and Y. Wang, Synthesis, microstructure, and photocatalysis of ZnO/CdS nano-heterostructure, *J. Phys. Chem. Solids*, 2011, **72**, 1165–1169.
- 162 F. Xu, Y. Yuan, H. Han, D. Wu, Z. Gao and K. Jiang, Synthesis of ZnO/CdS hierarchical heterostructure with enhanced photocatalytic efficiency under nature sunlight, *CrystEngComm*, 2012, **14**, 3615–3622.
- 163 T. K. Jana, A. Pal and K. Chatterjee, Self assembled flower like CdS-ZnO nanocomposite and its photo catalytic activity, *J. Alloys Compd.*, 2014, **583**, 510–515.
- 164 M. Alomar, Y. Liu and W. Chen, Surface Decorated Zn<sub>0.15</sub>Cd<sub>0.85</sub>S Nanoflowers with P25 for Enhanced Visible Light Driven Photocatalytic Degradation of Rh-B and Stability, *Appl. Sci.*, 2018, **8**, 327.
- 165 W. Cui, W. An, L. Liu, J. Hu and Y. Liang, Synthesis of CdS/BiOBr composite and its enhanced photocatalytic degradation for Rhodamine B, *Appl. Surf. Sci.*, 2014, **319**, 298–305.
- 166 R. Rajendran, K. Varadharajan, V. Jayaraman, B. Singaram and J. Jeyaram, Photocatalytic degradation of metronidazole and methylene blue by PVA-assisted Bi<sub>2</sub>WO<sub>6</sub>-CdS nanocomposite film under visible light irradiation, *Appl. Nanosci.*, 2018, **8**, 61–78.
- 167 K. Kadeer, Y. Tursun, T. Dilinuer, K. Okitsu and A. Abulizi, Sonochemical preparation and photocatalytic properties of CdS QDs/Bi<sub>2</sub>WO<sub>6</sub> 3D heterojunction, *Ceram. Int.*, 2018, **44**, 13797–13805.
- 168 L. Mao, X.-Y. Cai and M.-S. Zhu, Hierarchically 1D CdS decorated on 2D perovskite-type La<sub>2</sub>Ti<sub>2</sub>O<sub>7</sub> nanosheet hybrids with enhanced photocatalytic performance, *Rare Met.*, 2021, **40**, 1067–1076.
- 169 T. Cheng, H. Gao, G. Liu, Z. Pu, S. Wang, Z. Yi, *et al.*, Preparation of core-shell heterojunction photocatalysts by coating CdS nanoparticles onto Bi<sub>4</sub>Ti<sub>3</sub>O<sub>12</sub> hierarchical microspheres and their photocatalytic removal of organic pollutants and Cr(VI) ions, *Colloids Surf., A*, 2022, **633**, 127918.
- 170 B. Weng, K.-Q. Lu, Z. Tang, H. M. Chen and Y.-J. Xu, Stabilizing ultrasmall Au clusters for enhanced photoredox catalysis, *Nat. Commun.*, 2018, **9**, 1543.
- 171 L. Liu, X. Zhang, L. Yang, L. Ren, D. Wang and J. Ye, Metal nanoparticles induced photocatalysis, *Natl. Sci. Rev.*, 2017, **4**, 761–780.
- 172 P. Kumar, M. Chandra Mathpal, J. Prakash, B. C. Viljoen, W. D. Roos and H. C. Swart, Band gap tailoring of

- cauliflower-shaped CuO nanostructures by Zn doping for antibacterial applications, *J. Alloys Compd.*, 2020, **832**, 154968.
- 173 P. Kumar, M. Chandra Mathpal, G. Jagannath, J. Prakash, J.-R. Maze, W. D. Roos, *et al.*, Optical limiting applications of resonating plasmonic Au nanoparticles in a dielectric glass medium, *Nanotechnology*, 2021, **32**, 345709.
- 174 J. Prakash, J. Cho and Y. K. Mishra, Photocatalytic TiO<sub>2</sub> nanomaterials as potential antimicrobial and antiviral agents: Scope against blocking the SARS-COV-2 spread, *Micro Nano Eng.*, 2022, **14**, 100100.
- 175 R. V. Samriti, R. K. Gupta and J. Prakash, Engineering metal oxide semiconductor nanostructures for enhanced charge transfer: fundamentals and emerging SERS applications, *J. Mater. Chem. C*, 2022, **10**, 73–95.
- 176 Q. Kong, R. Wu, X. Feng, C. Ye, G. Hu, J. Hu, *et al.*, Synthesis; characterization; and growth mechanism of Au/CdS heterostructured nanoflowers constructed with nanorods, *J. Alloys Compd.*, 2011, **509**, 3048–3051.
- 177 J. Xiong, X. Du, G. Cheng, H. Yang, J. Chen, S. Dou, *et al.*, One dimensional hierarchical nanostructures composed of CdS nanosheets/nanoparticles and Ag nanowires with promoted photocatalytic performance, *Inorg. Chem. Front.*, 2018, **5**, 903–915.
- 178 J. Li, Z. Xia, D. Ma, G. Liu, N. Song, D. Xiang, *et al.*, Improving photocatalytic activity by construction of immobilized Z-scheme CdS/Au/TiO<sub>2</sub> nanobelt photocatalyst for eliminating norfloxacin from water, *J. Colloid Interface Sci.*, 2021, **586**, 243–256.
- 179 Q. Chen, M. Zhang, J. Li, G. Zhang, Y. Xin and C. Chai, Construction of immobilized 0D/1D heterostructure photocatalyst Au/CuS/CdS/TiO<sub>2</sub> NBs with enhanced photocatalytic activity towards moxifloxacin degradation, *Chem. Eng. J.*, 2020, **389**, 124476.
- 180 M. Zhang, H.-f Yin, J.-c Yao, M. Arif, B. Qiu, P.-f Li, *et al.*, All-solid-state Z-scheme BiOX(Cl, Br)-Au-CdS heterostructure: Photocatalytic activity and degradation pathway, *Colloids Surf., A*, 2020, **602**, 124778.
- 181 X. Deng, C. Wang, H. Yang, M. Shao, S. Zhang, X. Wang, *et al.*, One-pot hydrothermal synthesis of CdS decorated CuS microflower-like structures for enhanced photocatalytic properties, *Sci. Rep.*, 2017, **7**, 3877.
- 182 M. Wan, S. Cui, W. Wei, S. Cui, K. Chen, W. Chen, *et al.*, Bi-component synergic effect in lily-like CdS/Cu<sub>7</sub>S<sub>4</sub> QDs for dye degradation, *RSC Adv.*, 2019, **9**, 2441–2450.
- 183 L. Shi, Z. Ma, W. Qu, W. Zhou, Z. Deng and H. Zhang, Hierarchical Z-scheme Bi<sub>2</sub>S<sub>3</sub>/CdS heterojunction: Controllable morphology and excellent photocatalytic antibacterial, *Appl. Surf. Sci.*, 2021, **568**, 150923.
- 184 S. Huang, Z. Wei, L. Ma, C. Li, Q. Lu and J. Ma, Hydrothermal synthesis, photo-electrochemical and photocatalytic activity of SnS<sub>2</sub>/CdS nanocomposites, *J. Mater. Sci.: Mater. Electron.*, 2021, **32**, 676–686.
- 185 Z. Pu, T. Liu, G. Zhang, Z. Chen, D.-S. Li, N. Chen, W. Chen, Z. Chen and S. Sun, General Synthesis of Transition-Metal-Based Carbon-Group Intermetallic Catalysts for Efficient Electrocatalytic Hydrogen Evolution in Wide pH Range, *Adv. Energy Mater.*, 2022, **12**, 2200293.
- 186 F. Hu, D. Yu, M. Ye, H. Wang, Y. Hao, L. Wang, L. Li, X. Han and S. Peng, Lattice-Matching Formed Mesoporous Transition Metal Oxide Heterostructures Advance Water Splitting by Active Fe–O–Cu Bridges, *Adv. Energy Mater.*, 2022, **12**, 2200067.
- 187 Z. Pu, I. S. Amiinu, Z. Kou, W. Li and S. Mu, RuP<sub>2</sub>-Based Catalysts with Platinum-like Activity and Higher Durability for the Hydrogen Evolution Reaction at All pH Values, *Angew. Chem., Int. Ed.*, 2017, **56**, 11559–11564.
- 188 J. A. Nasir, R. Zu, S. N. A. Shah, A. Khan, I. S. Butler and C. R. A. Catlow, Recent developments and perspectives in CdS-based photocatalysts for water splitting, *J. Mater. Chem. A*, 2020, **8**, 20752–20780.
- 189 A. Fujishima and K. Honda, Electrochemical Photolysis of Water at a Semiconductor Electrode, *Nature*, 1972, **238**, 37–38.
- 190 X. Li, J. Yu, S. Wageh, A. A. Al-Ghamdi and J. Xie, Graphene in Photocatalysis: A Review, *Small*, 2016, **12**, 6640–6696.
- 191 H. Zhang, L. V. Besteiro, J. Liu, C. Wang, G. S. Selopal, Z. Chen, *et al.*, Efficient and stable photoelectrochemical hydrogen generation using optimized colloidal heterostructured quantum dots, *Nano Energy*, 2021, **79**, 105416.
- 192 X. Chen, S. Shen, L. Guo and S. S. Mao, Semiconductor-based Photocatalytic Hydrogen Generation, *Chem. Rev.*, 2010, **110**, 6503–6570.
- 193 S. Cao, L. Piao and X. Chen, Emerging Photocatalysts for Hydrogen Evolution, *Trends Chem.*, 2020, **2**, 57–70.
- 194 K. Maeda and K. Domen, New Non-Oxide Photocatalysts Designed for Overall Water Splitting under Visible Light, *J. Phys. Chem. C*, 2007, **111**, 7851–7861.
- 195 N. Bao, L. Shen, T. Takata and K. Domen, Self-Templated Synthesis of Nanoporous CdS Nanostructures for Highly Efficient Photocatalytic Hydrogen Production under Visible Light, *Chem. Mater.*, 2008, **20**, 110–117.
- 196 Y. Ma, Y. Liu, Y. Bian, A. Zhu, Y. Yang and J. Pan, Controlling shape anisotropy of hexagonal CdS for highly stable and efficient photocatalytic H<sub>2</sub> evolution and photoelectrochemical water splitting, *J. Colloid Interface Sci.*, 2018, **518**, 140–148.
- 197 F. Vaquero, R. M. Navarro and J. L. G. Fierro, Influence of the solvent on the structure, morphology and performance for H<sub>2</sub> evolution of CdS photocatalysts prepared by solvothermal method, *Appl. Catal., B*, 2017, **203**, 753–767.
- 198 L. Song, T. Li, S. Zhang and S. Zhang, Synthesis of rhodium phosphide cocatalyst and remarkably enhanced photocatalytic hydrogen evolution over CdS under visible light radiation, *Chem. Eng. J.*, 2017, **314**, 498–507.
- 199 Y. Wang, G. Meng, L. Zhang, C. Liang and J. Zhang, Catalytic Growth of Large-Scale Single-Crystal CdS Nanowires by Physical Evaporation and Their Photoluminescence, *Chem. Mater.*, 2002, **14**, 1773–1777.
- 200 R. M. Navarro, F. del Valle and J. L. G. Fierro, Photocatalytic hydrogen evolution from CdS–ZnO–CdO systems under



- visible light irradiation: Effect of thermal treatment and presence of Pt and Ru cocatalysts, *Int. J. Hydrogen Energy*, 2008, **33**, 4265–4273.
- 201 J. Fang, J. Gu, Q. Liu, W. Zhang, H. Su and D. Zhang, Three-Dimensional CdS/Au Butterfly Wing Scales with Hierarchical Rib Structures for Plasmon-Enhanced Photocatalytic Hydrogen Production, *ACS Appl. Mater. Interfaces*, 2018, **10**, 19649–19655.
- 202 E. Soto, F. Vaquero, N. Mota, R. M. Navarro and J. L. G. Fierro, CdS Photocatalysts Modified with Ag: Effect of the Solvothermal Temperature on the Structure and Photoactivity for Hydrogen Production, *Catalyst*, 2019, **9**, 110.
- 203 P. Wang, Y. Sheng, F. Wang and H. Yu, Synergistic effect of electron-transfer mediator and interfacial catalytic active-site for the enhanced H<sub>2</sub>-evolution performance: A case study of CdS-Au photocatalyst, *Appl. Catal., B*, 2018, **220**, 561–569.
- 204 F. F. Schweinberger, M. J. Berr, M. Döblinger, C. Wolff, K. E. Sanwald, A. S. Crampton, *et al.*, Cluster Size Effects in the Photocatalytic Hydrogen Evolution Reaction, *J. Am. Chem. Soc.*, 2013, **135**, 13262–13265.
- 205 L. Luo, Y. Wang, S. Huo, P. Lv, J. Fang, Y. Yang, *et al.*, Cu-MOF assisted synthesis of CuS/CdS(H)/CdS(C): Enhanced photocatalytic hydrogen production under visible light, *Int. J. Hydrogen Energy*, 2019, **44**, 30965–30973.
- 206 A. Meng, B. Zhu, B. Zhong, L. Zhang and B. Cheng, Direct Z-scheme TiO<sub>2</sub>/CdS hierarchical photocatalyst for enhanced photocatalytic H<sub>2</sub>-production activity, *Appl. Surf. Sci.*, 2017, **422**, 518–527.
- 207 S. Wang, B. Zhu, M. Liu, L. Zhang, J. Yu and M. Zhou, Direct Z-scheme ZnO/CdS hierarchical photocatalyst for enhanced photocatalytic H<sub>2</sub>-production activity, *Appl. Catal., B*, 2019, **243**, 19–26.
- 208 S. David, M. A. Mahadik, H. S. Chung, J. H. Ryu and J. S. Jang, Facile Hydrothermally Synthesized a Novel CdS Nanoflower/Rutile-TiO<sub>2</sub> Nanorod Heterojunction Photoanode Used for Photoelectrocatalytic Hydrogen Generation, *ACS Sustainable Chem. Eng.*, 2017, **5**, 7537–7548.
- 209 Z. Li, T. Ma, X. Zhang and Z. Wang, In<sub>2</sub>Se<sub>3</sub>/CdS nanocomposites as high efficiency photocatalysts for hydrogen production under visible light irradiation, *Int. J. Hydrogen Energy*, 2021, **46**, 15539–15549.
- 210 Y. Zhong, S. Yang, S. Zhang, X. Cai, Q. Gao, X. Yu, *et al.*, CdS branched TiO<sub>2</sub>: Rods-on-rods nanoarrays for efficient photoelectrochemical (PEC) and self-bias photocatalytic (PC) hydrogen production, *J. Power Sources*, 2019, **430**, 32–42.
- 211 Y. Zhang, Z. Peng, S. Guan and X. Fu, Novel β-NiS film modified CdS nanoflowers heterostructure nanocomposite: Extraordinarily highly efficient photocatalysts for hydrogen evolution, *Appl. Catal., B*, 2018, **224**, 1000–1008.
- 212 T. Zhang, F. Meng, Y. Cheng, N. Dewangan, G. W. Ho and S. Kawi, Z-scheme transition metal bridge of Co<sub>9</sub>S<sub>8</sub>/Cd/CdS tubular heterostructure for enhanced photocatalytic hydrogen evolution, *Appl. Catal., B*, 2021, **286**, 119853.
- 213 S. Liang, B. Han, X. Liu, W. Chen, M. Peng, G. Guan, *et al.*, 3D spatially branched hierarchical Z-scheme CdS-Au nanoclusters-ZnO hybrids with boosted photocatalytic hydrogen evolution, *J. Alloys Compd.*, 2018, **754**, 105–113.
- 214 J. Lv, J. Liu, J. Zhang, K. Dai, C. Liang, Z. Wang, *et al.*, Construction of organic–inorganic cadmium sulfide/diethylenetriamine hybrids for efficient photocatalytic hydrogen production, *J. Colloid Interface Sci.*, 2018, **512**, 77–85.
- 215 C. Wang, L. Wang, J. Jin, J. Liu, Y. Li, M. Wu, *et al.*, Probing effective photocorrosion inhibition and highly improved photocatalytic hydrogen production on monodisperse PANI@CdS core-shell nanospheres, *Appl. Catal., B*, 2016, **188**, 351–359.
- 216 H. Yu, F. Chen, F. Chen and X. Wang, *In situ* self-transformation synthesis of g-C<sub>3</sub>N<sub>4</sub>-modified CdS heterostructure with enhanced photocatalytic activity, *Appl. Surf. Sci.*, 2015, **358**, 385–392.
- 217 Y. Kim, E. Coy, H. Kim, R. Mrówczyński, P. Torruella, D.-W. Jeong, *et al.*, Efficient photocatalytic production of hydrogen by exploiting the polydopamine-semiconductor interface, *Appl. Catal., B*, 2021, **280**, 119423.
- 218 W. Wang, M. Li, X. Huang, J. Fang, F. Peng and H. Huang, Structural evolution mechanisms of Polydopamine/CdS and photothermal effect boosted photocatalytic H<sub>2</sub> production activity, *Appl. Surf. Sci.*, 2022, **601**, 154114.
- 219 X. Liu, T. Zhang, Y. Li, J. Zhang, Y. Du, Y. Yang, *et al.*, CdS@Polydopamine@SnO<sub>2-x</sub> sandwich structure with electrostatic repulsion effect and oxygen deficiency: enhanced photocatalytic hydrogen evolution activity and inhibited photo-corrosion, *Chem. Eng. J.*, 2022, **434**, 134602.
- 220 Z. Chen, G. Zhang, J. Prakash, Y. Zheng and S. Sun, Rational Design of Novel Catalysts with Atomic Layer Deposition for the Reduction of Carbon Dioxide, *Adv. Energy Mater.*, 2019, **9**, 1900889.
- 221 M. Xu, C. Sun, X. Zhao, H. Jiang, H. Wang and P. Huo, Fabricated hierarchical CdS/Ni-MOF heterostructure for promoting photocatalytic reduction of CO<sub>2</sub>, *Appl. Surf. Sci.*, 2022, **576**, 151792.
- 222 Z. Chen, G. Zhang, H. Chen, J. Prakash, Y. Zheng and S. Sun, Multi-metallic catalysts for the electroreduction of carbon dioxide: Recent advances and perspectives, *Renewable Sustainable Energy Rev.*, 2022, **155**, 111922.
- 223 L. Long, G. Lv, Q. Han, X. Wu, Y. Qian, D. Wang, *et al.*, Achieving Direct Z-Scheme Charge Transfer through Constructing 2D/2D α-Fe<sub>2</sub>O<sub>3</sub>/CdS Heterostructure for Efficient Photocatalytic CO<sub>2</sub> Conversion, *J. Phys. Chem. C*, 2021, **125**, 23142–23152.
- 224 Z. Zhu, X. Li, Y. Qu, F. Zhou, Z. Wang, W. Wang, *et al.*, A hierarchical heterostructure of CdS QDs confined on 3D ZnIn<sub>2</sub>S<sub>4</sub> with boosted charge transfer for photocatalytic CO<sub>2</sub> reduction, *Nano Res.*, 2021, **14**, 81–90.
- 225 Z. Chen, G. Zhang, Y. Wen, N. Chen, W. Chen, T. Regier, J. Dynes, Y. Zheng, S. Sun, *et al.*, Atomically Dispersed Fe-

- Co Bimetallic Catalysts for the Promoted Electroreduction of Carbon Dioxide, *Nano-Micro Lett.*, 2021, **14**, 25.
- 226 Z. Chen, G. Zhang, L. Du, Y. Zheng, L. Sun and S. Sun, Nanostructured Cobalt-Based Electrocatalysts for CO<sub>2</sub> Reduction: Recent Progress, Challenges, and Perspectives, *Small*, 2020, **16**, 2004158.
- 227 P. Zhang, S. Wang, B. Y. Guan and X. W. Lou, Fabrication of CdS hierarchical multi-cavity hollow particles for efficient visible light CO<sub>2</sub> reduction, *Energy Environ. Sci.*, 2019, **12**, 164–168.
- 228 Y.-X. Feng, H.-J. Wang, J.-W. Wang, W. Zhang, M. Zhang and T.-B. Lu, Stand-Alone CdS Nanocrystals for Photocatalytic CO<sub>2</sub> Reduction with High Efficiency and Selectivity, *ACS Appl. Mater. Interfaces*, 2021, **13**, 26573–26580.
- 229 S. Wang and X. Wang, Photocatalytic CO<sub>2</sub> reduction by CdS promoted with a zeolitic imidazolate framework, *Appl. Catal., B*, 2015, **162**, 494–500.
- 230 A. Varmazyari, A. Taghizadehghalehjoughi, C. Sevim, O. Baris, G. Eser, S. Yildirim, *et al.*, Cadmium sulfide-induced toxicity in the cortex and cerebellum: *In vitro* and *in vivo* studies, *Toxicol. Rep.*, 2020, **7**, 637–648.
- 231 X. Xie, R. Wang, Y. Ma, J. Chen, Z. Shi, Q. Cui, *et al.*, Sulfate-Functionalized Core–Shell ZnO/CdS/Ag<sub>2</sub>S Nanorod Arrays with Dual-Charge-Transfer Channels for Enhanced Photoelectrochemical Performance, *ACS Appl. Energy Mater.*, 2022, **5**, 6228–6237.
- 232 P. Gowdhaman, V. N. Praveen, R. Sakthi Sudar Saravanan, P. Venkateswari and H. M. Pandya, Facile synthesis of undoped and Sn doped CdS nanoparticles for dye-sensitized solar cell applications, *Opt. Mater.*, 2021, **120**, 111465.
- 233 D. Li, C. Yang, S. Rajendran, J. Qin and X. Zhang, Nanoflower-like Ti<sub>3</sub>CN@TiO<sub>2</sub>/CdS heterojunction photocatalyst for efficient photocatalytic water splitting, *Int. J. Hydrogen Energy*, 2022, **47**, 19580–19589.
- 234 U. Abdullah, M. Ali and E. Pervaiz, An Inclusive Review on Recent Advancements of Cadmium Sulfide Nanostructures and its Hybrids for Photocatalytic and Electrocatalytic Applications, *Mol. Catal.*, 2021, **508**, 111575.
- 235 S. Sharma, V. Dutta, P. Raizada, A. Hosseini-Bandegharai, P. Singh and V.-H. Nguyen, Tailoring cadmium sulfide-based photocatalytic nanomaterials for water decontamination: a review, *Environ. Chem. Lett.*, 2021, **19**, 271–306.